

**Noble Metal Nanoparticles Supported in
Ordered Mesoporous Carbon Coatings as Efficient
Electrocatalysts for the Hydrogen Evolution Reaction**

vorgelegt von
Diplom-Chemiker
Denis Robert Bernsmeier
geb. in Düsseldorf

Von der Fakultät II - Mathematik und Naturwissenschaften
der Technischen Universität Berlin
zur Erlangung des akademischen Grades

Doktor der Naturwissenschaften
- Dr. rer. nat. -

genehmigte Dissertation

Promotionsausschuss:

Vorsitzender: Prof. Dr. Arne Thomas
Gutachter: Dr.-Ing. Ralph Krähnert
Gutachter: Prof. Dr. Peter Strasser
Gutachterin: Prof. Dr. Christina Roth

Tag der wissenschaftlichen Aussprache: 02.12.2016

Berlin 2017

Für meinen Vater

Abstract

Hydrogen has the highest gravimetric energy density of all chemical substances. Accordingly, hydrogen is a promising candidate as a fuel or for energy storage. One efficient way to produce hydrogen is the electrolytic splitting of water molecules.

Water electrolysis requires electrode coatings with high catalytic activity. Platinum efficiently catalyzes the hydrogen evolution reaction (HER) in acidic environments but is also a rare and expensive metal. The activity achieved per metal atom can be increased when small Pt-containing particles are dispersed onto electrically conductive, accessible and stable support materials. However, the addition of Nafion, a typical binder material can decrease catalytic activity via blocking of pores and active surface sites.

This thesis reports two new synthesis approaches for highly active Nafion-free catalyst films consisting of small nanoparticles supported in a conductive mesoporous carbon matrix. One approach relies on the co-deposition of suitable noble metal ions together with carbon precursors in the presence of polymer micelles, which act as pore templates. The other approach employs preformed colloidal nanoparticles as noble metal precursors. Carbonization in inert atmosphere produces porous ordered mesoporous carbon films with defined structural properties like film thickness, pore size, nanoparticle composition and metal loading.

The films were tested for catalytic activity: Pt-containing catalyst films exhibited the highest activity in the HER and clearly outperform Nafion-based Pt/C catalysts in particular at high current densities. Bimetallic RuPt catalyst films showed a four times higher activity per Pt compared to conventional Pt/C reference catalysts. Pd-containing mesoporous carbon films were also tested as catalysts in the selective gas-phase hydrogenation of butadiene. The obtained catalysts provided significantly higher space-time-yields than all reported Pd/C catalysts.

The optimal conditions for carbonization were identified as well as necessary properties of the employed metal for a successful synthesis. Synthetic aspects like the influence of high weight loadings of the metal and kinetic aspects like the rate-determining step during the HER were studied.

Generally, the syntheses represent generic approaches to ordered mesoporous carbon coatings containing metal nanoparticles. Further improvements in the composition can lead to even higher activity and lower costs for catalyst production. The catalysts developed in this work can help to make water electrolyzers more efficient and cheaper.

Zusammenfassung

Wasserstoff besitzt die höchste massenspezifische Energiedichte aller chemischen Substanzen und erfährt daher zunehmende Bedeutung als Treibstoff oder als Energiespeicher. Die saure Wasserelektrolyse ist eine effiziente Methode um Wasserstoff herzustellen.

Um Überpotentiale bei der Wasserelektrolyse zu reduzieren, werden katalytisch aktive Elektrodenbeschichtungen eingesetzt. Platin ist der aktivste Katalysator für die Wasserstoffevolutionsreaktion (englisch *hydrogen evolution reaction HER*), jedoch ist es selten und teuer. Um die Massenaktivität des eingesetzten Platins zu erhöhen, werden üblicherweise kleine Pt-Nanopartikel auf elektrisch leitfähigem Kohlenstoff gebracht. Dieses Material sollte sowohl eine hohe Zugänglichkeit der aktiven Zentren sowie eine hohe Stabilität aufweisen. Nafion, welches typischerweise als Binder eingesetzt wird, kann jedoch die katalytische Aktivität reduzieren, indem es Poren sowie aktive Zentren blockiert.

Diese Arbeit beschreibt zwei neue Syntheseansätze für hochaktive Nafion-freie mesoporöse Katalysatorschichten. Diese bestehen aus kleinen Edelmetallnanopartikeln, verteilt in leitfähigem Kohlenstoff. Im ersten Syntheseansatz wurden lösliche ionische Edelmetall-Präkursoren verwendet, die zusammen mit einem Kohlenstoff-Präkursor sowie Blockcopolymeren, welche als Porentemplate dienten, abgeschieden wurden. Der zweite Syntheseansatz nutzte vorgeformte kolloidale Nanopartikel als Edelmetall-Präkursoren.

Karbonisierung führte zu porösen Katalysatorfilmen mit kontrollierbaren Eigenschaften wie Filmdicke, Porengröße und Verteilung sowie Zusammensetzung der Nanopartikel.

Die Katalysatorschichten wurden auf ihre katalytische Aktivität hin untersucht: Pt-haltige Schichten zeigten eine deutlich höhere Aktivität in der HER als vergleichbare Nafion-haltige Pt/C Schichten insbesondere bei hohen Stromdichten. RuPt Katalysatoren zeigten eine vierfach höhere Aktivität pro eingesetztem Platin. Darüber hinaus wurden Pd-haltige Schichten in der Hydrierung von Butadien untersucht. Sie zeigten eine signifikant höhere Raum-Zeit-Ausbeute als alle bisher veröffentlichten Pd/C Katalysatoren.

Es gelang die optimalen Karbonisierungstemperaturen der Schichten sowie notwendige Eigenschaften der einsetzbaren Metalle zu identifizieren. Synthetische Aspekte, wie der Einfluss einer hohen Metallbeladung und kinetische Aspekte, wie der geschwindigkeitsbestimmende Schritt der HER wurden untersucht.

Die präsentierten Syntheseansätze sind generisch und es lassen sich Kohlenstofffilme mit verschiedenen Edelmetallen herstellen. Durch weitere Verbesserungen der Zusammensetzung könnten noch aktivere und kostengünstigere Katalysatoren entwickelt werden, die dabei helfen Wasserelektrolyseure effizienter und preiswerter zu machen.

Table of contents

Abstract.....	iii
Zusammenfassung.....	v
Acronyms.....	viii
1 Introduction: The electrolytic hydrogen evolution reaction	1
1.1 Mechanisms: Volmer, Tafel and Heyrovsky	1
1.2 Thermodynamics and overpotential	2
1.3 Kinetics	3
1.4 Volcano plot and state-of-the-art Pt/C catalysts.....	5
1.5 Ordered mesoporous carbon films	6
1.6 Introduction of catalytically active metals into OMC films	8
1.7 Challenges, aims and structure of this thesis	9
2 Experimental.....	11
2.1 OMC film synthesis	11
2.2 Me/OMC film synthesis	13
2.3 MeNP/OMC film synthesis	14
2.4 Electrocatalytic testing	16
2.5 Morphology of an OMC film.....	17
3 Pd-containing mesoporous carbon films.....	21
3.1 Introduction	23
3.2 Experimental section.....	25
3.3 Results and Discussion.....	29
3.4 Conclusion	37
3.5 Acknowledgement.....	37
3.6 Supporting Information.....	38
4 Pt-containing mesoporous carbon films.....	41
4.1 Introduction	43
4.2 Experimental.....	45
4.3 Results and Discussion.....	48
4.4 Conclusion	55
4.5 Acknowledgement.....	55
4.6 Supporting Information.....	56
5 Ru and Pt-containing mesoporous carbon films.....	59
5.1 Introduction	61
5.2 Experimental.....	63
5.3 Results and discussion	67
5.4 Conclusion	78
5.5 Acknowledgement.....	78
5.6 Supporting Information.....	79
6 Incorporation of preformed Pt colloids into mesoporous carbon films	81
6.1 Introduction	83
6.2 Experimental.....	85
6.3 Results and discussion	89
6.4 Conclusion	97
6.5 Acknowledgement.....	97
7 General discussion.....	99
7.1 Influence of the metal precursor on structure and activity.....	99
7.2 Influence of composition on structure and activity	106
7.3 Tafel evaluation of Pt-containing carbon catalyst films	116
7.4 Comparison to literature.....	118

8	Conclusions and outlook	121
	Bibliography.....	123
	List of publications, patents and conference talks	140

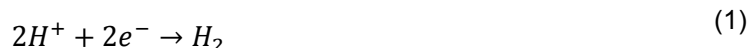
Acronyms

α	Charge transfer coefficient
acac	pentane-2,4-dionate: $(\text{CH}_3\text{COCHCOCH}_3)^-$, acetylacetonate
b	Tafel slope
β	angle of incidence of the X-ray on the film's surface plane
BESSY	Berliner Elektronenspeicherring für Synchrotronstrahlung
BET	Brunauer-Emmet-Teller
CV	cyclic voltammetry
ΔT	difference between carbonization and Tammann temperature: $T_{\text{carb}} - T_{\text{Tammann}}$
dec	decade (log scale)
DESY	Deutsches Elektronen-Synchrotron in Hamburg
DFT	density functional theory
E^0	standard potential
EDX	energy-dispersive X-ray fluorescence spectroscopy
EISA	evaporation induced self-assembly
F	Faraday's constant
FFT	fast Fourier transformation
ΔG	free enthalpy
ΔG_m	molar free enthalpy
GI-XRD	X-ray diffraction with grazing incidence
HER	hydrogen evolution reaction
HOR	hydrogen oxidation reaction
HR-TEM	high-resolution transmission electron microscopy
i	current
ICP-OES	inductively coupled plasma optical emission spectrometry
j	current density
j_0	exchange current density
λ	wavelength
m	mass
M	mol/l
M_w	g/mol
Me	metal
Me/OMC	ordered mesoporous carbon with noble metal nanoparticles employing metal ions
MeNP/OMC	ordered mesoporous carbon with noble metal nanoparticles employing preformed colloidal nanoparticles

NLDFT	non-local density functional theory for pore size analysis (physisorption)
OER	oxygen evolution reaction
OMC	ordered mesoporous carbon
QSDFT	quenched solid density functional theory for pore size analysis (physisorption)
R	universal gas constant
RDE	rotating disc electrode
RF	resorcinol-formaldehyde
RHE	reversible hydrogen electrode
q	scattering vector
SAED	selected area electron diffraction
SAXS	small angle X-ray scattering
SEM	scanning electron microscopy
SHE	standard hydrogen electrode
TEM	transmission electron microscopy
THF	tetrahydrofuran
T	temperature
$T_{Tammann}$	Tammann temperature
θ	angle of incidence in X-ray diffraction measurements
WDX	wavelength-dispersive X-ray fluorescence spectroscopy
X	conversion
XRD	X-ray diffraction
XPS	X-ray induced photoelectron spectroscopy

1 Introduction: The electrolytic hydrogen evolution reaction

The hydrogen evolution reaction (HER) is a fundamental reaction in electrochemistry. It takes place at the cathode of an electrolytic cell. The chemical reaction is rather simple: two protons are reduced to a dihydrogen molecule employing two electrons. (equation (1))



Due to its simplicity the HER is used as a model system for material (e.g. single crystal^{1, 2}) or computational studies (e.g. quantum chemical modeling via DFT³⁻⁵). Also in the merger of synthetic and computational approaches the HER is studied to develop new catalyst materials.⁶

The relevance of the HER in the chemical industry is significant. First of all the HER is one part of the established chloralkali process to produce Cl₂ gas. Chlorine is a basic chemical compound and produced in a high quantity.⁷ The demand amounts to 60 million tons a year.⁸ Hydrogen is also a promising candidate as a key energy carrier for mobility as well as energy transport and storage^{6, 9} since it has the highest gravimetric energy density of all chemical compounds.¹⁰ Water electrolysis produces hydrogen of a high purity.¹¹ The HER takes place at the cathode and the oxygen evolution reaction (OER) produces O₂ gas at the anode.

In fact, the HER is a well-studied multi-step reaction mechanism and needs to be explained in detail. The following chapters will discuss the mechanism, thermodynamic and kinetic aspects as well as introduce state-of-the-art catalysts. The end of the chapter will focus on the challenges which are faced in the search for efficient and inexpensive catalysts for the HER. Finally, challenges, aims and an outline of this thesis are presented.

1.1 Mechanisms: Volmer, Tafel and Heyrovsky

The multi-step mechanism of the hydrogen evolution reaction (HER) can be divided into following steps. The reaction schemes show the HER in acidic solution which is similar to the processes in alkaline media.

- 1) Transport of H⁺ to the cathode's surface
- 2) Electrochemical adsorption of H⁺ on the metal's surface: Volmer reaction



3) Formation and desorption of H₂ either electrochemically (a) or chemically (b):

a) Electrochemical desorption of H₂: Heyrovsky reaction



b) Chemical desorption of H₂: Tafel reaction



4) Mass transport of H₂ away from the cathode

MeH^{*} denotes a H atom which is chemically adsorbed on an active site of a metal Me. The reaction pathway of the H₂ desorption strongly depends on intrinsic chemical and electronic properties of the catalyst.^{1, 12} The rate-controlling step of the reaction at the electrode can be determined by the so-called Tafel-slope (see Chapter 1.3).¹³

1.2 Thermodynamics and overpotential

The HER in acidic solution is set as the point of zero of the electro-potential series. The so-called standard hydrogen electrode (SHE) assumes a proton activity of $a_{\text{H}^+} = 1 \text{ mol/l}$ and a partial hydrogen pressure of $p_{\text{H}_2} = 1 \text{ atm}$. The hydrogen is bubbled into the electrolyte around a platinized platinum electrode. The half-cell potential is then defined as $E^0(\text{SHE}) = 0.00 \text{ V}$.

After a proton is electrochemically adsorbed on a metal's surface (Volmer reaction, equation (2)) the proposed mechanism in chapter 1.1 describes two competing reactions. The adsorbed H on the surface (*MeH*^{*}) can either desorb (Volmer reaction, equation (2)) or combine with another proton (Heyrovsky reaction, equation (3) or Tafel reaction, equation (4)) to form a H₂ molecule. It is important to point out the dynamic nature of this process. A good catalyst should not be bound too strong to a H atom or a formed H₂ molecule since this would block the active site and hinder the adsorption of other reactants. In case of a too weak binding affinity, no H atom adsorbs on the metal's surface preventing the formation of a Me-H bond and thus no reaction can take place. This concept is called the Sabatier principle.¹⁴

The thermodynamic expression of the Sabatier principle states that the free enthalpy change during the adsorption of H on the metal's surface should be zero.⁶ Advanced density functional theory (DFT) models confirm this assumption.¹⁵ In a reversible

electrochemical reaction with constant pressure and temperature the free enthalpy can be expressed in terms of the standard potential. (equation (5))

$$\Delta G_m = -nFE^0 \quad (5)$$

ΔG_m is the molar free enthalpy, n the number of transferred electrons, F the Faraday's constant and E^0 the standard potential. Accordingly, the thermodynamic standard potential of the hydrogen evolution reaction should be zero for a good catalyst. This is in line with the above mentioned electrode potential of the standard hydrogen electrode (SHE) which is zero per definition.

The overpotential η is defined as the deviation of the true potential from the standard potential. Active catalysts like platinum show low overpotentials in the HER. The origin of overpotentials at low currents derives from electron transfer barriers across phase boundaries. At higher currents diffusional limitations of reactants (H^+ or H_2) or a limited electron transfer during the reactions may contribute to overpotentials.

1.3 Kinetics

Julius Tafel and others around the turn of the 20th century found that the potential and the electric current show a correlation in half-logarithmic scale at low currents.^{16, 17} This behaviour can be expressed in the so-called Tafel equation (equation (6)).

$$\eta = a + b \cdot \log(j) \quad (6)$$

η is the overpotential, j the current density and b the so-called Tafel-slope (equation (7)).¹⁸

$$b = \frac{\ln(10) RT}{\alpha n F} \quad (7)$$

R is the universal gas constant, T the temperature, α the so-called charge transfer coefficient, which must be between 0 and 1 and usually is assumed to be 0.5, n is the number of transferred electrons and F the Faraday's constant.

Introduction: The electrolytic hydrogen evolution reaction

The current density j can be rewritten as a function of the overpotential η .

$$j = j_0 \exp\left(\frac{-\eta}{b}\right) \quad (8)$$

j_0 is the exchange current density. Equation (8) is valid for the cathodic regime without considering diffusional limitations.¹⁹ The Tafel slopes for the Volmer, Heyrovsky and Tafel reactions (see chapter 1.1) at room temperature can be calculated with equation (7).^{12, 13,}
18

Volmer reaction (electrochemical adsorption of H^+):

$$b = \frac{\ln(10) RT}{\alpha F} \approx 120 \text{ mV/dec}$$

Heyrovsky reaction (electrochemical desorption of H_2)

$$b = \frac{\ln(10) RT}{(1 + \alpha)F} \approx 40 \text{ mV/dec}$$

Tafel reaction (chemical desorption of H_2)

$$b = \frac{\ln(10) RT}{(2)F} \approx 30 \text{ mV/dec}$$

The abbreviation dec stands for one decade in the range of current densities.

A charge transfer coefficient α of 0.5 is assumed.¹² This assumption is valid for most cases in the HER. But α can also be temperature dependent²⁰ or can vary with unusual electrode geometries.²¹

The value of the slope in the Tafel plot (potential versus logarithmic current density) at low current densities identifies which reaction is rate-limiting in the HER. The Volmer reaction on active HER catalysts like platinum is usually considered fast.² A mechanism sequence of Volmer and Heyrovsky reaction would show a Tafel slope of 40 mV/dec and is accredited to a high hydrogen coverage at active noble metal electrodes at low overpotentials.¹³ A Volmer-Tafel reaction sequence occurs at a low hydrogen coverage of the catalyst's surface.¹³ At higher overpotentials the current becomes independent of the potentials and the b becomes infinite.¹³

The exchange current density j_0 can also be derived from the Tafel equation. It is a measure of a material's ability to catalyze the HER.¹⁵ j_0 corresponds to the intensity of charge transfer at a potential when the rate of HER is at equilibrium and no net current is observed.

1.4 Volcano plot and state-of-the-art Pt/C catalysts

As mentioned in chapter 1.2 a good catalyst follows the Sabatier principle. The free enthalpy of hydrogen adsorption should therefore be zero. Materials with a higher or lower free enthalpy of hydrogen adsorption should show a lower activity. Accordingly, a plot of the activity versus the free enthalpy should be peak shaped. Such a plot is usually called Sabatier or volcano plot.²² A detailed volcano plot from several electrochemical measurements and thermodynamic calculations was published by Trasatti in 1972.²³ In Trasatti's as well as other contributions Pt was identified as the most active monometallic HER catalyst and occupied a position near the top of the volcano.

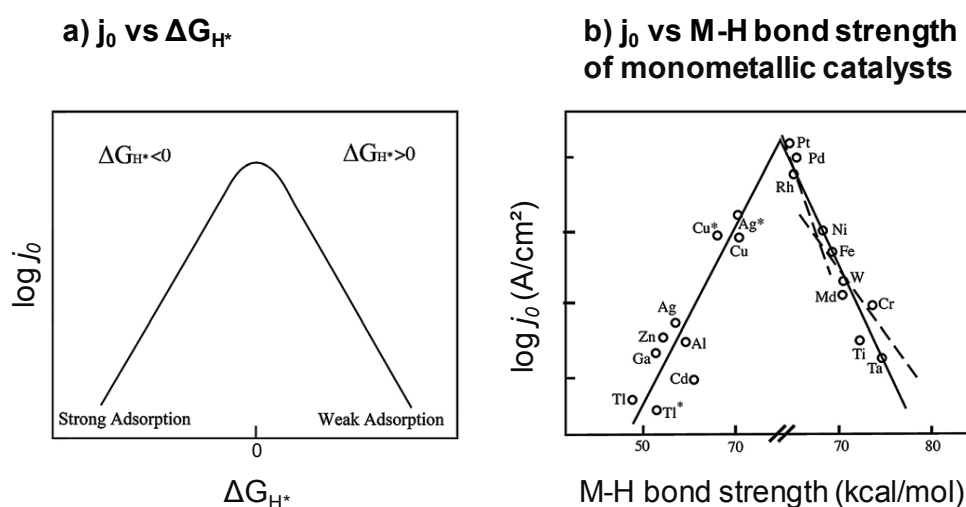


Figure 1. a) Relationship between exchange current density j_0 in logarithmic scale and free enthalpy of H adsorption ΔG_{H^*} . b) Electrochemically measured j_0 values on metals versus the strength of metal-hydrogen bond derived from the heat of hydride formation. Dependence of j_0 on ΔG_{H^*} for HER on the surface of various metals. Images were taken from Zheng et al.⁶ with granted permission of John Wiley and Sons.

Figure 1 shows two volcano plots. Figure 1a summarizes the relationship between the exchange current density j_0 and the free enthalpy of H adsorption ΔG_H . Figure 1b shows the volcano plot for monometallic HER catalysts. Pt has the highest exchange current density of all monometallic catalysts and is most proximate to the top of the volcano.²² Via a computational approach Nørskov studied all reaction steps of the HER at Pt.¹⁵ The change in free enthalpy during every step of the HER at Pt varies only weakly from 0. Nevertheless, the volcano plot suggests that there are materials which could exhibit a slightly weaker M-H bond than Pt and thus be nearer to the top of the volcano. Such materials would exhibit a higher HER activity.

The most employed catalysts for the HER in industry nowadays are Pt nanoparticles deposited or formed on conductive carbon allotropes. Pt/C catalysts can be synthesized via impregnation of a carbon support with solutions containing dissolved Pt species.

Thermal treatment converts the precursor into metallic Pt particles.²⁴⁻²⁸ Another approach is the immobilization of preformed colloidal Pt particles on carbon supports.^{29, 30} Carbon supports are typically powders of carbon nanotubes^{25, 26, 28, 30}, activated carbon²⁷ or carbon black²⁹.

The catalysts for electrolyzers need to be deposited as homogeneous and stable coatings on the cathode.³¹ Conventional electrode coatings are typically made by mixing fine-grained Pt/C powders with a binding agent (e.g. Nafion) and a solvent to form an ink. The ink is applied onto an electrode and dried. However, such coatings possess disadvantages like the blocking of pores and active sites by the binding agent, which decreases the catalyst's activity.³²⁻³⁴ Furthermore, the ink composition and distribution strongly influence the local electronic conductivity. The Nafion-based coatings are difficult to reproduce.^{35, 36} As a result the expensive and scarce Pt is often not used efficiently and the geometric Pt loadings are unnecessarily high.

The design of catalytic coatings which provide a more efficient utilization of the catalytically active component needs the identification a suitable coating material. The material should possess a low noble metal content, a high active surface area and a high stability in acidic media. One material that exhibits a high surface area and stability in acidic media is ordered mesoporous carbon.³⁷⁻⁴⁰ The next sub-chapter will give a short introduction into the properties and the synthesis of ordered mesoporous carbon coatings.

1.5 Ordered mesoporous carbon films

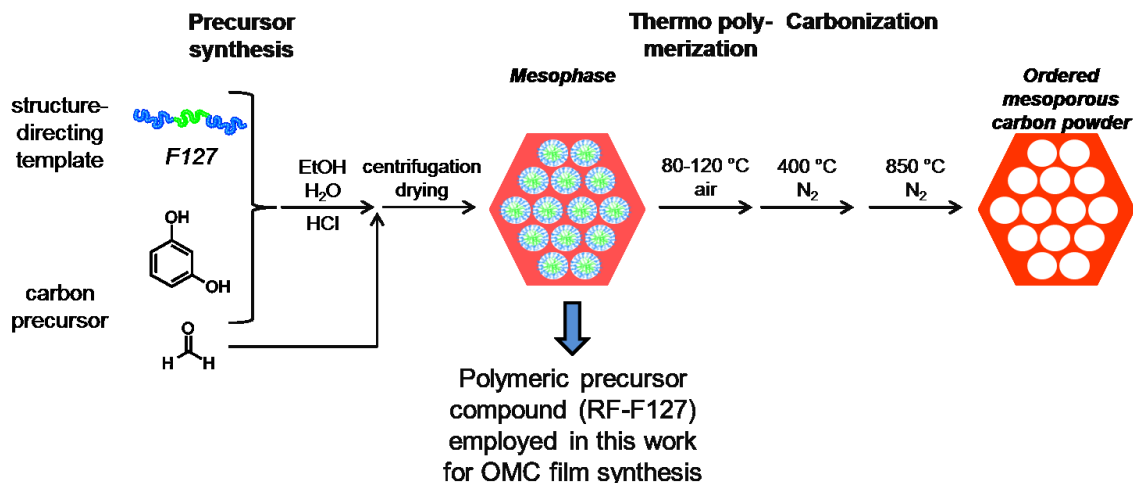
Ordered mesoporous carbon (OMC) films exhibit outstanding properties as they show a very high surface area, a tunable pore size, high porosity, chemical inertness and electrical conductivity.³⁷⁻⁴⁰ These attributes make OMC films ideal candidates for electrode coatings, membranes and catalytic coatings. In most cases a thin film geometry is desired to ensure no diffusion limitations.⁴¹ Furthermore, the presence of a substrate helps to depress the usual shrinkage of the pore walls during the carbonization step in the synthesis of OMC materials.⁴²

In the context of electrode preparation, OMC coatings provide a pathway to circumvent the use of binders like Nafion during electrode preparation. Binders are usually necessary to adhere reasonable amounts of catalyst to an electrode. Therefore, electrode coatings made from OMC films are expected to show a higher performance than carbon powders pasted with binders.⁴³

The hard-templating approach to mesoporous carbon materials with anodic aluminium oxide, zeolites, siliceous opals or silica as rigid sacrificial templates⁴⁴ has severe drawbacks as the synthesis is time consuming, costly and usually needs multiple

infiltration steps.³⁹ On the contrary, soft-templating via micelles of amphiphilic molecules is a more straightforward and facile pathway to synthesize mesoporous carbon materials.⁴⁵ In the soft-templating approach organic-organic interactions between a thermoplastic resin and a thermally-decomposable copolymer lead to an ordered nanocomposite based on the evaporation-induced self-assembly (EISA).⁴⁰ For a successful synthesis of soft-templated OMC three basic conditions need to be fulfilled: The polymer needs to get an impetus to form micelles and has to show a strong affinity to the precursor species, the precursor needs to be able to cross-link and the cross-linked precursor species has to show a higher stability than the template species during thermal removal of the template.⁴⁵ Especially due to the massive loss of volatile carbon⁴⁶ and the contraction of the system, which is more severe than for oxides⁴⁷ the preservation of the nanostructure during pyrolysis is challenging and a control of morphology and configuration difficult.⁴⁸ An understanding of OMC film fabrication is obviously required.⁴⁴

The synthesis of OMC films was first published in 2004 by Dai and co-workers.⁴⁶ They synthesized a hexagonally ordered mesoporous film by employing the block copolymer PS-P4VP as a template and the precursor molecules resorcinol and formaldehyde (RF). Another early approach was published by Tang et al. in 2005 showing uniaxially aligned lamellae of carbon by employing the special template poly(butylacrylate-*b*-acrylonitrile) (PBA-*b*-PAN).⁴⁹ The block copolymer Pluronic F127 (PEO-PPO-PEO) was first used by Tanaka with RF as a carbon precursor and triethyl-orthoacetate as co-precursor via spin-coating to form a hexagonally ordered film material, denoted as COU-1.⁵⁰ Later a similar synthesis route without triethyl-orthoacetate was established as COU-3.⁵¹ Other templates which are employed are Brij58³⁷ and P123⁴⁷. Other carbon precursor species replacing resorcinol are phloroglucinol^{44, 52}, phenol^{43, 47} or 1,5-Dihydroxynaphthalene³⁹. Formaldehyde which is necessary to induce the polymerization reaction can also be introduced in gaseous form.^{38, 53}



Scheme 1. Illustration of the synthesis approach to ordered mesoporous carbon powder as published by the Dai group.⁵⁴ The structure-directing triblock copolymer F127 (PEO-PPO-PEO) and resorcinol are dissolved in ethanol. After addition of 3 M hydrochloric acid, formaldehyde solution is added to start a polycondensation reaction. The derived polymeric resin is separated by centrifuging and deposited onto a petri dish. After thermal treatment at 100 °C in air and a subsequent carbonization under inert atmosphere (N₂) ordered mesoporous carbon (denoted as C-ORNL-1) is obtained.

In Scheme 1 a synthesis approach published by the Dai group to OMC powders is explained in detail.⁵⁴ In this thesis the conditions for the synthesis of the polycondensation product of resorcinol and formaldehyde together with F127 (RF-F127) are adapted. The polymeric compound will be used as carbon precursor for the OMC film synthesis.

OMC coatings show optimal properties as a support for catalytically active nanoparticles. The next sub-chapter will summarize synthesis approaches to metal-containing OMC powders and films reported in literature. Furthermore, it will focus on the challenges which are faced when active metal species are introduced into the carbon network.

1.6 Introduction of catalytically active metals into OMC films

Metal species can be introduced into the OMC networks as salt precursors or preformed metal nanoparticles during the synthesis process. The main drawback when introducing metal ions, on the one hand, is a severe aggregation with broad size distribution or less controllable size of the final metal particles.⁵⁵ On the other hand, the stabilizing agents of the metal nanoparticles often prevent a dispersion in the solution of carbon precursor and template.⁵⁵

Jaroniec and co-workers published a synthesis strategy to incorporate alumina and silica nanoparticles into soft-templated mesoporous carbon.⁵⁶ Later, they extended the approach to the incorporation of nickel and nickel oxide nanoparticles.⁵⁷ Nanoparticles were suspended together with phloroglucinol and the template polymer (F127) in ethanolic solution. After addition of HCl and subsequent addition of formaldehyde the polymer compound was separated and thermally treated.

In literature there are various examples for the introduction of metal species into OMC networks. Many kinds of metal species in OMC powder materials like Fe and Fe₂O₃^{58, 59}, TiO₂⁶⁰, Ni⁶¹ or noble metals like Ir⁶², Ru⁶³, Pd⁶⁴ and Pt⁶⁴ were shown. However, reports of a successful synthesis of metal-containing OMC films are uncommon. The group of Vogt recently presented the successful synthesis of cobalt oxide and vanadia containing OMC films.^{65, 66} The incorporation of the oxide particles into OMC films succeeded via co-deposition of the polymer precursor and ions as metal precursors and adapted subsequent thermal processing steps. Nevertheless, no synthesis of noble metal containing OMC films has been published so far.

1.7 Challenges, aims and structure of this thesis

This work aims to develop synthesis routes to noble metal containing OMC films, elucidate their structural properties and investigate their HER activity. The new synthesis approach is based on the dissolution of the RF-F127 polymer compound (see Scheme 1) in a THF-based solution or colloid. After film deposition via dip-coating and carbonization a mesoporous carbon film is obtained containing the metal species.

Challenges

The presence of the catalytically active metal species may have a detrimental effect on the ordered mesostructure and porosity of the OMC film. All the same, it is necessary to maintain the well-defined structure in order to enable the transport of protons to and of dihydrogen molecules away from the active site (step 1 and 4 of the proposed mechanism sequence in chapter 1.1). In order to increase the active surface area it is crucial to obtain a small nanoparticle diameter when the amount of employed noble metal shall be reduced. As the carbonization temperature is rather high (≥ 600 °C) sintering of the nanoparticles may occur.

Aims

Maintaining control over the size of the nanoparticles as well as the size and connectivity of the supports pore structure can clearly help in the optimization of supported catalyst.^{67, 68} Controlled deposition of particles inside mesopores with appropriate pore size can also exert a significant confinement effect, which drastically reduces sintering and degradation phenomena encountered under typical conditions of heterogeneous catalysis⁶⁹ and electrocatalysis.⁷⁰ This work shall develop improved synthesis procedures for electrocatalytically active coatings which provide (i) a high surface area with controlled interconnected pores, (ii) high accessibility to the supported nanoparticles, (iii) good electronic conductivity and (iv) homogenous catalyst layers without the need for binding

agents. Catalyst with these structural properties should reach high catalytic activities. The main aim of this work is the synthesis of catalysts with low Pt loadings and high HER activities at low overpotentials. Optimal conditions for carbonization will be identified as well as requirements for a successful synthesis. Synthetic aspects like the influence of the metal species and the metal weight loading will be studied. Furthermore, this work addresses kinetic aspects like the rate-determining step during the HER.

Structure of the presented results

This work will describe mono- and bimetallic OMC films and their electrocatalytic performance in the hydrogen evolution reaction (HER). The metal component is introduced either as a dissolved metal ion (**Me/OMC, route 1**) or as preformed nanoparticles (**MeNP/OMC, route 2**) in the film synthesis.

The synthesis strategy, the film morphology and the catalytic activity of films synthesized via route 1 will be discussed for Pd/OMC films in chapter 3, for Pt/OMC films in chapter 4 and for Ru/OMC films and bimetallic RuPt/OMC films in chapter 5.

The activity in heterogeneous catalysis will exemplarily be studied for one film species: the performance of Pd/OMC in the hydrogenation of butadiene (see chapter 3). Chapter 4 discusses in detail the influence of the carbonization temperature on particle and film morphology and electrocatalytic activity. Chapter 5 focusses on the particle composition of nanoparticles of the bimetallic approach (RuPt/OMC).

The film synthesis via route 2 (preformed nanoparticles) is described in chapter 6. It will describe the colloid synthesis and present physico-chemical characterization of Pt colloids, the carbonized PtNP/OMC film and discuss the electrocatalytic performance in the HER.

A general discussion about OMC films is given in chapter 7. The influence of the employed precursor species, the particle composition and kinetic aspects will be discussed. Furthermore, OMC catalyst films will be compared to catalysts described in literature, especially in terms of Pt content and activity. The last chapter (8) will summarize the outcome of the presented studies, give a conclusion and give ideas for further research.

Chapter 3 and 4 of this work are submitted to peer-reviewed scientific journals. A reference to the journal is given on the first page of the corresponding chapter.

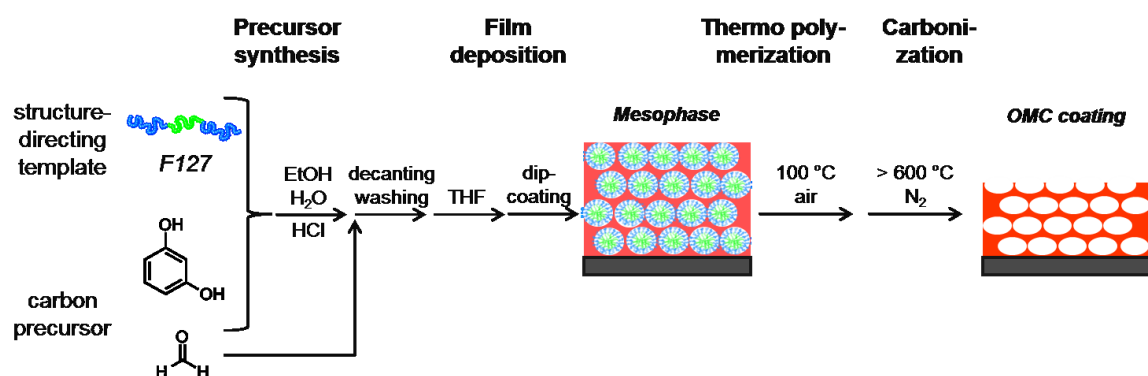
2 Experimental

This chapter explains the synthesis for metal-free OMC films (sub-chapter 2.1), as well as the new synthesis concepts for Me/OMC films (route 1, sub-chapter 2.2) and MeNP/OMC films (route 2, sub-chapter 2.3). Chapter 2.4 describes the electrochemical setup and the measuring procedure to determine the HER activity. Chapter 2.5 will present physico-chemical characterization of a metal-free OMC film.

Information about the supplier of the employed chemicals, exact amounts employed in the syntheses and details about the physico-chemical characterization of Me/OMC and MeNP/OMC films are given in the experimental parts of chapters 3, 4, 5 and 6.

2.1 OMC film synthesis

The employed synthesis of OMC films is based on a polymer preparation technique with resorcinol and formaldehyde as carbon precursor species and F127 as structure-directing agent. The synthesis of the carbon precursor compound was described by the Dai group (see Scheme 1).⁵⁴ The film synthesis is presented in Scheme 2. The dissolution of phenolic resin together with a structure-directing block copolymer was already described by Valkama et al.⁷¹



Scheme 2. Illustration of the synthesis approach to ordered mesoporous carbon films. The structure-directing triblock copolymer F127 (PEO-PPO-PEO) and resorcinol are dissolved in ethanol. After addition of hydrochloric acid, formaldehyde solution is added to start a polycondensation reaction. The derived polymeric resin is separated by centrifuging and then washed. The polymeric compound is redissolved in THF. Under controlled conditions a film is deposited via dip-coating to obtain a homogeneous mesophase film. After thermal treatment at 100 °C in air and a subsequent carbonization under inert atmosphere (N₂) a OMC film is obtained.

Chemicals

MilliQ water was employed for all synthesis procedures. Ethanol (EtOH, >99.9%, absolute) was obtained from VWR and tetrahydrofuran (THF, >99.9%, absolute) from Roth. Resorcinol and formaldehyde (37 wt% in water) and Pluronic F127

(PEO₁₀₆-*b*-PPO₇₀-*b*-PEO₁₀₆, $M_w = 12\,600$ g/mol) were purchased from Sigma-Aldrich. 3 M hydrochloric acid (HCl) was prepared from 12 M HCl (Alfa Aesar). All chemicals were used without further purification.

Pretreatment of substrates

Catalyst films were synthesized on different substrates, i.e. single side polished and double side polished Si wafer with (100)-orientation (University Wafers) and SiO₂ glass microscopy slides (Science Services). Si wafer substrates were cleaned with a tissue containing ethanol and calcined in air (2 h, 600 °C) prior to film deposition. SiO₂ glass substrates for conductivity measurements were ultrasonicated in ethanol and then wiped with a tissue containing ethanol prior to coating.

OMC film synthesis

1.1 g of resorcinol and 300 mg of F127 were placed in a centrifuge vial. 4.5 mL of EtOH was added and the vial was shaken until a clear solution was obtained. Thereafter, 4.5 mL of 3 M HCl was added. The mixture was shaken on a roller mixer for five minutes. 1.2 ml of formaldehyde (37% in water) was added at once and mixed with a vortex for 2 min and again shaken on a roller mixer. Circa four minutes after addition of formaldehyde, the solution became turbid. Ten minutes after the addition, a white precipitate was separated from the mixture by centrifugation at 7500 rpm for 10 min and the top-layer solution was discarded. The white precipitate was washed with water, again separated by centrifugation and after that dissolved in 5 mL of THF. A clear yellow dispersion was obtained and used for dip-coating. Films were deposited via dip-coating at 25 °C and 30% relative humidity. The coated substrates were thermally treated at 100 °C for 12 h, followed by carbonization at 600 °C for 3 h in nitrogen atmosphere (heating ramp of 1 K/min). Corresponding powder was prepared by drying the dip-coating suspension in a crucible with an identical thermal treatment as the films.

Physico-chemical characterization

SEM images were collected on a JEOL 7401F at 10 kV. Image J program, version 1.39u (<http://rsbweb.nih.gov/ij/>), was employed to determine from the images the pore diameter, film thickness and to obtain fast Fourier transformed (FFT) images. TEM images were recorded on a FEI Tecnai G² 20 S-TWIN operated at 200 kV on fragments of film samples scraped off the substrates and deposited on carbon-coated copper grids.

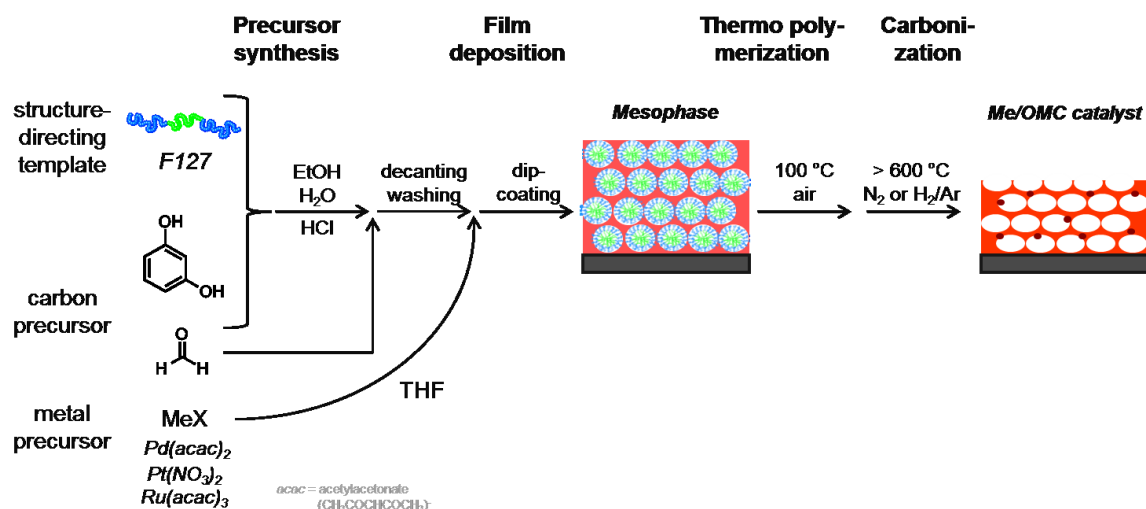
Films coated on thin silicon wafers (50 μm) were used for 2D-SAXS measurements. 2D-SAXS patterns were collected at the B03 beamline at DESY (synchrotron facility in Hamburg, Germany) with a calibrated radiation energy of 12.956 keV. The SAXS data were processed employing the software FIT2D Version V12.077.

The surface area of OMC film samples coated on both sides of double side polished silicon wafers was analyzed by N₂ physisorption. Isotherms were recorded at 77 K with a Quantachrome Autosorb-iQ. The samples were degassed in vacuum at 150 °C for 2 h prior to physisorption analysis. The surface area was evaluated with BET.

The electrical conductivity of OMC films on SiO₂ substrates was measured with a Keithley Model 6517B Electrometer employing an 8x8 pin probe head with an alternating polarity sequence of the pins.

2.2 Me/OMC film synthesis

The synthesis of Me/OMC films involves the co-deposition of metal ions with a compound consisting of a resin together with a polymer template (F127). A compound of a polymer template (F127) and a resin of resorcinol and formaldehyde is dispersed in a THF solution containing a soluble metal ions. Mesoporous films are deposited via dip-coating with this solution. After thermopolymerization at 100 °C and a subsequent carbonization in inert atmosphere homogeneous and electrically conductive carbon films with an ordered pore system are obtained. The described synthesis is marked as **route 1**. Details about the detailed syntheses are given in the experimental parts of the following chapters.

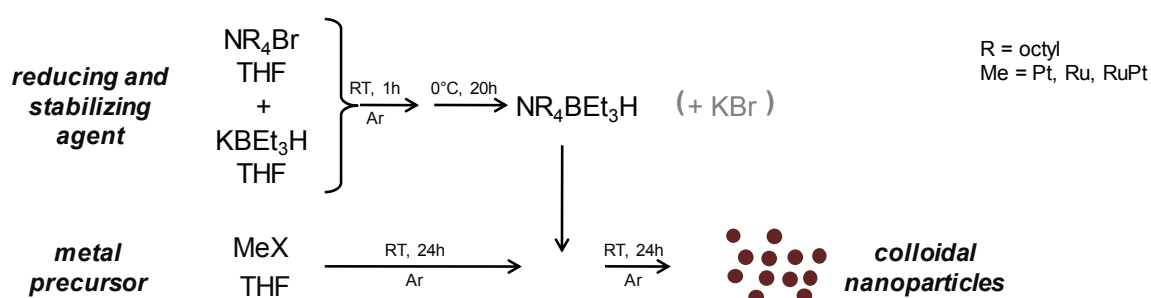


Scheme 3. Illustration of the synthesis approach to mesoporous Me/OMC catalyst films. The structure-directing triblock copolymer F127 (PEO-PPO-PEO) and resorcinol are dissolved in ethanol. After addition of hydrochloric acid, formaldehyde solution is added to start a polycondensation reaction. The derived polymeric resin is separated by centrifuging and then washed. The polymeric compound is redissolved in a metal precursor containing THF solution. Under controlled conditions a film is deposited via dip-coating to obtain a homogeneous mesophasic film. After thermal treatment at 100 °C in air and a subsequent carbonization under inert or reducing atmosphere (N₂ or H₂/Ar) a mesoporous Me/OMC film is obtained. The described synthesis is marked as route 1.

2.3 MeNP/OMC film synthesis

This work reports also the first synthesis of mesoporous MeNP/OMC catalyst films with colloidal size-controlled noble metal nanoparticles being employed as metal precursor. The synthesis succeeded by the co-deposition of preformed nanoparticles dispersed in THF along with a polymer resin consisting of resorcinol-formaldehyde and a structure-directing agent (Pluronic F127). The synthesis of colloidal metal particles in THF proves to be vital for the film preparation in order to provide the compatibility between the colloid and the polymer resin solution and retain the ability to form a micelle-structured mesophase.

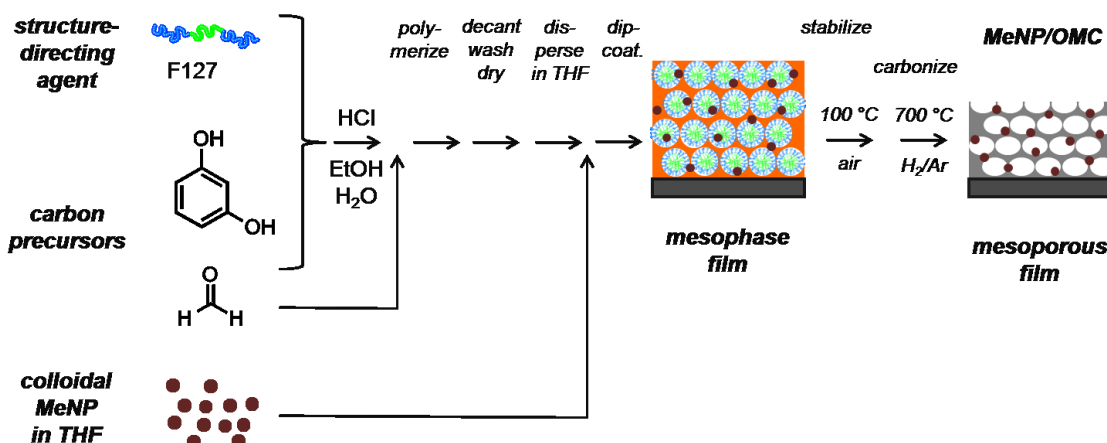
The deduced procedure for colloid synthesis is based on recipes published by Bönemann and co-workers⁷²⁻⁷⁴ as briefly summarized in Scheme 4. First, tetraoctylammoniumtriethylhydroborate ($N(\text{octyl})_4\text{BEt}_3\text{H}$) is synthesized by mixing tetraoctylammonium bromide (TOAB) in THF with potassium triethylborohydride (KBEt_3H) in THF at room temperature in Ar atmosphere. After 20 hours at circa 0 °C KBr is removed by filtration. The freshly prepared $N(\text{octyl})_4\text{BEt}_3\text{H}$ is then added to a metal precursor (i.e. a metal salt) dispersed in THF. $N(\text{octyl})_4\text{BEt}_3\text{H}$ serves as reducing and stabilizing agent (see chapter 6.2 for details).^{74, 75} According to Bönemann, the metal precursor does not need to be completely dissolvable in THF. For example, PtCl_2 is only partially dissolvable in THF. After addition of the reducing and stabilizing agent the precursor gets gradually dissolved until the reduction is completed.



Scheme 4. Illustration of the synthesis approach employed to colloidal noble metal nanoparticle in THF.^{74, 75} The stabilizing and reducing agent $N(\text{octyl})_4\text{BEt}_3\text{H}$ is formed by mixing TOAB in THF with KBEt_3H in THF at room temperature in Ar atmosphere. After 20 h at circa 0 °C KBr is removed by filtration. Colloidal nanoparticles are synthesized by dispersing an ionic metal precursor in THF and addition of a freshly prepared solution of $N(\text{octyl})_4\text{BEt}_3\text{H}$ in THF. After mixing for 24 h at room temperature the Pt colloid is obtained.

Colloidal nanoparticles in THF serve as metal precursor for the MeNP/OMC synthesis as illustrated in Scheme 5. The first synthesis step comprises the dissolution of the template (triblock copolymer Pluronic F127) and resorcinol in ethanol. HCl and formaldehyde solution are added to initiate a polycondensation reaction. The formed polymer resin is separated, washed and freeze-dried and then redissolved in THF. The MeNP colloid is

added to this mixture and then employed for film casting via dip-coating. The derived films are thermally treated at 100 °C in air to improve crosslinking and stabilize the films. Subsequent carbonization under inert gas flow at 700 °C results in template removal and formation of a highly conductive and graphitized PtNP/OMC film. The described synthesis is marked as **route 2**. Details about the syntheses are given in the experimental parts of the following chapters.



Scheme 5. Illustration of the synthesis approach employed to mesoporous MeNP/OMC catalyst films. The structure-directing triblock copolymer F127 (PEO-PPO-PEO) and resorcinol are dissolved in ethanol. After addition of hydrochloric acid formaldehyde solution is added to start the polycondensation reaction. The derived polymeric resin is separated by centrifuging, washed and freeze-dried. The polymeric compound is redissolved in THF and the Pt colloid added. Under controlled conditions a substrate is dipped into the mixture to obtain a homogeneous mesophasic film. After thermal treatment at 100 °C in air and a subsequent carbonization under inert atmosphere at 700 °C for 3 h a mesoporous PtNP/OMC film is obtained. The described synthesis is marked as **route 2**.

2.4 Electrocatalytic testing

All electrocatalytic testing was performed in 0.5 M H₂SO₄ electrolyte (Fixanal, Fluka Analytical) using a three-electrode disc setup (Pine MSR rotator, BioLogic SP-200 potentiostat) with a reversible hydrogen electrode "RHE" (Gaskatel, HydroFlex) as a reference, Pt gauze (Chempur, 1024 mesh cm⁻², 0.06 mm wire diameter, 99.9%) as counter electrode and coated GC discs rotated at 2000 rpm as working electrode. All potentials in this work are referenced to the RHE corrected.

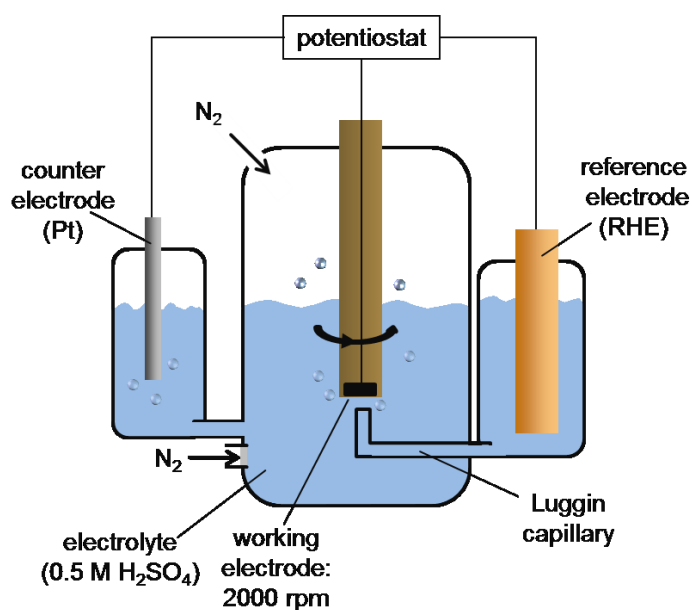


Figure 2. Electrochemical RDE setup used for studying the activity of catalysts in the HER. Coated glassy carbon discs served as the working electrode. Platinum gauze was used as a counter electrode. The applied potential is referred to a reversible hydrogen electrode and corrected for ohmic losses. Electrochemical testing was performed in N₂ purged 0.5 M H₂SO₄.

The working electrodes were prepared by cutting 6 mm circular discs from larger coated glassy carbon substrates. Prior to catalytic testing the electrolyte solution was purged for at least 30 min with nitrogen. The HER performance was assessed recording 50 cyclic voltammograms in a potential regime between 50 and -210 mV vs. RHE at a scan rate of 20 mV s⁻¹. Impedance spectra were recorded prior to CV testing to enable a correction for ohmic losses.

2.5 Morphology of an OMC film

The following section describes the morphology of typical OMC films and elucidates the impact of carbonization conditions on the films' physico-chemical properties.

Physico-chemical characterization of an OMC film is presented in Figure 3: Top-view (a) and cross-section (b) SEM image, TEM image (c) of a scraped off film sample, corresponding 2D-SAXS patterns (d and e) measured in transmission with a X-ray incident angle of $\beta = 90^\circ$ and 10° and a X-ray diffraction pattern (f).

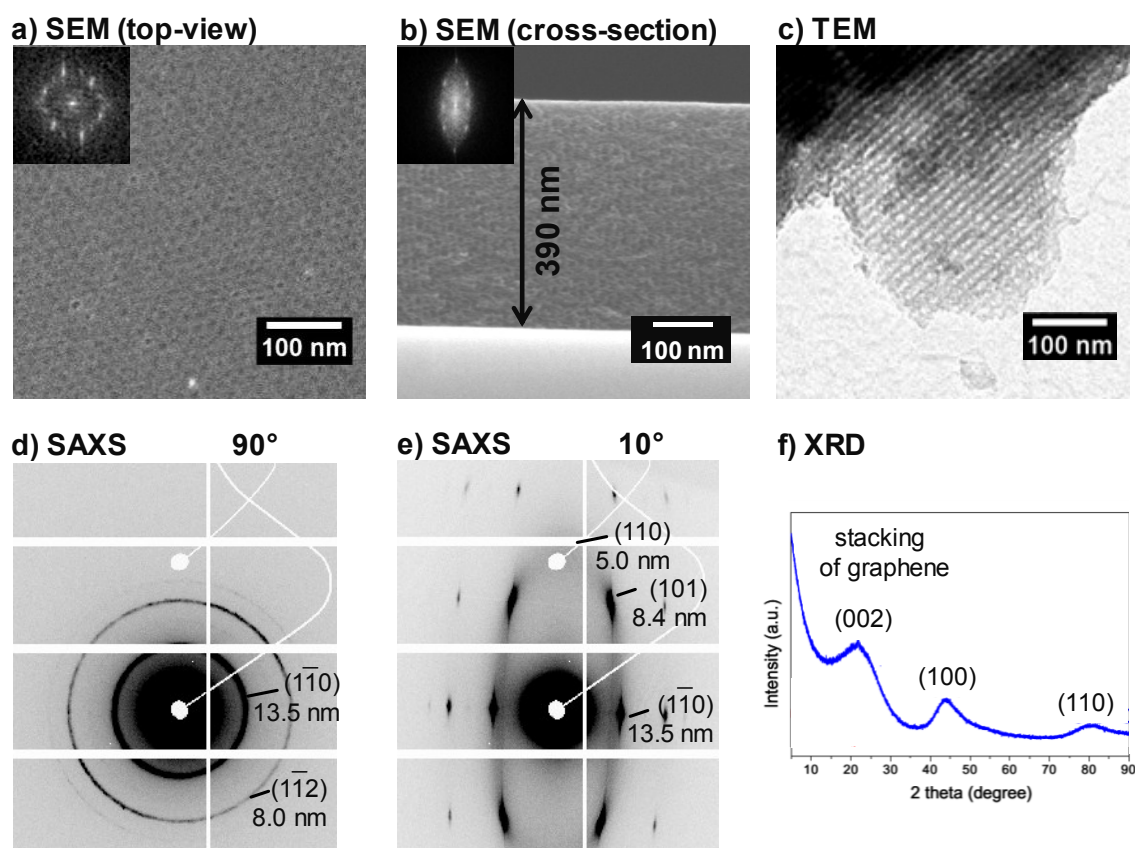


Figure 3. SEM, TEM, SAXS and XRD characterizations of a F127-templated OMC film, carbonized at 800°C in N_2 atmosphere. a) Top-view SEM image with FFT inset, b) cross-section SEM image with FFT inset, c) TEM micrograph in bright field mode, 2D-SAXS pattern recorded in transmission mode with an incident angle of 90° (d) and 10° (e) and f) XRD pattern in 2θ region of 5° to 50° with indicated reflections of stacking of graphene.⁷⁶ Images c) and f) were taken from an equally synthesized sample, published in ⁷⁷.

The top-view SEM image (Figure 3a) shows a homogeneous surface of mesopores (black spots) arranged at the surface plane. The average diameter of the mesopores amounts to 7 nm. A FFT (inset in Figure 3a) of the SEM image shows bright spots arranged on a ring, indicating the high ordering of the mesopores. The corresponding pore spacing amounts to circa 14 nm. Cross-section SEM images (Figure 3b) confirm a homogeneous film thickness (ca. 390 nm). Ordered mesopores are arranged throughout the film volume. The

mesopores show an ellipsoidal shape. A FFT (inset in Figure 3b) of the SEM image shows bright spots arranged on an ellipsoidal ring. The TEM image (Figure 3c) reveals a domain of a highly ordered arrangement of mesopores with 8 nm in diameter.

The pore ordering is studied in detail by SAXS (Figure 3d and e) recorded in transmission mode (90° and 10° in respect to the film surface). The measurement in 90° (Figure 3d) shows an isotropic ring which can be attributed to the $(1\bar{1}0)$ and the $(1\bar{1}2)$ planes of the pore system with a periodic distance of 13.5 nm. The SAXS pattern recorded in a tilted incidence angle of 10° (Figure 3e) show an ellipsoidal diffraction ring. Scattering spots on the ring can be attributed to lattice planes: $(1\bar{1}0)$ with a periodic distance of 13.5 nm and (101) with a periodic distance of 8.4 nm. The (110) plane which is perpendicular to the substrate's surface is only indicated. The regular pore distance perpendicular to the substrate amounts to 5.0 nm. Accordingly, the film contracted about 63% in perpendicular direction to the surface after template removal and carbonization. This phenomenon also explains the ellipsoidal shape of the FFT of the cross-section SEM image (inset in Figure 3b). This anisotropic film shrinkage is a common phenomenon for films templated by polymer micelles and described for metal oxide⁷⁸⁻⁸⁰ and carbon^{44, 45, 81} films. During thermal removal of the template micelle the film contracts unidirectionally and the mesopores flatten. The BET surface area was determined by N_2 physisorption. An OMC film carbonized at 800°C with a film thickness of 390 nm has a BET surface area of 370 m^2 per cm^3 film volume. Assuming a film density of circa 1.1 g/cm^3 (from WDX/StrataGem measurements of similar films) a surface area of $340\text{ m}^2/\text{g}$ can be estimated.

X-ray diffraction gives information of the degree of graphitization of the polymer network. In Figure 3f a diffractogram is shown. Three weak and broad diffraction signals are observed at $2\theta = 24^\circ$, 44° and 84° . The reflections can be assigned to disordered graphene stacks. The (002) lattice plane of disordered graphene stacks shows a maximal reflection at 24° .⁷⁶

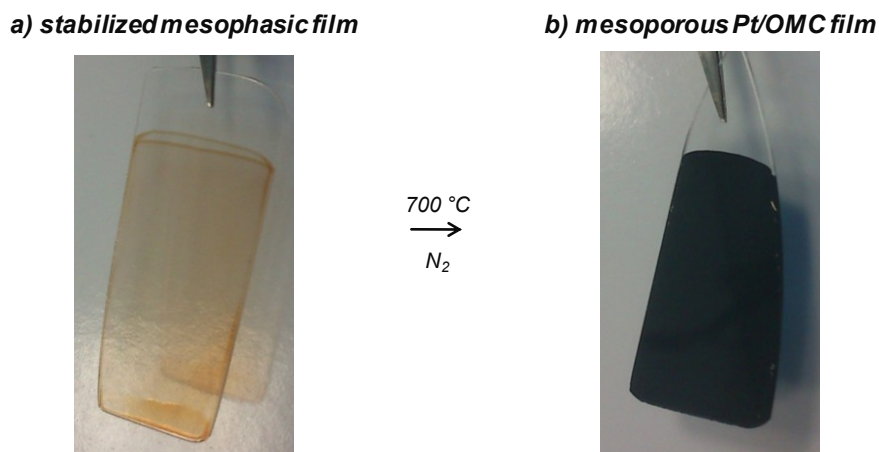


Figure 4. Photographs of Pt-containing films prepared according route 1 on SiO₂ glass substrates. a) As deposited mesophasic film after thermal treatment at 100 °C is presented. b) A Pt/OMC film after carbonization for 3 h at 700 °C in N₂ atmosphere. The film thickness of the carbonized film (b) amounts to circa 950 nm.

Photographs of Pt-containing films prepared via route 1 (Scheme 3) before and after carbonization treatment (700 °C in N₂ atmosphere) are shown in Figure 4. The films were deposited on SiO₂ glass substrates. Before carbonization (Figure 4a) the film is transparent and has a faint orange color. At the bottom and sides of the substrate edge effects are visible. These regions with thicker film are typically observed for dip-coated films.^{82, 83} After carbonization the film becomes black and nontransparent. The color indicates a graphitization of the polymer network. The certain degree of graphitization is attended by an increased electrical conductivity which is crucial for a high performance as an electrocatalyst. The color of the non-carbonized film changes slightly from dark yellow for OMC films without noble metal, via orange for Pt and Pd to a vinaceous color for Ru containing films. After carbonization all types of OMC films turn black. Altogether, the combined results prove the successful synthesis of crack-free OMC films with templated mesoporosity. An ordered cubic pore structure was obtained with pores accessible to N₂. The films show a significant degree of graphitization.

Influence of the carbonization temperature

A highly-active electrocatalyst requires a high electrical conductivity of the carbon support. The conductivity is strongly affected by the applied carbonization temperature via the resulting degree of graphitization as well as the detrimental effect of film degradation. The influence of carbonization temperature on film morphology, BET surface area and electrical conductivity was studied for OMC films carbonized at 400, 600, and 800 °C.

Figure 5 presents SEM images in top-view (a), BET surface area values from N₂ physisorption measurements (b) as well as the electrical conductivity (c) for differently carbonized OMC films. Top-view SEM images (Figure 5a) show that the films porosity progressively evolves with increasing carbonization temperature. At 400 °C only a very faint contrast indicative of mesopore formation can be seen. However, above 600 °C

pores and pore wall become clearly visible. Carbonization at 800 °C induces some collapse of pore walls on the films outer surface but in general the film morphology stays intact.

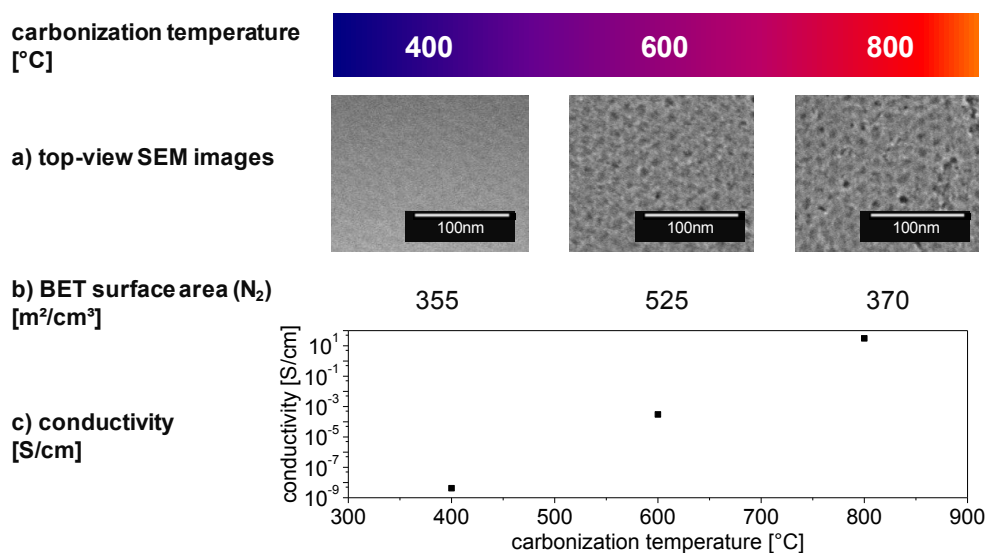


Figure 5. Influence of the carbonization temperature on F127-templated OMC films. The films were carbonized in N₂ atmosphere for 3 h: a) top-view SEM images, b) BET surface area from N₂ physisorption measurements, c) electron conductivity from sheet conductivity measurements.

The BET surface area (Figure 5b) of a film carbonized at 400 °C amounts to 355 m² per cm³ film volume. At 600 °C the surface area is higher with 525 m²/cm³ and at 800 °C the surface area diminishes to 370 m²/cm³. The maximal BET surface area at 600 °C can be attributed to an increased formation of micropores which are lost due to degradation at 800 °C. However, all studied thermal treatments produced a highly porous structure.

Electrocatalysis requires that the catalyst support is sufficiently conductive. Figure 5c shows the impact of carbonization temperature on the films' electrical conductivity (log scale). Starting out with films of very low conductivity at 400 °C (4 × 10⁻⁹ S/cm) the observed conductivity progressively increases at 600 °C (3 × 10⁻⁴ S/cm) and 800 °C carbonization temperature (30 S/cm) by ten orders of magnitude. At 800 °C the OMC film is highly conductive. The values are in good agreement with values reported for similar mesoporous carbon films (20 S/cm after carbonization at 800 °C).⁸⁴⁻⁸⁶

The combined evidence suggests that the formation of a highly conductive carbon support with open porosity requires a temperature above 600 °C. However, temperatures exceeding 800 °C may induce detrimental effects such as degradation of the pore walls and loss of microporosity. A detailed study will analyze the impact of the carbonization temperature on Pt/OMC coatings in chapter 4. (see Figure 10 and Supplement Figure S7).

3 Pd-containing mesoporous carbon films

Reprinted with permission from
ACS Catalysis, **2016**, 6 (12), pp 8255–8263.
Copyright 2017 American Chemical Society.
DOI: [10.1021/acscatal.6b02240](https://doi.org/10.1021/acscatal.6b02240)

Received: 5th of August 2016

Published online: 11th of November 2016

Published in print: 2nd of December 2016

This dissertation was handed in on the 11th of October 2016. The herein presented version of the said research article contains small modifications as it represents its state before peer-revision.

Highly active binder-free catalytic coatings for heterogeneous and electro catalysis: Pd on mesoporous carbon and its application in butadiene hydrogenation and hydrogen evolution

Denis Bernsmeier¹, Laemthong Chuenchom^{1,2}, Benjamin Paul¹, Stefan Rümmler³,
Bernd Smarsly², Ralph Kraehnert¹

¹ Department of Chemistry, Technische Universität Berlin, Straße des 17. Juni 124, 10623 Berlin

² Institute of Physical Chemistry, Justus Liebig Universität, Heinrich-Buff-Ring 58, 35392 Giessen

³ Institute of Chemistry, Martin-Luther-Universität Halle-Wittenberg, von-Danckelmann-Platz 4,
06120 Halle

Abstract

Heterogeneous catalysis performed in wall-coated reactors as well as electrocatalysis require homogeneous catalytic coatings with high surface area and good accessibility of the active sites. Conventional coating methods necessitate the use of binder components that often block pores and active sites, which limits catalytic efficiency and utilization of expensive active metals.

We report a new approach for the direct and binder-free synthesis of chemically, mechanically and thermally stable catalytic coatings based on ordered mesoporous carbon films employed as catalyst support. The synthesis relies on the codeposition of a structure-directing agent and small clusters of polymeric carbon precursors along with metal ions on a substrate. A sequence of thermal treatments converts the polymer into partly graphitized carbon, decomposes the structure-directing agent and converts the metal precursor into highly active nanoparticles.

Synthesis and catalytic applications are exemplarily demonstrated for Palladium on carbon, a system widely used in heterogeneous and electro catalysis. The obtained catalysts provide significantly higher space-time-yields in the selective gas-phase hydrogenation of Butadiene than all reported Pd/C catalysts while at the same time retaining isothermal reactor conditions. Moreover, when tested in the electro-catalytic hydrogen evolution reaction HER, the catalysts outperform reported Pd/C catalysts by a factor of three, which underlines the benefits of the developed binder-free catalyst system.

Key words: catalyst synthesis, Nafion, carbon, palladium, HER, butadiene hydrogenation

3.1 Introduction

Finely divided noble metals such as palladium are excellent catalysts for a wide range of chemical reactions. In heterogeneous catalysis supported Pd particles are employed e.g. in automotive catalytic converters⁸⁷ as well as numerous hydrogenation⁸⁸⁻⁹² and dehydrogenation²⁰ catalysts. In electrochemistry Pd catalyzes the hydrogen evolution reaction^{93, 94}, the oxygen reduction reaction⁹⁵ as well as oxidation reactions⁹⁶. Most of these catalysts use carbon as a support material due to its high abundance, stability and electrical conductivity.^{4, 12}

Fast and highly exothermic Pd-catalyzed reactions in heterogeneous catalysis typically require the catalyst to be present in the form of a wall-coating. Such coatings can transport the heat of reaction efficiently from the catalyst, thus avoiding hot-spot formation.⁹⁰ Moreover, nanostructured porous coatings can provide a rapid mass transfer, which is required for efficient catalyst utilization.^{1, 97} Catalysts prepared on electrode plates in the form of surface coatings are also essentially required in electro catalysis. These coatings need to assure the rapid transport of electrons towards the active sites, but should provide also good accessibility and short diffusion paths for electrolyte and product species.⁴⁰

The most prominent technique to produce catalytic coatings for heterogeneous catalysis is so-called wash-coating.¹⁸ Common synthesis methods employ a slurry prepared from fine-grained catalyst powders, a binder material and a solvent for deposition of the coating. Typical oxide-based catalysts include micron-sized (Pt/Al₂O₃, Rh/Al₂O₃², Al₂O₃⁷) or ball-milled (Al₂O₃¹⁵, Pd/Na-Al-Si-O_x¹⁴) powders of noble metals supported on oxides. Smaller sized particles are obtained from sols (Al₂O₃^{5, 9}, SiO₂⁵, TiO₂⁵, CeO₂¹⁷) with addition of active metal species prior to⁹ or after deposition¹⁷, followed by calcination and reduction.

The most common way for the preparation of electrode coatings is the mixing of carbon-based catalyst powders and an ionomer binder (e.g. Nafion) with a solvent to form an ink. The ink is cast onto the electrode and dried. Unfortunately, binders such as Nafion can block pores and active sites and therefore degrade the coatings performance.^{21, 23, 32} Other challenges include the homogeneity of ink composition and coating, which critically influences the resulting electrical conductivity of the deposited film and makes the accurate and reproducible synthesis of electrode coatings rather challenging.^{6, 36}

Binder-free coatings of carbon have been reported in the form of so-called "ordered mesoporous carbon" (OMC), a carbon material with templated mesoporosity that combines a number of properties desired in catalysis, i.e. high surface area, tuneable pore size, high porosity, chemical inertness and electrical conductivity.³⁷⁻⁴⁰ These attributes make OMC films ideal candidates as catalyst support materials for electrodes,

membranes and wall-coated reactors in heterogeneous catalysis. However, suitable ways of introducing active sites such as particles of noble metals are required.

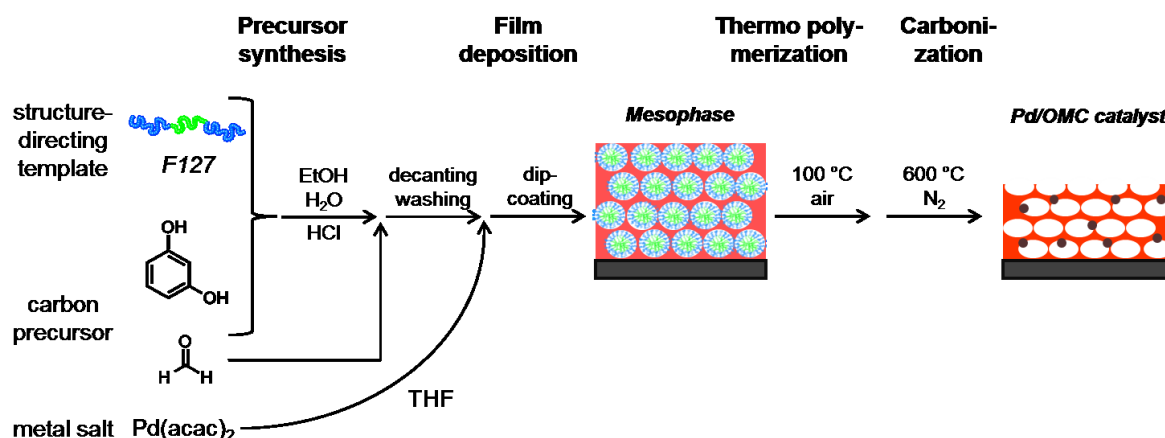
OMC materials are accessible via soft-templating with micelles of block copolymers. Parameters like pore size and degree of graphitization are can be finely tuned.⁹⁸ Furthermore heteroatom-doping of the carbon network and surface modifications are accessible.^{45, 81}

Common methods for the synthesis of films of ordered mesoporous carbon employ micelles of amphiphilic molecules deposited along with small clusters of a polymeric resin.⁴⁵ Interactions between the thermoplastic resin and a thermally decomposable copolymer during evaporation-induced self-assembly (EISA) result in formation of an ordered nanocomposite film. Subsequent heat treatments stabilize the polymeric framework, decompose the template molecules and finally transform the remaining polymer into a porous carbon material.⁴⁰ A variety of precursors, solvents and structure-directing agents can be used from the film synthesis. Dai and co-workers⁴⁶ synthesized hexagonally ordered mesoporous film employing PS-P4VP as a template. Tanaka et al. reported hexagonally ordered carbon films (COU-1) using Pluronic F127 (PEO-b-PPO-b-PEO) as template.⁵⁰ Other templates include Brij58³⁷ and Pluronic P123⁴⁷. Resorcinol^{46, 50, 51}, phloroglucinol^{44, 52}, phenol^{43, 47} and 1,5-Dihydroxynaphthalene³⁹ together with formaldehyde^{38, 53} can be used as precursors.

The synthesis of templated OMC films has at least three basic requirements⁴⁵, all of which could be significantly influenced by the additional presence of metal species: 1) The template polymer needs to assemble with the precursor clusters to form an ordered mesophase, 2) the template needs to decompose at a lower temperature than the cross-linked precursor, and 3) the formed pore structure needs to be retained despite a massive loss of volatile species⁴⁶ and contraction of the system⁴⁸ during the final pyrolysis step. A catalytically active metal could be incorporated into the film synthesis in two different ways, either as a dissolved metal salt or as preformed metal nanoparticles dispersed in the solution that is used for film casting. Major challenges result from a severe aggregation and sintering of dissolved metal species during carbonization (> 600 °C), which produces large particle and a broad size distribution.⁵⁵ Moreover, stabilizing agents that protect colloidal metal particles from aggregation often prevents also the self-assembly of polymeric precursor and pore template.⁵⁵ Also the interaction between metal and carbon species during carbonization and pore formation remains so far largely unexplored. A direct synthesis of catalytically active noble-metal containing OMC films has therefore not been reported so far.

We report the first direct synthesis route to mechanically, chemically and thermally stable OMC films that incorporate exemplarily catalytically active palladium particles. The

general synthesis procedure is illustrated in Scheme 6. The synthesis is based on the redissolution of a pre-polymerized RF resin that already contains a structure-directing agent (Pluronic F127) in THF along with dissolved metal precursors. The use of metal salts that are soluble in THF is a key requirement of the synthesis. After film deposition of the combined solution via dip-coating, thermal cross-linking and carbonization an electrically conductive mesoporous carbon film is obtained that contains small and accessible metal particles.



Scheme 6. Illustration of the synthesis approach to mesoporous Pd/OMC catalyst films. The structure-directing triblock copolymer F127 (PEO-PPO-PEO) and resorcinol are dissolved in ethanol. After addition of hydrochloric acid, formaldehyde solution is added to start a polycondensation reaction. The derived polymeric resin is separated by centrifuging and washed. The polymeric compound is redissolved in a Pd(acac)₂ containing THF solution. Under controlled conditions a film is deposited via dip-coating to obtain a homogeneous mesophase film. After thermal treatment at 100 °C in air and a subsequent carbonization under inert atmosphere (N₂) at 600 °C a mesoporous Pd/OMC film is obtained.

The following sections present the synthesis details, the obtained morphology, crystallinity and porosity of carbonized Pd/OMC film as well as its catalytic activity studied exemplarily in heterogeneous catalysis (butadiene hydrogenation and electrocatalysis (hydrogen evolution reaction HER)). The comparison to conventional catalysts reported in literature illustrates the superior performance of the binder-free Pd/OMC in both types of applications.

3.2 Experimental section

Chemicals

Resorcinol, formaldehyde (37 wt% in water) and Pluronic F127 (PEO₁₀₆-b-PPO₇₀-b-PEO₁₀₆, M_w = 12 600) were purchased from Sigma-Aldrich. MilliQ water was used for all synthesis procedures. Ethanol (EtOH, >99.9%, absolute) and tetrahydrofuran (THF, >99.9%, absolute) were purchased from VWR. 3 M hydrochloric acid (HCl) was prepared

from 12 M HCl (Alfa Aesar). Palladium(II) acetylacetonate ($\text{Pd}(\text{C}_5\text{H}_7\text{O}_2)_2$ or $\text{Pd}(\text{acac})_2$, 98%) was purchased from Alfa Aesar. 5%-Nafion solution, isopropanol as well as Pd on activated carbon (Cat. No. 20.568-0, 5 wt%) were obtained from Sigma-Aldrich. All chemicals were used without further purification.

Substrate pre-treatment

Si wafer substrates were cleaned with ethanol and calcined in air (2 h, 600 °C) prior to film deposition. Stainless steel plates (1.4301) were cut into 33 x 27 mm substrates. The steel substrates were grinded, washed and calcined as described earlier.⁹⁷ Glassy carbon (Sigradur G) substrates were purchased from HTW. All glassy carbon (GC) substrates were polished with 0.05 μm diamond dispersion and cleaned thoroughly with ethanol and water. SiO_2 glass substrates for conductivity measurements were purchased from UniversityWafer and cleaned with ethanol.

Synthesis of Pd/OMC: Pd-containing mesoporous carbon films and powders

For the catalyst synthesis according to Scheme 6 an amount of 1.1 g of resorcinol was mixed with 0.3 g of F127 in 4.5 mL of EtOH until a clear solution was obtained. Then 4.5 mL of 3 M HCl were added. The mixture was stirred for five minutes. 1.3 g of formaldehyde (37% in water) was added and thoroughly mixed. After circa four minutes the solution became turbid. Ten minutes after the addition of the formaldehyde solution, a white precipitate was separated from the mixture by centrifugation at 7500 rpm for 5 min and the top-layer solution was discarded. The white precipitate was washed with water and then dissolved in 5 mL of THF containing 31.5 mg of dissolved $\text{Pd}(\text{acac})_2$. A clear orange dispersion was obtained and used for dip-coating. Films were deposited via dip-coating at 25 °C and 30% relative humidity. The coated substrates were thermally treated at 100 °C for 12 h in air, followed by carbonization at 600 °C for 3 h in flowing nitrogen atmosphere (heating ramp of 1 K/min). Corresponding powder samples were prepared by drying the dip-coating suspension in a crucible followed by an identical thermal treatment as applied to the films. For enhanced catalytic performance, films were additionally treated in a muffle furnace at 400 °C for five minutes in air to remove residual carbon from the formed Pd particles. In case of electrocatalytic testing in the hydrogen evolution reaction the catalyst was in addition treated for 15 min at 400 °C in a tube furnace in an atmosphere of 5% hydrogen in argon.

Synthesis of Pd/C/Nafion reference catalyst

The reference catalyst was prepared by dissolving 5 mg of Pd/active carbon (5 wt%) in 3.98 ml of water. 20 μl of Nafion solution (5%) was carefully added. After addition of 1 ml of isopropanol the mixture was sonicated for 15 min with 6 W output power with a Branson

Sonifier. The resulting ink was immediately employed for film deposition via drop-casting and subsequent drying at 60 °C. The resulting reference catalyst film had a geometric Pd loading of 1.15 $\mu\text{g}/\text{cm}^2$. In the following the catalyst will be denoted as Pd/C/Nafion.

Physico-chemical properties

SEM images were collected on a JEOL 7401F at 10 kV. Image J program, version 1.39u (<http://rsbweb.nih.gov/ij>), was employed to determine the pore diameter, film thickness, size of Pd particles and to obtain fast Fourier transformed (FFT) images. TEM and selected area electron diffraction (SAED) images were recorded on a FEI Tecnai G² 20 S-TWIN operated at 200 kV on fragments of film samples scraped off the substrates and deposited on carbon-coated copper grids. To determine the amount of the Pd in the film, the mass depth was calculated using the STRATAGEM film analysis software (v 4.8) based on wavelength dispersive X-ray (WDX) spectra analyzed with a JEOL JXA-8530F electron microprobe at 7 and at 10 kV.

Films coated on thin silicon wafers (50 μm) were used for 2D-SAXS measurements. 2D-SAXS patterns were collected at the μSpot beamline at BESSY II synchrotron (Berlin, Germany) with a calibrated radiation energy of 12.399 keV. The SAXS data were processed employing the software FIT2D Version V12.077. XRD was measured on a Bruker D8 Advance (Cu K α radiation) with grazing incident beam (1°).

XP spectra were recorded with an Omicron DAR 400 X-ray source with Al-K α excitation. Electrons were detected with an EA 125X Hemispherical Energy Analyzer

Two-point sheet conductivity measurements were performed with a Keithley Model 6517B Electrometer employing a 8x8 pin probe head with an altering polarity sequence of the pins. Kr and N₂ adsorption isotherms were measured at 77K with a Quantachrome Autosorb-iQ. The samples were degassed in vacuum at 150 °C for 2 h prior to sorption analysis. The surface areas were determined by the Brunauer-Emmett-Teller (BET) method. Pore size evaluation was done with a QSDFT equilibrium Kernel and a model assuming cylindrical pores.

Adhesion of a carbonized Pd/OMC coating to a steel substrate was tested by the “tape test” as describe in ASTM D3359 *Standard Test Methods for Measuring Adhesion by Tape Test* (<http://www.astm.org/Standards/D3359.htm>). An X-cut was made through the coating penetrating the substrate. An adhesive tape (Scotch-Tape) was applied over the cut. The tape was smoothed and then pulled away. Poorly adhered coatings would peel away with the tape whereas well-adhered coatings would be stable. Photographs before and after the test were taken, employing an Olympus BX40 optical microscope.

Catalytic testing in hydrogenation of 1,3-butadiene

Pd/OMC films were coated on both sides of steel substrates. For each catalytic run, 5 or 10 identical steel plates with the same thickness (0.5 mm for 5 plates, and 0.25 mm for 10 plates) were stacked parallel into the reactor housing. Photographs of a catalyst stack and the reactor are presented in Supplement Figure S2. The testing setup and the procedure was similar to the one described by Ortel et al.⁹⁷ A reaction mixture consisting of 5% butadiene (2.5 purity), 10% hydrogen (5.0 purity), and 85% nitrogen (5.0 purity) was passed through the reactor at a flow rate of 60 mL/min (STP) at 1.05 bar. The catalyst was heated to 80 °C under reactive gas flow and equilibrated to reaction conditions for several hours. Afterwards, the temperature was gradually decreased stepwise from 80 °C, 72 °C, 64 °C, 56 °C, 48 °C, 40 °C and finally to 35 °C with a dwell time of 60 min for each temperature set point. Analysis of the gas products was continuously performed every 7 min by an online gas chromatograph (Agilent GC 7890 equipped with FID, TCD and columns HP Plot Al₂O₃, Molsieve 5A, HP Plot Q and DB FFAP). The space-time yield (STY) was calculated as produced moles of butenes per second per kilogram of the catalyst [$\text{mol}_{\text{butene}} \text{ s}^{-1} \text{ kg}_{\text{catalyst}}^{-1}$] and kilogram contained [$\text{mol}_{\text{butene}} \text{ s}^{-1} \text{ kg}_{\text{Pd}}^{-1}$].

Electrocatalytic testing in hydrogen evolution reaction in acidic medium

All electrocatalytic testing was performed by using a three-electrode disc setup with a RHE (Gaskatel, HydroFlex) as a reference and Pt gauze (ChemPur, 1024 mesh cm⁻², 0.06 mm wire diameter, 99.9%) as a counter electrode. All potentials in this work are referenced to the reversible hydrogen electrode. Small discs with a diameter of 6 mm were cut out from the coated GC substrates. These homogeneously coated discs were mounted on a rotating disk shaft and served as a working electrode ($n = 2000$ rpm) using 0.5 M H₂SO₄ as the supporting electrolyte (Fixanal, Fluka Analytical) and a BioLogic SP-200 as the potentiostat. The electrolyte solution was purged for at least 30 minutes with nitrogen before the catalytic tests. Prior to testing a break-in procedure was conducted (50 potential cycles in the cathodic regime (50 to -210 mV)) followed by a conditioning time of 2 h at open circuit potential. During break-in treatment and in the subsequent HER measurement a flow of N₂ gas maintained over the electrolyte. The activity in the hydrogen evolution reaction was investigated by cyclic voltammetry in a potential window of 50 to -210 mV vs. RHE with a scan rate of 20 mV s⁻¹. After 50 cycles no potential was applied for two hours, followed by another sequence of 50 cycles in the HER regime. Impedance spectroscopy was measured to correct the ohmic losses.

3.3 Results and Discussion

Physico-chemical properties of Pd/OMC films

Figure 6 presents for a typical Pd/OMC catalyst film carbonized for 3 h at 600 °C in nitrogen flow: a) SEM cross-section images in secondary electron mode and b) back-scattered electron mode, 2D-SAXS patterns recorded with c) an incident angle of $\beta = 90^\circ$ and d) $\beta = 7^\circ$, e) a TEM micrograph of a film segment and f) diffraction patterns obtained by XRD. The film contains 3 wt% Pd (from WDX analysis and StrataGem evaluation).²²

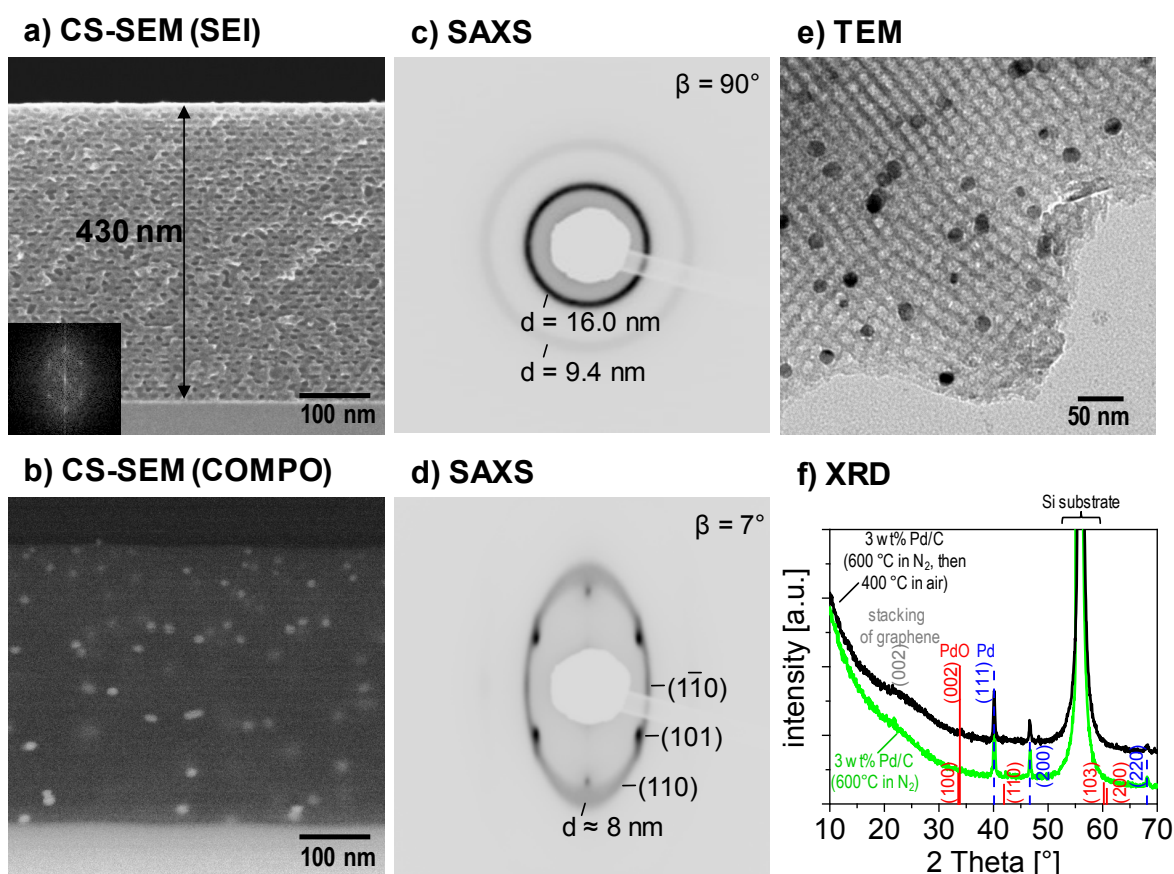


Figure 6. Physico-chemical analysis of a F127-templated ordered mesoporous carbon film, containing 3 wt% Pd, carbonised at 600 °C. Cross-section SEM image in secondary electron mode with FFT inset (a) and in back-scattered electron mode (b). 2D-SAXS patterns with an incident angle of $\beta = 90^\circ$ (c) and $\beta = 7^\circ$ (d). The anisotropic ring in (c) can be attributed to regular pore lattice distances of 16.0 nm in first order and 9.4 nm in second order. The scattering spots in (d) are indexed according to a face-centered cubic pore lattice (space group $Im\bar{3}m$) with (110) orientation in respect to the substrate surface. A TEM micrograph of a scraped off film segment (e) shows homogeneously distributed PdNP (dark spots) in an ordered mesoporous carbon matrix. XRD analysis (f) of a film carbonized at 600 °C is compared to a film additionally treated at 400 °C in air. Assigned (*hkl*) indices correspond to cubic Pd metal (PDF 46-1043), cubic PdO (PDF 41-1107). A broad reflection (24°) can be attributed to stacking of graphene.⁷⁶

The SEM cross-section image (Figure 6a) recorded in secondary electron image mode indicates that the Pd/OMC films exhibit a homogeneous and locally ordered pore structure throughout the film without cracks, aggregates or other irregularities. The film thickness amounts to ca. 430 nm. The templated mesopores feature dimensions of 8 nm

parallel and 6 nm perpendicular to the substrate. The FFT obtained from the SEM image (inset in Figure 6a) features an ellipsoidal pattern with bright spots that can be attributed to periodic pore distances of 14 nm parallel and 9 nm perpendicular to the substrate. The diffraction spots can be assigned to the (110) and the (101) planes of a cubic closed packing of pores and therefore indicate a high degree of ordering. The ellipsoidal pore shape originates from a uniaxial film contraction during template removal which is in line with the ellipsoidal nature of the pores.⁹⁷

SEM images recorded with backscattered electrons on same film position (Figure 6b) indicate the location of Pd containing particles as bright spots caused by higher metals higher z contrast. The formed Pd particles appear to be separate and distributed throughout the whole volume of the mesoporous carbon film.

N₂ sorption analysis of a corresponding Pd/OMC powder sample confirms a narrow size distribution of the formed mesopores around 5 nm (see QS-DFT evaluation of a full N₂ isotherm, Supplement Figure S3). This observation is consistent with the pore sizes observed from SEM images. The deduced total pore volume amounts to 0.46 cm³/g. 40% of this pore volume can be assigned to micropores. The accessible surface area of a Pd/OMC film carbonized at 600 °C was obtained via BET analysis of a Kr physisorption measurement and amounts to 590 m² per cm³ film volume.

Small angle X-ray scattering (SAXS) patterns of Pd/OMC films carbonized at 600 °C show a high degree of pore ordering (Figure 6c, d). The pattern recorded at 90° beam incident angle with respect to the film surface plane shows two isotropic rings that can be attributed to *d*-spacing values of 16.0 nm and 9.4 nm of the mesopore lattice (Figure 6c). SAXS measured in grazing incidence (Figure 6d) shows an ellipsoidal shape that indicates uniaxial film shrinkage perpendicular to the substrate. The bright scattering spots can be assigned to the lattice planes (1 $\bar{1}$ 0) as well as (101) of a contracted cubic pore system.⁹⁹ The *d*-spacing value perpendicular to the substrate amounts to 8 nm, which indicates a film contraction of ca. 50% during template removal and carbonization. The porous system is only weakly influenced by the embedded nanoparticles. Yet, higher metal contents (> 3 wt%) will reduce the pore ordering.

A TEM micrograph of a Pd/OMC film segment (Figure 6e) confirms the homogeneous distribution of Pd particles and a particle size of about 14.3 ± 3.2 nm with particles being located inside a well ordered mesoporous carbon framework. The majority of the particles located inside the film remain small. XRD patterns (Figure 6f) were obtained for Pd/OMC films carbonized at 600 °C in nitrogen and for films treated additionally for 15 min at 400 °C in air in order to remove carbon species from the surface of Pd particles (see also Supplement Figure S4). Clear reflections can be observed at 40.1°, 46.7° and 68.1°, which corresponds well with the (111), (200) and (220) lattice planes of metallic palladium

(PDF 46-1043). SAED analysis (not shown) confirms that Pd is present in a metallic state. The XRD signal at 56° results from the substrate (Si wafer) employed for the Pd/OMC film samples studied in XRD. Reflections corresponding to palladium oxide were not observed. A broad reflection around 24° can be attributed to the (002) lattice plane of disordered small graphene stacks.⁷⁶ A XP spectrum in the region of Pd_{3d} (Supplement Figure S5a) is dominated by a signal that corresponds to metallic Pd (335.0 eV).⁶⁸ Smaller peaks of PdO and PdO₂ at 336.2 eV¹⁰⁰ and 337.6 eV⁶⁶, respectively, correspond to oxidized layers on the Pd surface which form when the film sample is exposed to ambient air. An intense peak in the C_{1s} region (Supplement Figure S5b) confirms the dominating presence of graphitic carbon.¹⁰¹

Partial graphitization is an essential requirement of the film synthesis in order to produce materials with an electrical conductivity high enough to allow electrocatalytic reactions to occur on the formed Pd particles. The electrical conductivity measured for Pd/OMC films carbonized at 600 °C amounts to 0.03 S/cm. Adhesion of a Pd/OMC film to a steel substrate was tested by the tape test.¹⁰² As depicted in Supplement Figure S1 no carbon film was peeled off after pulling off a tape. This behavior indicates good mechanical stability and strong adhesion of the carbon film to the substrate.

The developed synthesis approach thus produces conductive carbon films with well-ordered mesopores throughout the film volume with a high surface area. The formed metallic Pd nanoparticles are well dispersed and the presence of Pd does not disturb the formation of the open-porous carbon network. The carbon shows a small degree of graphitization and good electrical conductivity.

Catalytic performance in butadiene hydrogenation

The developed Pd/OMC catalytic coatings were tested in a micro-structured reactor designed to accommodate five and ten catalyst plates with minimal channel width (1625 and 830 μm , respectively). The reactor design (see Supplement Figure S2b) maximizes the contact area between catalytic coating and thermally conductive reactor material to ensure that very fast and exothermic reactions such as the hydrogenation of butadiene can be studied under isothermal conditions.

Figure 7 displays catalytic results obtained with a stack containing five reactor plates coated on both sides with Pd/OMC, carbonized at 600 $^{\circ}\text{C}$ in N_2 atmosphere and additionally treated for 5 min at 400 $^{\circ}\text{C}$ in air to remove carbon species. Shown are a) butadiene conversion vs. temperature with and without the initial air treatment, b) selectivity vs. conversion and c) a comparison of butadiene conversion between reactors comprising five and ten stacked catalyst plates.

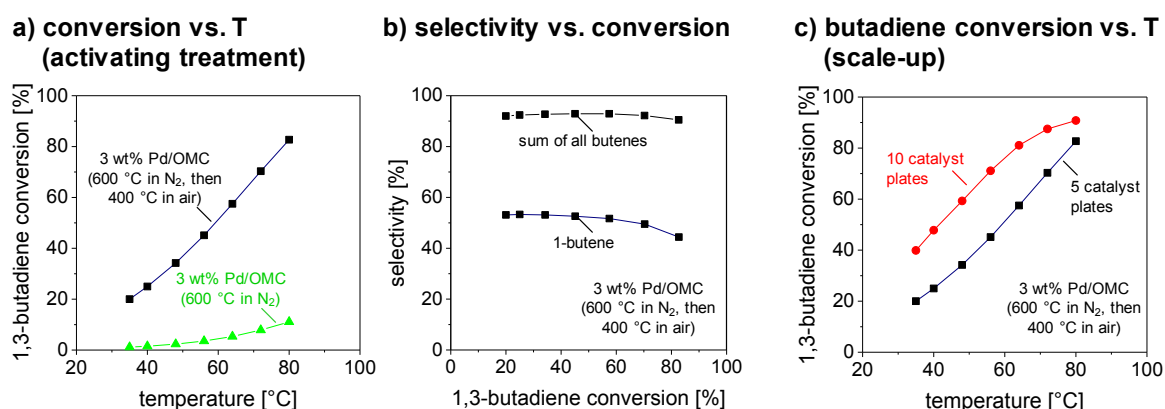


Figure 7. Catalytic performance of mesoporous Pd/OMC catalytic coatings in the selective gas-phase hydrogenation reaction of 1,3-butadiene. a) Butadiene conversion vs. temperature. The Pd/OMC catalyst with 3 wt% Pd loading treated for 5 min at 400 $^{\circ}\text{C}$ in air is compared to a non-treated Pd/OMC catalyst. b) Selectivity to 1-butene and total butene selectivity vs. butadiene conversion. c) Butadiene conversion vs. temperature of 5 coated catalyst plates compared to a scaled-up approach with 10 plates. Both catalyst sets were pretreated for 5 min at 400 $^{\circ}\text{C}$ in air. The reaction feed contained 5% butadiene and 10% hydrogen in nitrogen at a constant flow rate of 30 ml/min. The composition of the product gas flow was studied at seven different temperatures between 35 $^{\circ}\text{C}$ and 80 $^{\circ}\text{C}$.

Figure 7a indicates a poor activity for the film treated only in N_2 , with a butadiene conversion reaching less than 11% at 80 $^{\circ}\text{C}$. After additionally treatment of a corresponding Pd/OMC film in air (5 min, 400 $^{\circ}\text{C}$) a drastically higher activity can be observed that reaches 20% already at 35 $^{\circ}\text{C}$ and 83% at 80 $^{\circ}\text{C}$. The strongly enhanced performance suggests that the Pd particles contained in the "as carbonized" Pd/OMC film might be covered by a thin carbon shell, which can be removed by the air treatment and results in a highly active hydrogenation catalyst (see Supplement Figure S4 for more information).

Figure 7b plots for the air-treated Pd/OMC catalyst the selectivity towards 1-butene and towards the sum of all butenes vs. the butadiene conversion. The catalyst performs very selective. At low conversion selectivities amount to about 54% (1-butene) and 92% (sum of all butenes). The observed 1-butene selectivity agrees well with typical Pd/C and Pd/TiO₂ catalysts reported in literature.^{19, 22, 97, 100} More remarkably, the high selectivity to 1-butene is retained also well above 80% butadiene conversion, whereas typical catalysts reported in literature show a significant decrease in selectivity starting already at butadiene conversion levels of about 50% (Pd/TiO₂, in⁹⁰) to 60% (Pd/C, in¹⁹, Pd/TiO₂ in^{97, 100}).

The space-time yield of butene formed per mass of Pd contained in the catalyst can be used to compare the performance of different reported Pd/C catalysts directly. Yan et al.¹⁹ reported performance data obtained under condition comparable to our study (48 °C, C_{H₂}:C_{BD} = 2.5:1, 110 µg active Pd, 1.01 bar). The reported catalysts include a commercial Pd/C, Pd nanoparticles supported on graphene as well as single-site Pd catalysts supported on graphene. The obtained STY for those catalysts amounts to 2.5, 2.5 and 3.0 mol_{butene} s⁻¹ kg_{Pd}⁻¹, respectively. In contrast, the Pd/OMC catalyst presented in Figure 7a produces 3.8 mol_{butene} s⁻¹ kg_{Pd}⁻¹ which indicates a 25 to 50% higher mass-specific catalytic activity towards butene formation.

Different factors might be contributing to the observed high activity. Silvestre et al. and Dal Santo et al. reported that butadiene hydrogenation is a highly structure sensitive reaction.^{69, 87} Pd-(111) facets were concluded to dominate hydrogenation rates for supported Pd particles that exceed a particle size of 4 nm.⁶⁹ Moreover, Schauermann, Freund and co-workers reported in a series of publications, that the presence of subsurface carbon atoms on Pd surfaces drastically lowers the activation barrier for subsurface migration of H-atoms on Pd-(111) facets, which critically influenced the corresponding activity and selectivity of olefin conversions in their studies.^{12, 99, 103} During the high-temperature treatment of our Pd/OMC catalysts, carbon species were abundantly present which makes the migration of carbon in to the subsurface region of Pd particles likely and could explain the high hydrogenation reactivity. However, such subsurface carbon species are very difficult to analyze and thus beyond the scope of this work.

Further insights can be gained from the Arrhenius plots. The activation energy derived for Pd/OMC between 35 and 56 °C amounts to 31.5 kJ/mol. This value is about 50% lower than activation energies reported for oxide-supported Pd catalysts (Pd/TiO₂: 68 kJ/mol¹⁰⁴ and 62 kJ/mol^{97, 100}; Pd/Al₂O₃ 48-66 kJ/mol⁹¹) as well as carbon-supported Pd (Pd/C: 58 kJ/mol; PdNP/graphene: 65 kJ/mol, both calculated from data reported in¹⁹). An apparent energy of activation which amounts to about half the value of the true activation energy is a typical indicator of transport limitations by pore diffusion.¹⁶ Physisorption

measurements on the Pd/OMC catalysts indicate that about 40% of their total pore volume can be assigned to micropores (see Supplement Figure S3). The observed apparent energy of activation of 31.5 kJ/mol could thus indicate that a major fraction of the active Pd could be located inside micropores. However, Pd/OMC still outperforms all comparable carbon supported Pd catalysts reported in literature in terms of butene formation rates.

One specific advantage of the developed synthesis route is the simple and facile scale-up of the catalyst and reactor production via "numbering up" of the number of catalyst plates fitted into the reactor housing. A photo of a micro-structured reactor fitted with five and ten catalyst plates is shown in the Supplement Figure S2. The corresponding performance of both catalyst stacks is compared in Figure 7c in terms of butadiene conversion plotted vs. temperature. At 35 °C the conversion amounts to 20% (five plates) and 40% (10 plates), i.e. twice as high. Moreover, the observed space time yield amounts to $2.2 \text{ mol}_{\text{butene}} \text{ s}^{-1} \text{ kg}_{\text{Pd}}^{-1}$ for both configurations, illustrating perfect scale-up behavior. The data illustrates the simplicity of the scale-up of catalyst and reactor and confirms that excellent temperature control and close to isothermal conditions can be retained despite the doubled amount of heat produced by the fast and highly exothermic reaction.

Electrocatalytic performance in the hydrogen evolution reaction

The HER performance of Pd/OMC catalyst films deposited on a glassy carbon was tested by cyclic voltammetry (CV) performed in acidic medium (0.5 M H₂SO₄). The catalyst films were carbonized at 600 °C and then treated for 5 min at 400 °C in air (oxidative cleaning) and 15 min in H₂/Ar atmosphere at 400 °C (reduction). Figure 8 plots a) the current density recorded at -200 mV during the first 50 cycles, (b) the 50th recorded CVs as current density vs. applied potential and c) the corresponding Tafel plots for the Pd/OMC catalyst as well as a conventional Pd/C/Nafion shown for reference. Both catalysts feature the same Pd loading (1.15 μg/cm²). Figure 8b) shows in addition also the activity of Pd-free OMC.

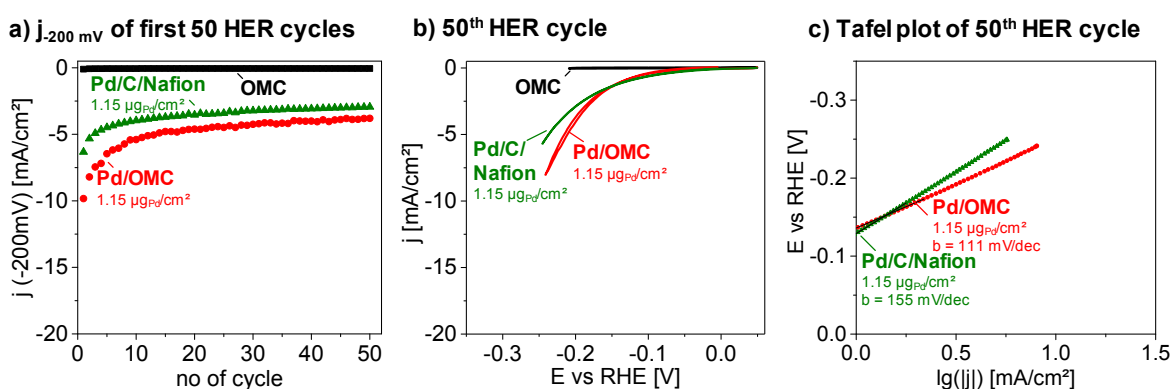


Figure 8. Electrocatalytic performance of Pd/OMC, Pd/C/Nafion and Pd-free OMC films in HER. a) Current response at a potential of -200 mV (vs. RHE) plotted vs. cycle number derived from the first 50 cathodic sweeps during CV testing. b) Geometric current density plotted vs. potential for the 50th cycle of CV testing. c) Tafel evaluation (potential vs. $\log(\text{current density})$) for the 50th cycle. The first 15 points in the HER regime were employed for linear fitting. All CVs are recorded in 0.5 M sulfuric acid with a scan rate of 20 mV/s. The graphs compare a mesoporous 3 wt% Pd/OMC catalyst with a Pd-free OMC coating (390 nm thick film) and a conventional Pd/C/Nafion reference catalyst film based on a Nafion ink and commercial Pd/C (5 wt% on activated carbon). Both Pd-containing catalysts feature the same geometric Pd loading of 1.15 μg_{Pd}/cm².

Pd/OMC shows throughout the first 50 cycles a significantly higher HER current than the Pd/C/Nafion reference coating (Figure 8a). Moreover, both catalysts show decreasing currents in the first 20 cycles followed by a regime of stable performance. The initial activity follows for both catalysts a similar pattern and is therefore not specific to Pd/OMC. The decrease could be related to an initial saturation of the electrolyte with the formed hydrogen gas that hinders subsequent hydrogen desorption.

The CVs depicted in Figure 8b for the 50th cycle indicate the HER activity as a function of potential. No oxidation or reduction features other than HER are observed. Both Pd/OMC and Pd/C/Nafion contain the same amount of Pd. The Nafion-free Pd/OMC catalysts shows higher HER currents particularly at the more negative applied potential, i.e. higher

current densities. Ordered mesoporous carbon films without palladium (Figure 8b "OMC") show no signs of HER activity nor any other reductive currents.

Tafel evaluation plots can provide insights into mechanistic aspects and transport limitations in the HER.¹³ Figure 8c displays Tafel plots for Pd/OMC and Pd/C/Nafion after 50 HER cycles. The observed Tafel slopes amount to 111 mV/dec for Pd/OMC and 155 mV/dec for Pd/C/Nafion. Pentland et al. derived Tafel slope of about 99 to 107 mV/dec for unsupported polycrystalline Pd.¹⁰⁵ Bhowmik et al. reported similar values around 121 mV/dec for Pd/C/Nafion catalysts.¹⁰⁶ Bai et al. observed 85 mV/dec for preformed Pd cubes (d = 10 nm) fixed with Nafion on a working electrode.¹⁰⁷ Hence, Pd/OMC exhibits Tafel slope values that are well within the range of literature values reported for Pd. Values around 120 mV/dec were reported to be indicative for the discharge of a proton on the metal surface to be rate-determining (Volmer reaction, $H^+ + e^- + M \rightleftharpoons MH_{ads}$).¹³

Table 1. Comparison of the HER performance in acidic solution of the herein presented catalysts Pd/OMC and Pd/C/Nafion with state-of-the-art catalysts reported literature.

Author	Catalyst	Pd loading [$\mu\text{g}/\text{cm}^2$]	Electrolyte	j at -200 mV [mA/cm ²]	$j_{\text{mass-based}}$ at -200 mV [mA/ μg_{Pd}]	Tafel slope b [mV/dec]
this study	Pd/OMC	1.15	0.5 M H ₂ SO ₄ (N ₂)	-3.7	-3.2	111
this study	Pd/C/Nafion	1.15	0.5 M H ₂ SO ₄ (N ₂)	-2.9	-2.5	155
Bhowmik et al. ¹⁰⁶	Pd/C/Nafion	43	0.5 M H ₂ SO ₄ (N ₂)	-16	-0.37	121
Bai et al. ¹⁰⁷	PdNP /Nafion	46	0.5 M H ₂ SO ₄ (Ar)	-11	-0.24	85
Bai et al. ¹⁰⁷	PdNP/rGO/Nafion	46	0.5 M H ₂ SO ₄ (Ar)	-50	-1.1	
Pentland et al. ¹⁰⁵	pc Pd ^a		0.01 M HCl			107

The intrinsic activity of different Pd-based catalysts can be compared based on the mass-normalized current density recorded at the same overpotential. Table 1 compares for different catalysts the current density measured at -200 mV vs. RHE, the corresponding Pd loading, the mass-normalized activity as well as the respective reported Tafel slopes. The new Pd/OMC catalysts achieve a mass-normalized HER current of -3.2 mA per μg Pd after 100 cycles, whereas the Pd/C/Nafion measured for comparison reaches only -2.5 mA/ μg_{Pd} . Carbon-supported catalysts reported in literature show in general lower activities. Bhowmik et al. report -0.37 mA/ μg_{Pd} for a Pd/C/Nafion catalyst.¹⁰⁶ Catalysts reported by Bai et al. perform with -0.24 mA/ μg_{Pd} (Pd nano-cubes / Nafion) and -1.15 mA/ μg_{Pd} (Pd nano-cubes / reduced Graphene Oxide rGO / Nafion).¹⁰⁷ Hence, the Nafion-free Pd/OMC catalysts outperform the Pd/carbon catalysts reported in literature by at least a factor of three.

3.4 Conclusion

Highly active binder-free carbon based supported catalysts can be synthesized in the form of wall-coatings by a synthesis route that employs the co-deposition of a structure-directing agent and small clusters of polymeric carbon precursors along with ionic metal species on a substrate. A sequence of thermal treatments converts the polymer into partly graphitized carbon, decomposes the structure-directing agent and converts the metal precursor into highly active nanoparticles. The resulting Pd/OMC films contain small Pd particles well-distributed in a mesoporous carbon matrix and with high surface area, chemical, mechanical and thermal stability as well as electrical conductivity. The presented concept omits the necessity of a binder (e.g. Nafion) in the synthesis of the catalytic coating.

The binder-free Pd/OMC films prove to be highly active in the gas-phase hydrogenation of butadiene as well as the electrocatalytic hydrogen evolution reaction. In butadiene hydrogenation the obtained Pd/OMC coatings provide significantly higher space-time-yields than all reported Pd/C catalysts while at the same time enabling isothermal reactor conditions. The presented concept provides an easy path for the scale-up of synthesis and reaction while preserving ideal operating conditions. Moreover, when tested in the electrocatalytic hydrogen evolution reaction HER, the catalysts outperform reported Pd/C catalysts by a factor of three, which underlines the benefits of the developed binder-free catalyst system.

The presented concept paves the way to the controlled synthesis of a wide range of highly active catalytic coatings that employ carbon as a support for other active metals such as Pt, Ru and Rh and the opportunity to study these catalysts under very defined reaction conditions. Moreover, the catalyst properties can be easily tuned and enable the investigation of parameters such as pore size, film thickness and conductivity, and in particular of the role of Nafion in electrocatalysis.

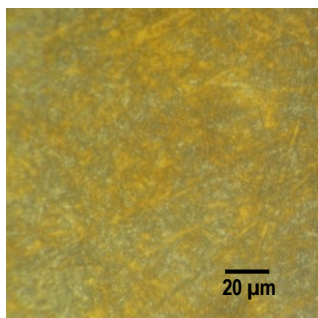
3.5 Acknowledgement

The authors thank Björn Eckhardt, Katrin Schulz, Roman Schmack, Arno Bergmann from TU Berlin, Eik Koslowski from Universität Halle as well as Sören Selve and Jörg Nissen from ZELMI (TU Berlin) for support in material analytics. We acknowledge funding from BMBF (FKZ 03EK3009). RK thanks in particular Einstein Foundation Berlin for generous support provided by an Einstein-Junior-Fellowship (EJF-2011-95). SAXS measurements were conducted at the μ Spot beamline at BESSY II synchrotron.

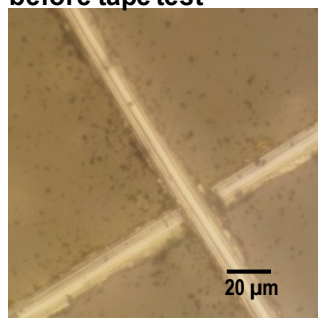
3.6 Supporting Information

1) Adhesion testing of Pd/OMC on steel substrates

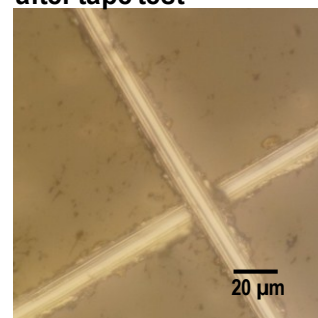
a) uncoated steel substrate



b) Pd/OMC coating on steel before tape test



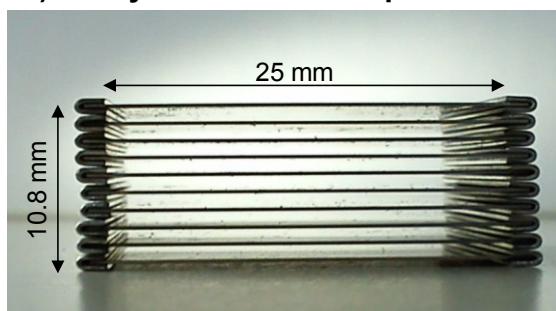
c) Pd/OMC coating on steel after tape test



Supplement Figure S1. Photographs, employing an optical microscope, of (a) an uncoated steel substrate, a (b, c) a Pd/OMC coating on a steel substrate (b) before and (c) after the tape test. The tape test is used to analyze the adhesion of a coating to the substrate. An X-cut was made through the coating (Pd/OMC carbonized at 600 °C) penetrating through to the substrate. Then Scotch-Tape was applied over the cut. The tape was smoothed and then pulled away. No coating was peeled off by this procedure.

2) Reactor design, catalyst geometry and scale up in heterogeneous catalysis

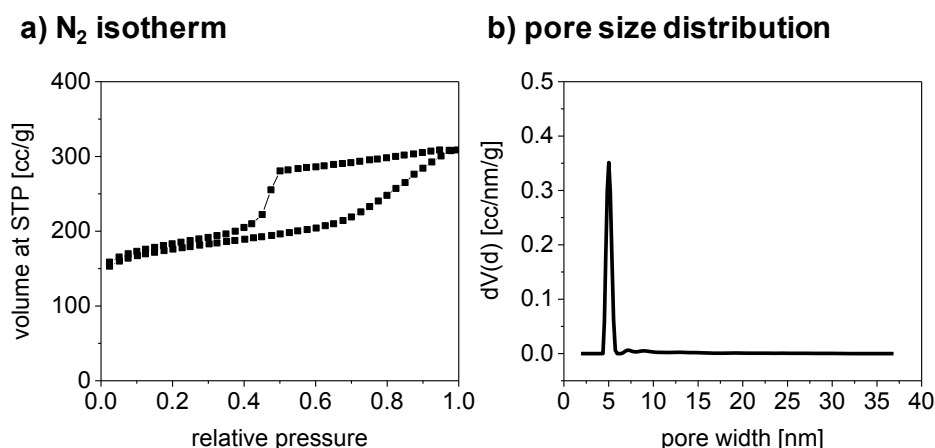
a) catalyst stack with ten plates



b) catalyst stack in reactor

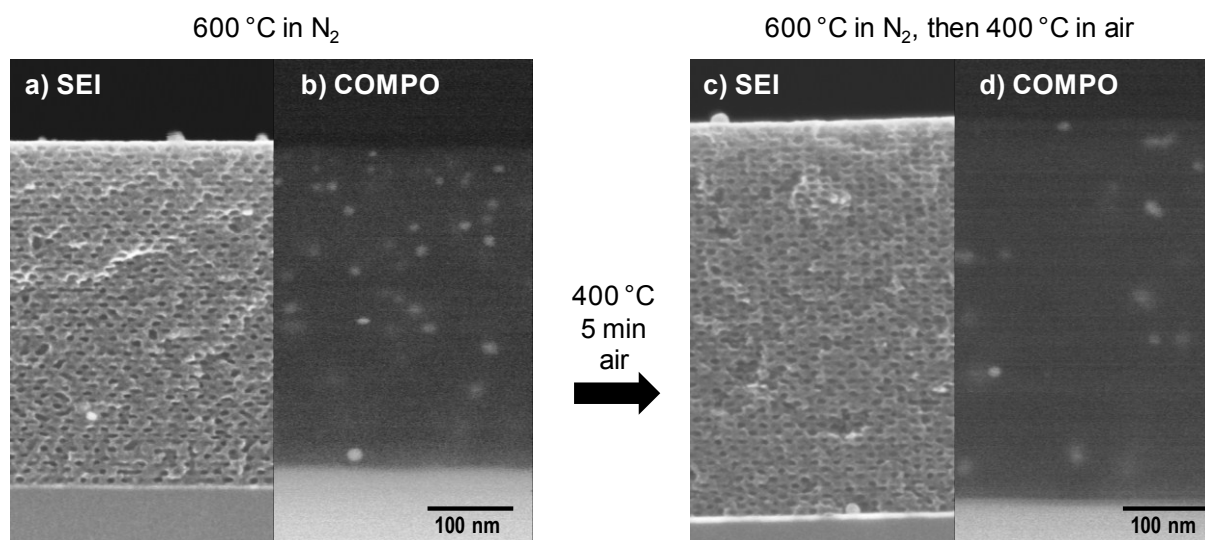


Supplement Figure S2. a) Photograph of a catalyst stack with ten stainless steel plates (plate dimensions: 30 mm x 25 mm x 0.25 mm). b) Photograph of the open reactor mounted with a catalyst stack of 5 plates coated with Pd/OMC. The reactor design ensures that the highly exothermic and very fast hydrogenation of butadiene can be studied under isothermal conditions. The change of temperature along the catalyst plates during the reaction was measured to be less than 1 K. Hence, despite the large amount of heat generated during butadiene hydrogenation the reactor can be operated isothermally and thus be used for kinetic studies.

3) N₂ sorption analysis of Pd/OMC

Supplement Figure S3. N₂ physisorption analysis of a F127-templated carbon powder containing 1.2 wt% Pd, carbonized at 600 °C. a) Nitrogen adsorption/desorption isotherm. b) Pore size distribution curve employing a QSDFT equilibrium model (cylindrical pores).

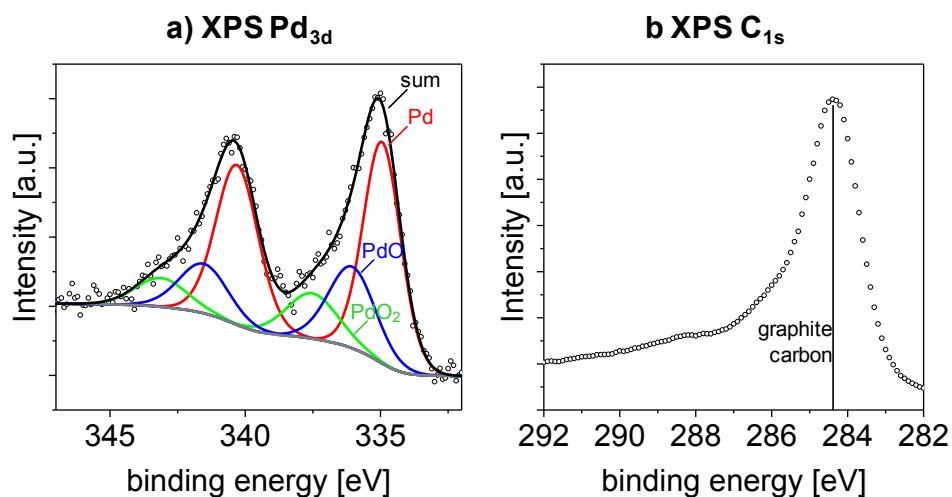
4) SEM analysis of Pd/OMC prior and after air treatment at 400 °C



Supplement Figure S4. SEM analysis of a F127-templated ordered mesoporous carbon film, containing 3 wt% Pd, carbonised at 600 °C without (a) and with (b) additional thermal treatment at 400 °C in air. Cross-section SEM image in secondary electron mode (a) and in back-scattered electron mode (b).

An additional thermal treatment at 400 °C for 5 min in air was applied to remove remaining carbon species from the surface of the Pd nanoparticles. SEM analysis of air-treated film with cross-section images in secondary electron mode (Supplement Figure S4a and c) and backscattered electron mode (Supplement Figure S4b and d) indicate that neither the film morphology nor the composition of the film are degraded by the air treatment.

5) XPS analysis of Pd/OMC



Supplement Figure S5. XP spectrum in the regions of Pd_{3d} and C_{1s} of a F127-templated Pd/OMC film carbonized at 600 °C in N₂ atmosphere, additionally treated in air at 400 °C and subsequently reduced in H₂/Ar at 350 °C. a) Pd_{3d} XP spectrum with deconvoluted peaks of Pd, PdO and PdO₂. b) C_{1s} XP spectrum with indicated binding energy of graphite carbon.

4 Pt-containing mesoporous carbon films

Published in

D. Bernsmeier, M. Bernicke, E. Ortel, A. Bergmann, A. Lippitz, J. Nissen, R. Schmack, P. Strasser, J. Polte, R. Kraehnert, *ChemElectroChem* **2017**, 4, 221.

DOI: [10.1002/celec.201600444](https://doi.org/10.1002/celec.201600444)

Reprinted with granted permission from John Wiley & Sons.

License date 12th of January 2017

Received: 25th of July 2016

Published online: 15th of November 2016

Published in print: 16th of January 2017

This dissertation was handed in on the 11th of October 2016. The herein presented version of the said research article contains small modifications as it represents its state before peer-revision.

Nafion-free carbon supported electrocatalysts with superior HER performance via soft-templating

Denis Bernsmeier¹, Michael Bernicke¹, Erik Ortel², Arno Bergmann¹, Andreas Lippitz²,
Jörg Nissen³, Roman Schmack¹, Peter Strasser¹, Jörg Polte⁴, Ralph Kraehnert¹

¹ Department of Chemistry, Technische Universität Berlin, Straße des 17. Juni 124, 10623 Berlin

² BAM - Federal Institute for Materials Research and Testing, Division 6.1, Unter den Eichen 44-46,
12203 Berlin

³ ZELMI, Technische Universität Berlin, Straße des 17. Juni 135, 10623 Berlin

⁴ Department of Chemistry, Humboldt-Universität zu Berlin, Brook-Taylor-Str. 2, 12489 Berlin

Abstract

Efficient water electrolysis requires electrode coatings with high catalytic activity. Platinum efficiently catalyzes the hydrogen evolution reaction (HER) in acidic environments, but is also a rare and expensive metal. The activity achieved per metal atom can be increased when small Pt particles are dispersed onto electrically conductive, highly accessible and stable support materials. However, the addition of Nafion, a typical binder material employed in the manufacturing of electrode coatings, can decrease catalytic activity via blocking of pores and active surface sites.

We report a new approach for the direct synthesis of highly active Nafion-free Pt/C catalyst films consisting of small Pt nanoparticles supported in size-controlled mesopores of a conductive carbon film. The synthesis relies on the co-deposition of suitable Pt and C precursors in the presence of polymer micelles, which act as pore templates. Subsequent carbonization in inert atmosphere produces porous catalyst films with controlled film thickness, pore size and particle size. The catalysts clearly outperform all Nafion-based Pt/C catalysts reported in literature in particular at high current densities.

Keywords: ordered mesoporous carbon, soft-templating, highly active electrocatalyst, carbon coating, film catalyst, platinum nanoparticles, hydrogen evolution reaction, Nafion-free

4.1 Introduction

Many catalytic applications rely on active metal species supported in a carbon matrix that provides a high surface area. Pt nanoparticles immobilized on conductive carbon allotropes such as graphitic carbon²⁴ or nanotubes²⁵ serve e.g. as highly active electrocatalysts for oxygen reduction^{24, 25} and hydrogen evolution reaction^{18, 108}. Pt/C is also commonly employed in heterogeneous catalysis for oxidation¹⁰⁹ and hydrogenation reactions²⁸, as amperometric biosensors²⁶ or in hydrogen storage²⁷.

Typical Pt/C catalysts have been synthesized via impregnation of a carbon support with a solution containing a dissolved Pt species, followed by a thermal treatment that converts the precursor into metallic Pt particles.²⁴⁻²⁸ Alternatively, also preformed colloidal Pt particles were immobilized on carbon support.^{29, 30} Such carbon supports are typically supplied as powders (carbon nanotubes^{25, 26, 28, 30}, activated carbon²⁷, carbon black²⁹).

Electrocatalysis in fuel cells and water electrolyzers³¹ as well as heterogeneous catalysis in micro-reactors^{100, 104} requires homogeneous and stable catalytic coatings. For the preparation of conventional electrode coatings fine-grained Pt/C powders are typically mixed with a binding agent (Nafion) and a solvent to produce an ink. This ink is applied onto electrode substrates and then dried. However, Nafion has been reported to block pores and active sites, which results in lower catalytic activity.³²⁻³⁴ Moreover, ink composition and distribution strongly influences the local electronic conductivity. The reproducible preparation of Nafion-based catalytic coatings has thus been described as "an art in itself".^{35, 36}

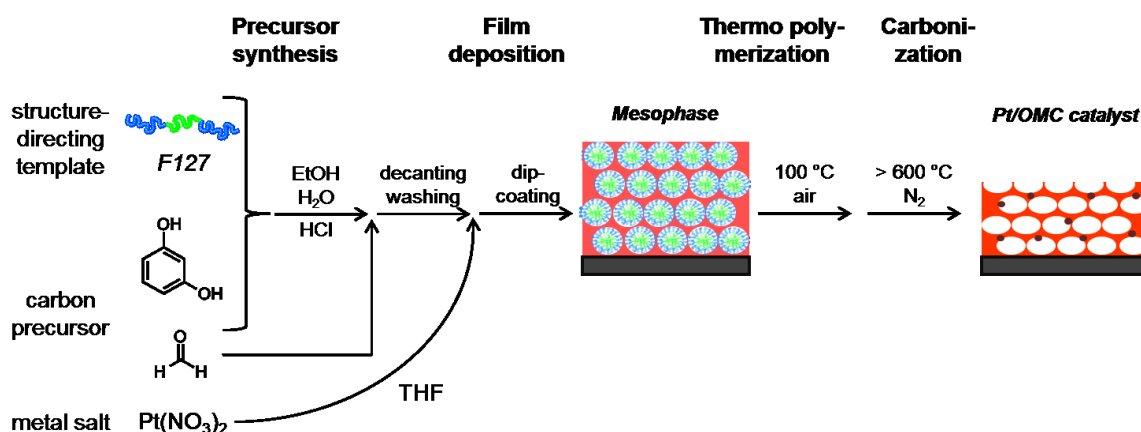
Introducing a high degree of size-controlled mesopores into the catalyst and omitting the need for the Nafion binder should considerably enhance the catalytic performance of Pt/C catalysts. A well-defined mesopore system can also enhance the thermal⁶⁹ and electrochemical stability⁷⁰ of supported Pt particles via pore confinement. An improved synthesis procedure for electrocatalytically active Pt/C coatings should thus (i) provide a high surface area and accessibility to the supported Pt particles via interconnected mesopores, (ii) enable excellent electronic conductivity, and (iii) omit the need for binding agents.

The synthesis of Pt-free carbon coatings with high surface, controlled porosity and pore connectivity^{40, 110, 111} as well as a high electrical conductivity¹¹² has been reported in the form of ordered mesoporous carbon "OMC" films. Control over the materials pore structure is obtained via amphiphilic molecules that act as structure-directing agents.^{42, 45, 110, 113} Typical syntheses start out from low molecular-weight precursor (e.g. resins consisting of a polycondensation product of phenol¹¹⁴, resorcinol⁴⁶ or phloroglucinol⁵² with formaldehyde) and a template molecule (e.g. triblock copolymer) dispersed in an organic solvent. Upon solvent removal precursor and structure-directing agent assemble into an ordered mesophase. Subsequent heat treatments remove the template polymer and convert the precursor into a carbon matrix.⁴⁵ Only few period 4 and 5 transition metals (Fe⁵⁵, Nb¹¹⁵) have been incorporated directly into OMC networks so far. However, such a direct synthesis of Me/OMC catalyst films did so far not succeed for any of the precious

metals that are active in fuel cell catalysis and electrolysis, which might be related to the fact that all of these metals are prone to strong sintering at the temperatures required for the framework graphitization.

We report the first Me/OMC synthesis that incorporates a precious metal (Pt) directly into an electrically conductive carbon film with templated porosity while retaining a small Pt particle size. The Nafion-free catalysts shows high conductivity and accessibility to Pt, resulting in superior electro catalytic performance when compared to all Pt-based HER catalyst reported in literature so far.

The Pt/OMC catalyst films were obtained by the procedure illustrated in Scheme 7. Polymer template (Pluronic F127) and a resin of resorcinol and formaldehyde were dispersed in a THF solution⁷¹ that contains suitable dissolved Pt species. Deposition of the solution via dip-coating results in a film featuring an ordered mesophase. Further thermo-polymerization at 100 °C and a subsequent heat treatment in inert atmosphere produces homogeneous carbon films comprising a system of ordered mesopores that contain small and well-dispersed Pt particles. The films are mechanically stable and adhere well to many different electrode substrates.



Scheme 7. Synthesis approach to mesoporous Me/OMC catalyst films illustrated for Pt. The structure-directing triblock copolymer F127 (PEO-PPO-PEO) and resorcinol are dissolved in ethanol. After addition of hydrochloric acid, formaldehyde solution is added to start a polycondensation reaction. The derived polymeric resin is separated by centrifuging and washed. The polymeric compound is redissolved in a Pt(NO₃)₂ containing THF solution. Under controlled conditions a film is deposited via dip-coating to obtain a homogeneous mesophase film. After thermal treatment at 100 °C in air and a subsequent carbonization under inert atmosphere (N₂) a mesoporous Pt/OMC film is obtained.

The following sections of the paper describe the synthesis details as well as structure and composition of typical Pt/OMC films, elucidate the impact of carbonization conditions on the films physico-chemical properties, assess the performance of different catalysts in the HER reaction and compare the best catalysts to numerous reference systems.

4.2 Experimental

Chemicals

MilliQ water was employed for all synthesis procedures. Resorcinol and formaldehyde (37 wt% in water), Pluronic F127 (PEO₁₀₆-*b*-PPO₇₀-*b*-PEO₁₀₆, M_w = 12 600 g/mol), 5%-Nafion solution and isopropanol were purchased from Sigma-Aldrich. Ethanol (EtOH, >99.9%, absolute) and tetrahydrofuran (THF, >99.9%, absolute) were obtained from VWR. 3 M hydrochloric acid (HCl) was prepared from 12 M HCl (Alfa Aesar). Platinum(II) nitrate (Pt(NO₃)₂ 99.95%) was purchased from ChemPur. All chemicals were used without further purification.

Pt on Vulcan (BASF, XC 72R (Cat. No. 181, 10 wt% Pt) and a thick polycrystalline Platinum foil (99.95%, 0.5 mm thick, from Labor-Platina) were employed as reference catalysts. The Pt foil was polished with a 0.05 μm Al₂O₃ dispersion and cleaned with water prior to testing.

Substrate pre-treatment

Catalyst films were synthesized on different substrates, i.e. single and double side polished Si wafers ((100)-orientation, from University Wafers), glassy carbon (Sigradur G from HTW), and SiO₂ glass microscope (Science Services). Si wafer substrates were cleaned with a tissue containing ethanol and calcined in air (2 h, 600 °C) prior to film deposition. The glassy carbon (GC) substrates were polished with 0.05 μm diamond dispersion and sonicated two times in water and ethanol, then rinsed with ethanol. SiO₂ glass substrates for conductivity measurements were sonicated in ethanol and then wiped with a tissue containing ethanol.

Synthesis of Pt/OMC films and powders

Pt/OMC catalyst films were synthesized via dip-coating of different substrates into solutions containing precursors for Pt and carbon as well as the structure-directing agents. The initial solution was obtained by mixing 550 mg of resorcinol together with 150 mg of the template Pluronic F127 and 2.25 mL of EtOH in a centrifuge tube until a clear solution was obtained. Then 2.25 mL of 3 M HCl were added to initiate a polymerization and the tube was placed for 5 min in a shaker. Thereafter 605 μl of formaldehyde (37% in water) were added at once and shaking was continued. The solution became turbid after another ca. four minutes. About 10 min after addition of the formaldehyde the formed white precipitate was separated via centrifugation (5 min at 7500 rpm). The white precipitate was then washed with water and thereafter dissolved in 2.5 mL of THF containing either 1.4, 4.5 or 7.7 mg of dissolved Pt(NO₃)₂. The obtained clear orange solution was used for film deposition.

Catalyst films were deposited onto the cleaned substrates via dip-coating at 25 °C and 30% relative humidity (dip-coater 5 AC from IDlabs). The coated substrates were transferred to a drying furnace and then thermally treated for 12 h at 100 °C in static air for film stabilization. The coated substrates were subsequently placed in a tube furnace and heated in N₂ flow with 1K/min up to typically 800 °C, holding the temperature for 3 h,

followed by subsequent naturally cooling down to room temperature. Corresponding powder samples were prepared by drying the dip-coating solution in a crucible, followed by the same thermal treatment as for the films. Prior to catalytic testing all catalyst film were treated in air at 400 °C (20 min, muffle furnace) in order to remove residual carbon species from the formed Pt particles.

Synthesis of catalytic reference coatings from Pt/Vulcan and Nafion

Coatings of Pt/Vulcan reference catalysts (1 $\mu\text{g}/\text{cm}^2$ geometric Pt loading) were prepared according to established routes reported in literature^{116, 117}. In a typical synthesis 5 mg of Pt/Vulcan powder (10 wt% Pt) were dispersed in 3.98 ml of water, to which 20 μl of Nafion solution (5%) and 1 ml of isopropanol were added. The mixture was sonicated for 15 min (Branson Sonifier, 6 W output power). The resulting ink was immediately deposited onto cleaned GC substrates via drop-casting and subsequently dried at 60 °C in static air.

Physico-chemical characterization

SEM images were recorded on a JEOL 7401F at 10 kV. Image J (program version 1.39u, <http://rsbweb.nih.gov/ij>) for the analysis of pore diameter, film thickness, size of Pt particles and for fast Fourier transformed (FFT) images. TEM images were recorded on a FEI Tecnai G² 20 S-TWIN operated at 200 kV from film samples scraped off the substrates and deposited on carbon-coated copper grids. To determine the amount of Pt contained in the Pt/OMC films, the so called "mass depth" (units: $\mu\text{g}_{\text{element}} \text{ per } \text{cm}^2_{\text{substrate}}$) was calculated using the STRATAGEM film analysis software (v 4.3) based on wavelength dispersive X-ray (WDX) spectra analyzed with a JEOL JXA-8530F electron microprobe at 7 and at 10 kV.¹¹⁸

2D-SAXS patterns were recorded on Pt/OMC-coated thin silicon wafers (50 μm) at the B03 beamline (DESY, Hamburg, Germany) with a calibrated radiation energy of 12.956 keV. The SAXS data were processed employing the software FIT2D Version V12.077. XRD was recorded on a Bruker D8 Advance (Cu K α radiation) with grazing incident beam (1°). Reflections were assigned using the Powder Diffraction Files database and further analyzed via Rietveld refinement using the Topas software (V4.2, Bruker-AXS). Reflection profiles were fitted using the Fundamental Parameter approach and a 4th order Chebyshev polynomial as background. Scale factor, lattice parameters of the phases and broadening of the reflections by Gaussian and Lorentzian contributions were refined taking Zero point errors into account. The Scherrer equation (volume-weighted FWHM) was used to estimate the crystallites coherence length taking instrumental line broadening into account.

The electrical conductivity of Pt/OMC coated on SiO₂ substrates was measure with a Keithley Model 6517B Electrometer employing an 8x8 pin probe head with an alternating polarity sequence of the pins.

The pore system of Pt/OMC powder samples was analyzed from N₂ sorption isotherms recorded at 77 K on a Quantachrome Autosorb-iQ. The samples were degassed in vacuum at 150 °C for 2 h prior to sorption analysis. Surface area and pore size were

evaluated with a NLDFT equilibrium Kernel and a model assuming cylindrical pores. The calculation model is available in Quantachrome ADiQwin software (Version 3.01).

XP spectra of Pt/OMC film surfaces were recorded with an AXIS Ultra DLD electron spectrometer manufactured by Kratos Analytical, UK using monochromated Al-K α excitation. Spectra were taken by setting the instrument to the hybrid lensmode and the slot mode providing approximately a 300 × 700 μm^2 analysis area. The binding energy scale was corrected for charging using an electron binding energy of 284.6 eV for the C_{1s} level of graphite. Peak fitting of XP spectra was performed with a Lorentzian-Gaussian sum function peak shape model using the Unifit 2013 software (Unifit Scientific Software GmbH, Leipzig, Germany). For all spectra Shirley backgrounds were used.

Electrocatalytic testing in the hydrogen evolution reaction

All electrocatalytic testing was performed in 0.5 M H₂SO₄ electrolyte (Fixanal, Fluka Analytical) using a three-electrode disc setup (Pine MSR rotator, BioLogic SP-200 potentiostat) with a reversible hydrogen electrode "RHE" (Gaskatel, HydroFlex) as a reference, Pt gauze (Chempur, 1024 mesh cm⁻², 0.06 mm wire diameter, 99.9%) as counter electrode and Pt/OMC-coated GC discs rotated at 2000 rpm as working electrode. All potentials in this work are referenced to the RHE corrected. The working electrodes were prepared by cutting 6 mm circular discs from larger Pt/OMC-coated GC substrates. Prior to catalytic testing the electrolyte solution was purged for at least 30 min with nitrogen. The HER performance was assessed recording 50 cyclic voltammograms in a potential window between 50 and -210 mV vs. RHE at a scan rate of 20 mV s⁻¹. Impedance spectra were recorded prior to CV testing to enable a correction for ohmic losses.

4.3 Results and Discussion

The following sections describe first the physico-chemical properties of Pt/OMC catalyst films. Thereafter, the influence of the applied carbonization temperature film structure, composition and electrical conductivity is discussed. Finally, the HER activity and stability is assessed and compared to commercial reference catalysts.

Pt/OMC films carbonized at 800 °C

Figure 9 presents exemplarily the structural features of a Pt/OMC film (ca. $0.15 \mu\text{g}_{\text{Pt}}/\text{cm}^2_{\text{substrate}}$) after carbonization in N_2 atmosphere at 800 °C. The figure displays SEM images in (a) top-view and (b) cross-section, (c,d) corresponding 2D-SAXS patterns recorded in transmission with a beam incident angle of $\beta = 90^\circ$ and $\beta = 10^\circ$ relative to the substrate surface as well as (e) TEM and (f) HR-TEM images of a film segment.

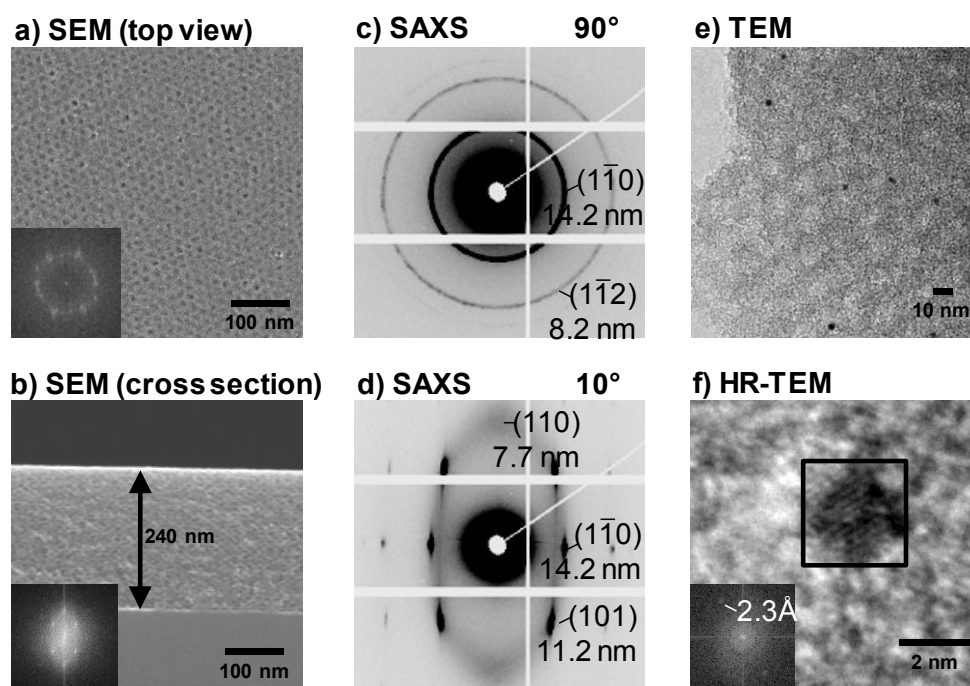


Figure 9. Structure of a Pt/OMC film carbonized at 800 °C: a) Top-view SEM image with FFT inset, b) cross-section SEM image with FFT inset, (c, d) 2D-SAXS pattern recorded in transmission mode with an incident angle of 90° and 10°, and e) TEM micrograph in bright field mode as well as f) HR-TEM of a Pt particle with corresponding FFT inset.

Top-view SEM images of the films (Figure 9a) show a crack-free and homogeneous surface completely covered with mesopores of about 9 nm diameter. The pores are well ordered as evidenced by the FFT of the SEM image (inset in Figure 9a), which presents numerous bright spots arranged on a ring. The corresponding pore spacing amounts to approx. 15 nm.

Cross-section SEM (Figure 9b) confirms that the homogeneous films are completely penetrated by ordered mesopores throughout the film thickness (ca. 240 nm). The sizes of the formed ellipsoidal mesopores amounts to 9 nm parallel and 4 nm in the normal

direction relative to the substrate surface. The FFT of the cross-section-SEM image (inset in Figure 9b) shows corresponding intensity spots. The regular pore spacings derived from FFT amount to 14.5 nm parallel and 5.5 nm normal to the substrate surface. The observed ellipsoidal distortion of the pore shape is a common phenomenon reported for oxide (TiO_2 ⁷⁸, Pd/TiO_2 ¹⁰⁴, IrO_2 ⁶⁸, Ru/Ir/TiO_2 ¹¹⁹, MgO ¹²⁰, ZnO ¹²¹, NiO ¹⁰², SnO_2 ⁹⁸) and carbon films^{44, 45, 81} templated by polymer micelles.^{78, 98} The distortion results from uniaxial shrinking normal to the substrate surface upon drying of the deposited films.¹²²

SAXS data confirm pore ordering and film contraction. Patterns recorded in transmission with 90° (Figure 9c) feature two distinct circular diffraction rings that can be assigned to the $(1\bar{1}0)$ plane of a cubic pore lattice with a periodic distance of 14.2 nm as well as the $(1\bar{1}2)$ plane with a periodic distance of 8.2 nm. SAXS curves recorded at lower incidence angles of 10° (Figure 9d) show an ellipsoidal shape. The bright scattering spots can be attributed to the lattice planes $(1\bar{1}0)$ with a periodic distance of 14.2 nm as well as a (101) plane with a periodic distance of 11.2 nm of a contracted cubic pore system.⁹⁹ Due to the low angle of incidence also the (110) plane, which is perpendicular to the substrate, can be observed. The regular pore distance normal to the substrate surface amounts to 7.7 nm, which indicates that the deposited films shrink by about 46% during template removal and carbonization.

TEM micrographs of the film confirm the abundant presence of templated and ordered mesopores in the whole film volume (Figure 9e). Moreover, dark spots evidence the presence of Pt particles of about 2.7 ± 0.5 nm diameter well dispersed inside the pore system. Lattice fringes visible in HR-TEM images (Figure 9f) indicate a high crystallinity of the particles. The spacing of the fringes amounts to 2.3 Å, which agrees well with the (111) lattice planes present in the cubic Pt structure (04-0802, $\text{Fm}\bar{3}\text{m}$).

N_2 physisorption analysis of a corresponding Pt/OMC powder sample (see Supplement Figure S6) shows a hysteresis loop of the isotherm indicative of mesopores. Moreover, a steep initial rise at low pressures evidences also the presence of micropores. About 60% of the total pore volume of $0.48 \text{ cm}^3/\text{g}$ can be attributed to mesopores, about 40% to micropores. NLDFT evaluation of the sorption data (Supplement Figure S6b) indicates a narrow pore size distribution centered around 5.1 nm and a total surface area of $875 \text{ m}^2/\text{g}$. Bulk and surface composition of the catalysts were analyzed for a Pt/OMC film carbonized at 700°C ($2.0 \mu\text{g}_{\text{Pt}}/\text{cm}^2$) via XPS and XRD as presented in the Supplement Figure S7. Grating incidence XRD (Supplement Figure S7a) shows reflections which can be attributed to metallic platinum along with a faint reflection that can be assigned to the stacking of graphene. The Pt_{4f} region of the XPS signal (Supplement Figure S7c) is dominated by a signal that corresponds to metallic Pt.¹²³ An intense peak in the C_{1s} region (Supplement Figure S7d) confirms the dominating presence of graphitic carbon.¹²⁴

Hence, the film formation process of mesophase ordering, carbonization and template removal works well despite the presence of additional Pt species. Moreover, pore confinement appears to prevent Pt particle sintering even at the applied temperature of 800°C . The resulting Pt/OMC films consist of metallic crystalline Pt particles of about 2.7 nm size distributed in a pore system formed by ordered and interconnected mesopores.

Influence of the carbonization temperature on catalyst formation

Beside mesophase formation the thermal treatment that forms particles and stabilizes the carbon network proved to be the most critical synthesis step. Hence, the influence of carbonization temperature on nanoparticle formation, electrical conductivity and film morphology was studied between 400 and 900 °C. Figure 10 presents corresponding SEM images in (a) top-view and (b) cross-section, (c) TEM data, (d) Pt particle sizes derived from TEM as well as (e) the films electrical conductivity for Pt/OMC films synthesized with 4.5 mg of $\text{Pt}(\text{NO}_3)_2$ ($0.4 \mu\text{g}_{\text{Pt}}/\text{cm}^2_{\text{substrate}}$, from WDX). Complementary compositional analysis (mass loading of Pt, C and O, from WDX) is presented in the Supplement Figure S8.

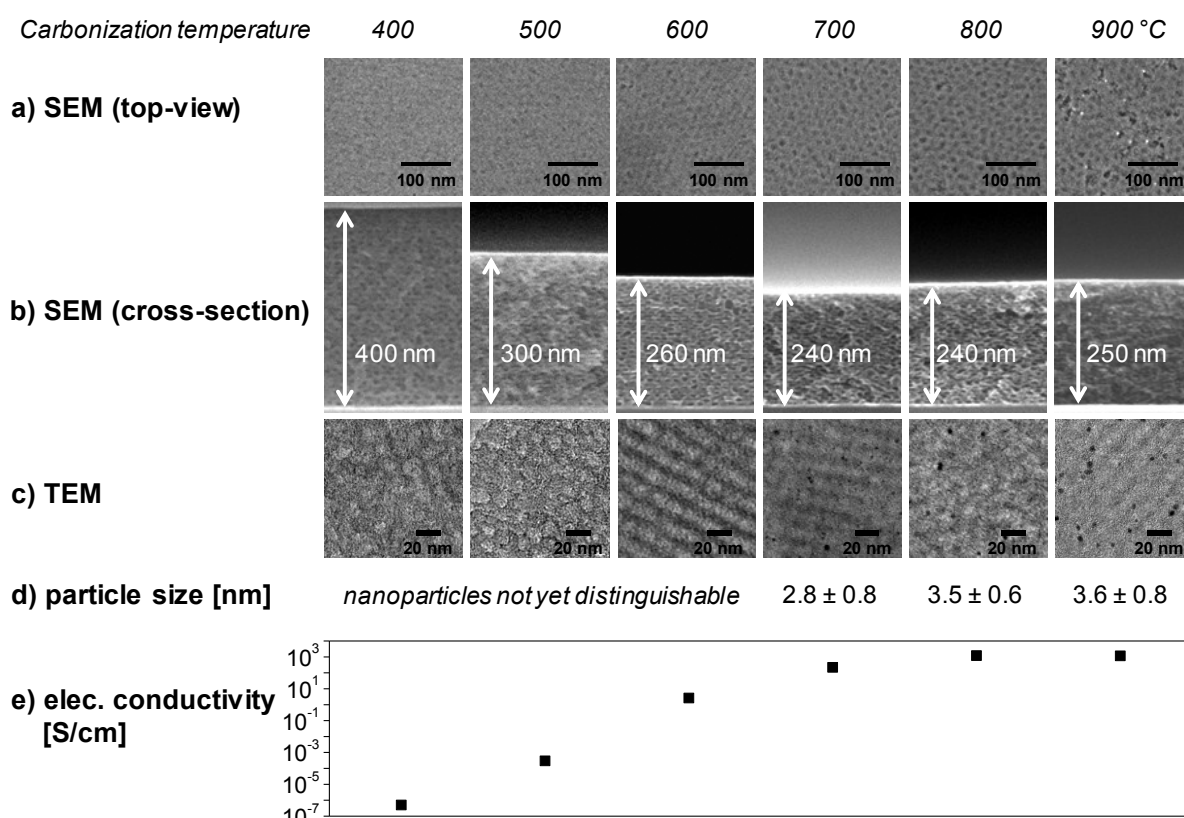


Figure 10. Influence of the carbonization temperature on F127-templated Pt/OMC films. The films were carbonized in N_2 atmosphere for 3 h: a) top-view SEM images, b) cross-section SEM images, c) TEM images in bright field mode, d) diameter of measured particles from TEM (particles detectable for $T_{\text{carb}} = 700, 800$ and 900 °C), e) electron conductivity from sheet conductivity measurements.

Top-view SEM images (Figure 10a) show that the films porosity progressively evolves with increasing carbonization temperature. At 400 °C and 500 °C only a very faint contrast indicative of mesopore formation can be seen. Above 600 °C pores become clearly visible. Carbonization at 900 °C induces the partial collapse of pore walls and the formation of large Pt particles (ca. 10 nm) on the films outer surface. Both observations indicate that carbonization at 900 °C degrades the carbon support and sinters the formed Pt particles.

Cross-section SEM images (Figure 10b) confirm the impact of temperature on mesopore formation and allow the analysis of film thickness evolution. Pt/OMC films shrink from about 400 nm film thickness (400 °C) to 300 nm (500 °C) and 260 nm (600 °C), but retain this thickness value within the range of experimental accuracy up to 900 °C. Hence, carbonization of the precursor polymer requires at least 600 °C, which is consistent with literature reports on Pt free OMC films.⁴⁵

TEM (Figure 10c) provides complementary information on the size of formed Pt particles (Figure 10d). Up to 600 °C Pt particles are not yet visible in the TEM. Carbonization at 700 °C forms Pt particles with a diameter of 2.8 ± 0.8 nm distributed throughout the porous carbon. Temperatures of 800 °C (3.5 ± 0.6 nm) and 900 °C (3.6 ± 0.8 nm) induce a slight particle growth within the confined mesopore system. However, a small fraction of the Pt particles that is not confined in mesopores, i.e. located on the films outer surface, grows at 900 °C to about 10 nm size (Figure 10a, 900 °C), confirming the critical role of the templated mesopore system for the stabilization of small particle sizes. A similar stabilization effect has been reported by Schüth et al. for Pt nanoparticles located inside hollow graphitic spheres (900 °C⁷⁰) and AuPt nanoparticles inside porous carbon shells (1000 °C¹²⁵).

Electrocatalysis requires that the catalyst support is sufficiently conductive. Figure 10e shows the corresponding electrical film conductivity (log scale). Starting out with films of very low conductivity at 400 °C (5×10^{-7} S/cm) the values increase by orders of magnitude at 500 °C (3×10^{-4} S/cm), 600 °C (3 S/cm) and 700 °C (2×10^2 S/cm). At 800 °C and 900 °C a maximum of about 1×10^3 S/cm is reached, indicative of a highly conductive catalyst film.

The increasing graphitization of the film at higher temperatures is also reflected by the films composition, e.g. the "mass depth" of the species Pt, O and C as computed from WDX analysis (Supplement Figure S8). The amount of non-volatile Pt (ca. $0.5 \mu\text{g}/\text{cm}^2$) remains constant throughout the studied temperature range as expected. However, values recorded for C decrease from $42 \mu\text{g}/\text{cm}^2$ (400 °C) to about 20 - 26 $\mu\text{g}/\text{cm}^2$ (500 °C and higher temperatures) which can be attributed to removal of volatile organic compounds and decomposition/removal of the polymer template upon carbonization. Moreover, also the O content decreases continuously from $9 \mu\text{g}/\text{cm}^2$ (400 °C) to $4 \mu\text{g}/\text{cm}^2$ (500 °C), $3 \mu\text{g}/\text{cm}^2$ (600 °C) and finally ca. $2 \mu\text{g}/\text{cm}^2$ (700-900 °C). The removal of oxygen is attributed to the decomposition of the oxygen-containing precursors (resorcinol, formaldehyde) corresponds well with the drastic increase in electrical conductivity up to 700 °C.

The combined evidence suggests that the formation of a highly conductive carbon support with open porosity and clearly observable small Pt nanoparticles throughout the sample requires a temperature of about 700 °C. Confinement effects retain the small particle size also at 800 °C. However, temperatures exceeding 800 °C degrade the pore walls and induce particle sintering on the films external surface.

HER performance

The electrocatalytic performance of the developed Nafion-free Pt/OMC catalysts was studied performing the Hydrogen Evolution (HER) tests in a RDE setup with 0.5 M sulfuric acid using repeated potential cycles. Pt/OMC catalysts with the same Pt loading ($0.4 \mu\text{g}_{\text{Pt}}/\text{cm}^2$) but carbonized at different temperatures (400, 500, 600, 700, 800, 900 °C) were analyzed via cyclic voltammetry (CV) after exposure to a mild oxidative cleaning (20 min at 400 °C in air). Figure 11a depicts the 3rd recorded cycle for each catalyst.

All catalysts are active in the HER, but the applied carbonization temperature strongly influences the respective activity. Films carbonized at 400 °C show hardly any current response. With increasing carbonization temperature a monotonous increase in activity is observed between 500 and 700 °C that reaches maximum with a current density of $-16.7 \text{ mA}/\text{cm}^2$ at -50 mV overpotential (700 °C). Carbonization at 800 °C and 900 °C strongly decrease the activity.

The observed activity trends can be rationalized by the observed structural features of Pt/OMC. Films carbonized at 700 °C exhibit a fully developed pore system (Figure 10a/b/c), small Pt particles (Figure 10d) as well as high electrical conductivity of the support (Figure 10e). The increase in activity up to 700 °C correlates with two observations that cannot be separated in the present approach, i.e. the formation of small Pt particles (Figure 10c/d) as well as an increase in electrical conductivity (Figure 10e). The decrease in activity at carbonization temperatures exceeding 700 °C could be related to the degradation of the pore system and particle sintering as visible in SEM (Figure 10a, 900 °C).

Subsequent tests fixed the carbonization temperature of Pt/OMC to the optimal temperature, i.e. 700 °C. In order to identify optimal Pt loadings and test for possible transport limitations associated with higher Pt loadings similar Pt/OMC catalysts were prepared with different Pt amounts of 0.84 and $1.2 \mu\text{g}_{\text{Pt}}/\text{cm}^2$. Each synthesis was repeated twice to test the synthesis reproducibility. Additional Pt/Vulcan/Nafion catalysts were synthesized via classical Nafion ink ($1 \mu\text{g}_{\text{Pt}}/\text{cm}^2$) and tested along with a polycrystalline Pt foil as a reference.

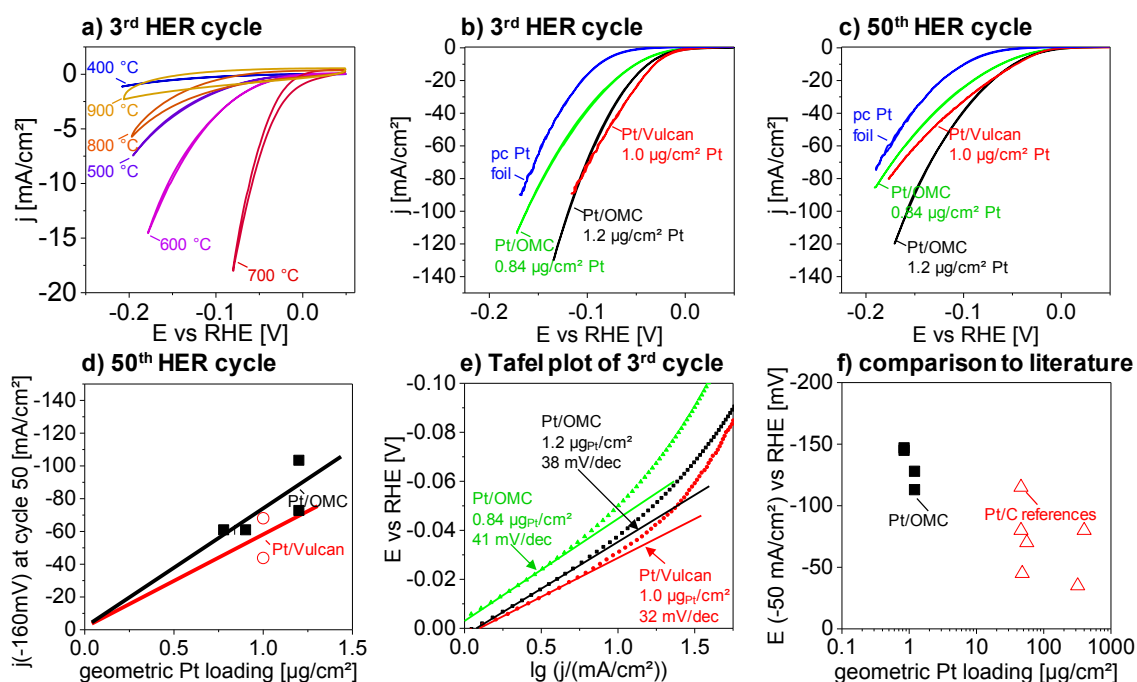


Figure 11. Electrochemical performance of Pt-containing catalyst films. Cyclic voltammetric (CV) measurement were recorded in the HER regime with 20 mV/s in 0.5 M sulfuric acid. a) 3rd cycle of a CV measurement recorded of F127-templated Pt/OMC catalyst films ($0.4 \mu\text{g}_{\text{Pt}}/\text{cm}^2$) carbonized for 3 h in N_2 atmosphere at the indicated temperature and additionally treated for 20 min in air. b-e) Mesoporous Pt/OMC catalysts (carbonized at 700°C) with Pt loading of $1.2 \mu\text{g}/\text{cm}^2$ (black) and $0.84 \mu\text{g}/\text{cm}^2$ (green) are compared to a polished pure polycrystalline Pt plate (blue) and to a commercial Pt/Vulcan carbon catalyst (red) with a Pt loading of $1 \mu\text{g}/\text{cm}^2$. b) 3rd cycle of a CV measurement. c) 50th cycle. d) Current density at an potential of -160 mV vs RHE at the 50th cycle plotted against the geometric Pt loading of Pt/OMC (black solid squares) and Pt/Vulcan reference (red hollow circles) catalysts. Each point represents one measured catalyst. e) Tafel evaluation of the 3rd cycle (potential E vs. $\log(\text{current density})$). f) Overpotentials at $-50 \text{ mA}/\text{cm}^2$ plotted against the geometric Pt loading (log scale): Pt/OMC (black solid squares) and recently published Pt/C reference catalysts (red triangles):^{107, 126-129}.

Figure 11b depicts the corresponding HER current responses in the 3rd cycle. All Pt/OMC coatings show excellent HER activity (Figure 11b). With Pt loading increasing from $0.84 \mu\text{g}/\text{cm}^2$ to $1.2 \mu\text{g}/\text{cm}^2$ also the observed HER activity increases. Pt/Vulcan/Nafion catalysts prepared with a similar Pt loading of $1 \mu\text{g}_{\text{Pt}}/\text{cm}^2$ show similar current densities at low potentials, but are outperformed by Pt/OMC at high currents. Moreover, the unsupported polycrystalline Pt foil exhibits a significantly lower performance when compared to both types of supported catalysts.

The excellent performance of Pt/OMC catalysts is retained also after 50 repeated potential cycles (Figure 11c). All tested catalysts, and in particular Pt/Vulcan/Nafion, show a decrease in current density of about 40 to 50% with repeated cycling. Such a decrease in HER performance over Pt-based catalysts has been reported in literature to originate from organic impurities found even in highly purified electrolytes,⁸⁷ where concentrations as low as $10^{-10} \text{ mol}/\text{dm}^3$ can lead to blocking of active site.^{101, 105} The stronger initial decrease in current densities observed for the Nafion based catalyst indicates also a current related to Nafion degradation could contribute to the CV signal. After 50 cycles Pt/OMC clearly

outperforms Pt/Vulcan/Nafion at comparable Pt loading for high current densities and potentials more negative than -100 mV.

The activity differences can be observed more readily from Figure 11d that plots the current density at -160 mV vs. RHE for different Pt loadings of Pt/OMC and Pt/Vulcan/Nafion. Each point in the diagram represents a different catalyst. The observed HER current of Pt/OMC scales (within the margin of error) linearly with the geometric Pt loading. When compared for high current densities at the same Pt loading, Pt/OMC outperforms Pt/Vulcan/Nafion by about 30%. This improved performance of Pt/OMC could result from several factors, e.g. an improved mass transport within the homogeneous carbon layers that are fully penetrated by ordered and 3D-connected templated mesopores, the high electrical conductivity throughout the complete catalyst as well as the absence of Nafion which avoids blocking of active sites.

Mechanistic insights can be gained by evaluation of corresponding Tafel plots (Figure 11e) of the 3rd cycle, which plots the potential E vs. log of the current density. According to literature the Tafel slope b can be indicative of differences in the rate-determining step of the HER.^{12, 18} Values of about 40 mV/dec are typically attributed to electrochemical formation of molecular hydrogen (Heyrovsky reaction, $MH_{ads} + H^+ + e^- \rightleftharpoons M + H_2$), whereas values of ~ 30 mV/dec refer to rate limitation by chemical H_2 desorption via recombination of adsorbed H atoms (Tafel reaction, $2 MH_{ads} \rightleftharpoons 2 M + H_2$). Tafel slopes observed for the studied Pt/OMC catalysts amount to 41 mV/dec ($0.84 \mu g_{Pt}/cm^2$) and 38 mV/dec ($1.2 \mu g_{Pt}/cm^2$) (Figure 11e). For Pt/Vulcan/Nafion a slope of $b = 32$ mV/dec is observed. This value agrees well with data reported in literature for different Pt/C/Nafion catalysts tested in 0.5 M H_2SO_4 , reported in literature, i.e. about 29 to 34 mV/dec.^{108 128-130}

Both type of catalysts, i.e. Pt/OMC and Pt/Vulcan/Nafion, deviate from linear Tafel behavior at current densities above ca. -6 to -8 mA/cm², indicating that transport effects can play a significant role (Figure 11e). However, the observed increase in Tafel slope occurs much more pronounced on Pt/Vulcan/Nafion than on Pt/OMC. Hence, the superior performance of the Nafion-free Pt/OMC in particular at higher current densities (Figure 11d) is likely to originate from better transport properties than Nafion based materials.

Figure 11f compares eventually the performance of the developed Nafion-free Pt/OMC catalysts with Pt/C catalysts reported in literature. The Figure plots the overpotential that is required to reach a current density of -50 mA/cm² vs. the respective geometric Pt loading (log scale). The further left in the diagram a catalyst is located, the lower is the amount of Pt that is required to reach a given HER performance. All catalysts shown in Figure 11f were tested in 0.5 M H_2SO_4 electrolyte. The developed Pt/OMC catalysts can be found in the left region of the diagram at overpotentials of -113 mV (50th cycle) for a Pt loading of $1.2 \mu g_{Pt}/cm^2$. Catalysts reported in literature required clearly higher Pt loadings to achieve the same performance. Reddy et al. reported a Nafion-based Pt/Vulcan XC 72 catalyst (Dupont, 20 wt% Pt) with a loading of $48 \mu g_{Pt}/cm^2$ that required -45 mV to reach a current density of 50 mA/cm².¹²⁶ Gao et al. presented a Nafion-based 20 wt% Pt/Vulcan XC 72 catalyst (Johnson-Matthey) that required $56 \mu g_{Pt}/cm^2$ and -70 mV to

reach -50 mA/cm^2 .¹³¹ Another Nafion-based catalyst Pt on carbon black (Johnson Matthey) reported by Wu et al. required -35 mV at a Pt loading of $320 \mu\text{g}_{\text{Pt}}/\text{cm}^2$.¹²⁹ Hence, Pt/OMC reaches the same performance as Nafion based catalysts reported in literature, but at a significantly lower required loading of Pt.

4.4 Conclusion

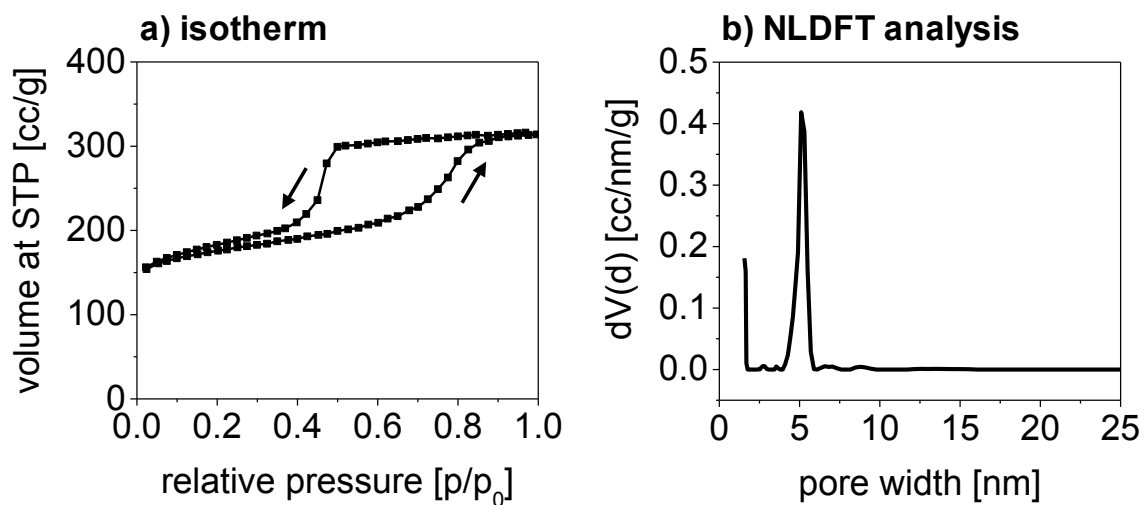
We report a new synthesis route for binder-free mesoporous Me/OMC catalyst films with homogeneous morphology based on dip-coating of polymeric carbon precursors in the presence structure-directing polymer micelles as well as molecular platinum precursors. The developed synthesis route is illustrated for Pt-based catalysts and produces homogeneous coatings comprised of small Pt particles located in size-controlled mesopores that are formed from a partially graphitized carbon structure. The mesoporous Pt/OMC coatings possess a high surface area, good pore connectivity as well as excellent electrical conductivity, i.e. all properties required for a good electro catalyst. The films clearly outperform Nafion-based Pt/C catalysts in HER in particular at high current densities that approach practical operation conditions. The enhanced performance can be explained by the abundant presence of mesopores in the film, the improved accessibility of the active centers and the absence of detrimental Nafion influences.

The proposed synthesis concept is not limited to the incorporation of Pt into mesoporous carbon coatings. The introduction of other active metal species can pave the way to the synthesis of a wide range of catalytic systems that rely on conductive carbon supports with high surface area and mesoporosity. Moreover, even the synthesis of bimetallic supported catalysts should be feasible and allow a further decrease in the amount of Pt required for typical electrocatalytic reactions. A post-modification of the presented Pt/OMC catalysts with Nafion could enable for the first time a direct analysis of the influence of binders on the transport properties of porous carbon based catalysts.

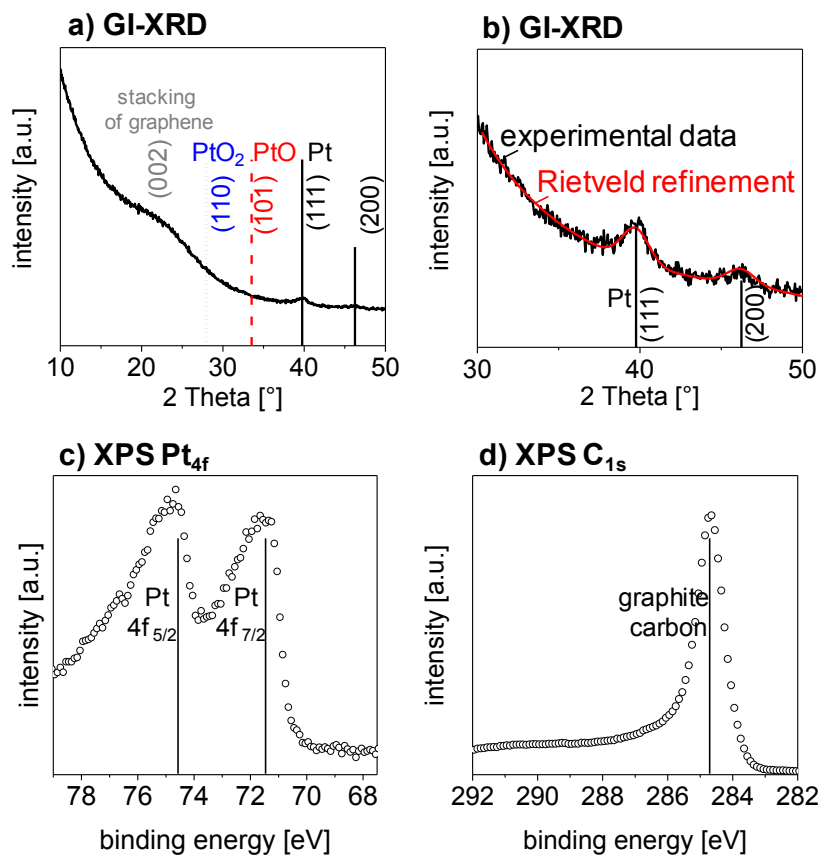
4.5 Acknowledgement

The authors thank ZELMI (TU-Berlin) for providing infrastructure for electron microscopy. We thank B. Paul for SEM measurements. DB, MB and RK acknowledge generous funding from BMBF under contract FKZ 03EK3009. RK particularly appreciates support from the Einstein Stiftung Berlin (EJF-2011-95). Portions of this research were conducted on beamline B1 at light sources DORIS III and PETRA III at DESY with assistance by Ulla Vainio and Björn Eckhardt.

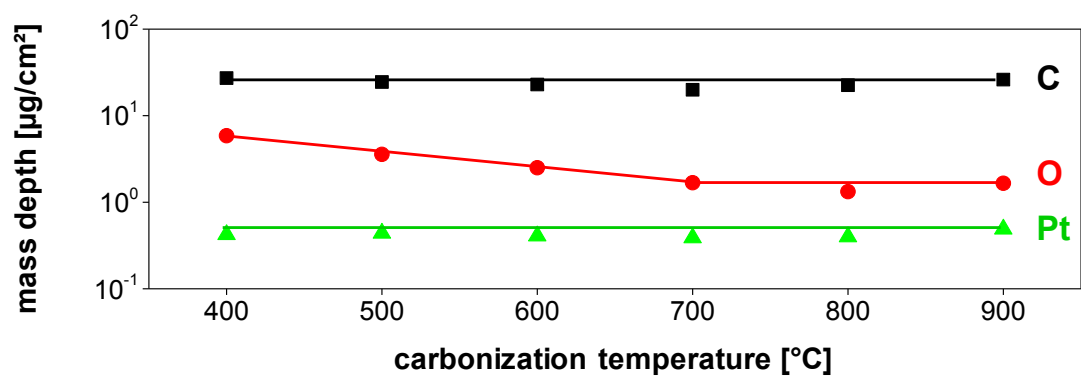
4.6 Supporting Information



Supplement Figure S6. N₂ physisorption analysis of Pt/OMC powder. The material was carbonized for 3 h in nitrogen atmosphere at 700 °C. a) full isotherm measured at 77 K, b) NLDFT evaluation of the isotherm with assumed cylindrical pore configuration. The calculated specific surface area amounts to 875 m²/g.



Supplement Figure S7. XRD pattern in gracing incidence configuration and XPS spectra of F127-templated Pt/OMC films carbonized at 700 °C in N₂ atmosphere: a) XRD pattern with indicated reflections of orthorhombic PtO₂ (PDF: 04-0802), tetragonal PtO (43-1100) and cubic Pt (04-0802), b) XRD pattern (black) and Rietveld refinement (red); c) and d) XPS spectra (black hollow spheres) in the regions of Pt_{4f} and C_{1s} with indicated binding energies of metallic Pt and graphite carbon.



Supplement Figure S8. Influence of the carbonization temperature on the mass depth of C, O and Pt in F127-templated Pt/OMC films. The films were carbonized in N_2 atmosphere for 3 h.

5 Ru and Pt-containing mesoporous carbon films

To be submitted

Mesoporous RuPt/C coatings with significantly decreased Pt content efficiently catalyze the HER

Denis Bernsmeier¹, Michael Bernicke¹, Erik Ortel², Roman Schmack¹, Jörg Polte³, Ralph Kraehnert¹

¹ Department of Chemistry, Technische Universität Berlin, Straße des 17. Juni 124, 10623 Berlin

² BAM - Federal Institute for Materials Research and Testing, Division 6.1, Unter den Eichen 44-46, 12203 Berlin

³ Department of Chemistry, Humboldt Universität zu Berlin, Brook-Taylor Str. 2, 12489 Berlin

Abstract

Platinum is the most active catalyst for the electrolytic hydrogen evolution reaction (HER). Yet, it is expensive as well as scarce and therefore needs to be used most efficiently. In order to reduce the amount of necessary Pt we propose a synthesis approach to alloyed RuPt nanoparticles which retain the enhanced catalytic activity of Pt. These particles are dispersed on an electrically conductive, highly accessible and stable carbon coating. The synthesis route relies on the co-deposition of ionic Ru and Pt precursors together with a carbon precursor with micelles as structure-directing pore templates. The films adhere without the use of binding agents like Nafion, which can decrease catalytic activity by blocking of pores and active surface sites. Carbonization in reducing atmosphere (H_2/Ar) leads to ordered mesoporous carbon films with a controlled morphology and a very high electrical conductivity. The films exhibit well-dispersed small nanoparticles.

The presented RuPt catalyst films show a four times higher activity per Pt in the hydrogen evolution reaction compared to conventional Nafion-based Pt/C reference catalysts. Moreover, the synthesis approach represents a generic approach to ordered mesoporous carbon coatings containing metal nanoparticles.

key words: hydrogen evolution reaction, bimetallic nanoparticles, ordered mesoporous carbon coatings, soft-templating

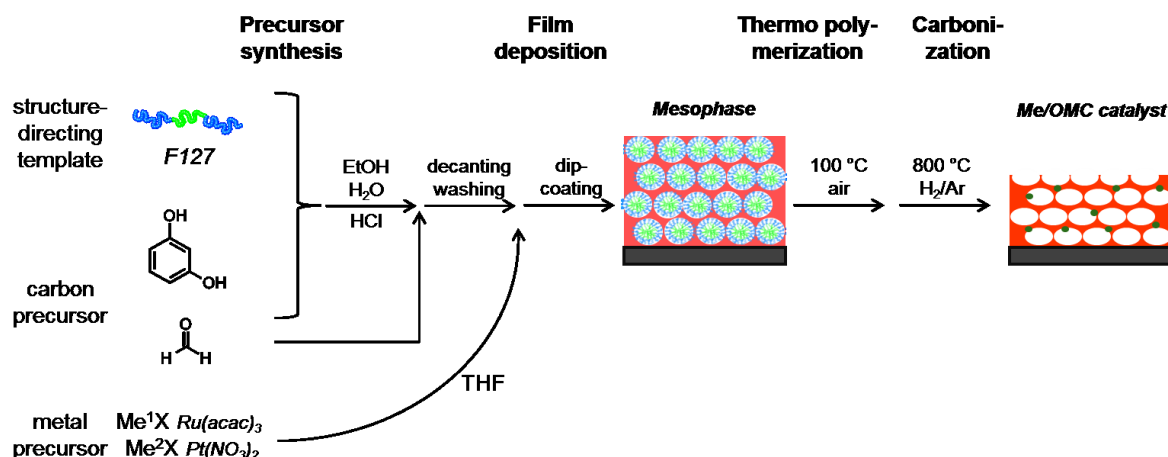
5.1 Introduction

Platinum is the most active metal that catalyzes the hydrogen evolution reaction (HER) in acidic electrolytes.^{6, 132} It is also commonly used in electrocatalytic alcohol oxidation reactions^{133, 134} as well as the oxygen reduction reaction^{135, 136}. However, Pt is scarce, expensive and needs to be used most efficiently.^{9, 107} Typical catalysts, therefore, maximize the exposed active surface area by immobilization of Pt nanoparticles on conductive and porous carbon materials.¹³³⁻¹³⁸ The Pt content of such nanoparticles can be decreased further when Pt is used in the form of bimetallic nanoparticles, where the second metal can contribute to enhanced Pt dispersion and to an electronic modification of the active Pt atoms. Bimetallic HER catalysts have been reported in core-shell configuration (e.g. Pd/Pt¹⁰⁷, Bi/Pt⁴) as well as alloys (e.g. BiPt⁴, CuPt.¹³⁹). However, the synthesis of core-shell structure can be quite tedious and complicated and is often limited by the thermal stability of the formed structures.

Ruthenium appears to be an excellent candidate for the synthesis of a bimetallic Pt-based HER catalysts. For more than 20 years it has been the cheapest of all noble metals and is about 10-30 times cheaper than Pt.¹⁴⁰ Furthermore, Ru shows a high activity in the HER and is stable in acidic medium. Elbert et al. studied RuPt in the hydrogen oxidation and hydrogen evolution and proved the enhanced catalytic activity.¹⁴¹ However, they used a conventional preparation method based on Nafion, which has been reported to block pores and active sites.^{33, 34}

Ordered mesoporous carbon (OMC) coatings show a high surface area, a controllable pore size and a high electrical conductivity as well as chemical inertness.^{40, 44, 110-112} Therefore, they are ideal candidates for electrode coatings. OMC coatings with a well-defined structure can be synthesized via soft-templating. Micelles of amphiphilic polymers (e.g. block-copolymers) arrange together with a polymeric carbon precursor (e.g. a resin from a polycondensation reaction of phenol¹⁴², resorcinol⁴⁶ or phloroglucinol⁵² with formaldehyde) to a mesophasic film. A thermal treatment removes the template micelle and transforms the precursor into a graphitic carbon matrix.⁴⁵ Only metals like Fe⁵⁵ and Nb¹¹⁵ have been incorporated into OMC networks so far. The synthesis of OMC films containing nanoparticles of noble metals has not been reported.

Herein we present the first bimetallic Me/OMC catalyst film. The synthesis involves the co-deposition of ionic precursors with a compound of a resin from resorcinol and formaldehyde and a polymer template (F127). The procedure is described in Scheme 8. The polymer compound is dispersed in a solvent containing ions of Me¹ and Me². Films are deposited via dip-coating. After thermal treatment at 100 °C and subsequent carbonization homogeneous and electrically conductive carbon films with an ordered pore system are obtained. The films contain small well-dispersed nanoparticles.



Scheme 8. Illustration of the synthesis approach to bimetallic mesoporous Me/OMC catalyst films. The structure-directing triblock copolymer F127 (PEO-PPO-PEO) and resorcinol are dissolved in ethanol. After addition of hydrochloric acid, formaldehyde solution is added to start a polycondensation reaction. The derived polymeric resin is separated by centrifuging and then washed. The polymeric compound is redissolved in THF which contains a mixture of dissolved metal precursors. Under controlled conditions a film is deposited via dip-coating to obtain a homogeneous mesophasic film. After thermal treatment at $100\text{ }^\circ\text{C}$ in air and a subsequent carbonization under reducing atmosphere (H_2/Ar) a bimetallic mesoporous Me/OMC film is obtained.

The present contribution describes the film morphology of bimetallic RuPt/OMC and monometallic Ru/OMC films. Size and composition of the nanoparticles of RuPt/OMC are studied with STEM/EDX. The electrochemical HER performances of Me/OMC films with RuPt, Ru and Pt is compared to commercial Pt/C references demonstrating the high Pt-mass-based activity of RuPt/OMC.

5.2 Experimental

Chemicals

Formaldehyde (37 wt% in water), resorcinol, Pluronic F127 (PEO₁₀₆-*b*-PPO₇₀-*b*-PEO₁₀₆, M_w = 12 600 g/mol), 5%-Nafion solution and isopropanol were purchased from Sigma-Aldrich. Ethanol (EtOH, >99.9%, absolute) and tetrahydrofuran (THF, >99.9%, absolute) were purchased from VWR. 3 M hydrochloric acid (HCl) was prepared from a 12 M HCl (Alfa Aesar). Ru(III) acetylacetonate (Ru(C₅H₇O₂)₃, >99%) was obtained from Merck. Platinum(II) nitrate (Pt(NO₃)₂, 99.95%) was bought from ChemPur. All chemicals were used without further purification. Pt on Vulcan (BASF, XC 72R (Cat. No. 181, 10 wt% Pt) was employed as a reference catalyst. MilliQ water was used.

Substrate pre-treatment

Catalyst films were synthesized on different substrates. Single side polished and double side polished Si-wafer with (100)-orientation were purchased from University Wafers. Super-thin Si-wafers (50 μm) were employed for transmission SAXS measurements. Glassy carbon "Sigradur G" from HTW and SiO₂ glass microscope slides from Science Services. Si-wafer substrates were cleaned with a tissue containing ethanol and calcined in air (2 h, 600 °C) prior to film deposition. The glassy carbon (GC) substrates were polished with 0.05 μm alumina dispersion and immersed and ultrasonicated two times in water and ethanol and afterwards rinsed with ethanol. SiO₂ glass substrates for conductivity measurements were immersed and ultrasonicated in ethanol and afterwards cleaned with a tissue containing ethanol prior to coating.

Synthesis of RuPt-containing mesoporous carbon films

RuPt/OMC catalyst films were synthesized via dip-coating of different substrates employing a THF-containing solution of a carbon precursor, ionic Ru and Pt precursors and a structure-directing agent. In a centrifuge tube 1100 mg of resorcinol together with 300 mg of the template Pluronic F127 were dissolved in 4.5 mL of EtOH until a clear solution was obtained. Afterwards, 4.5 mL of 3 M HCl was added. The tube was shaken for five minutes. 1212 μL of formaldehyde (37% in water) was then added and the vial continuously shaken. After circa four minutes the solution became turbid. The white precipitate which formed was separated from the solution by centrifugation for 5 minutes at 7500 rpm ten minutes after the addition of formaldehyde. The remaining solution was discarded. The white precipitate was then washed with water and thereafter dissolved in 5 mL of THF containing 3.7 mg of dissolved Pt(NO₃)₂ and 34.2 mg of dissolved Ru(acac)₃. A clear dispersion with vinaceous color was obtained and used for dip-coating.

Catalyst films were deposited onto the clean substrates via dip-coating at 25 °C and 30% relative humidity (dipcoater: Coater 5 AC from IDLab). The coated substrates were transferred to a drying furnace and then thermally treated for 12 h at 100 °C in air for film stabilization. Afterwards the coated substrates were transferred into a tube furnace and heated with 1 K/min in H₂/Ar flow up to 800 °C, holding the temperature for 3 h, followed by subsequent cooling down in H₂/Ar flow to room temperature. For enhanced catalytic performance, films were additionally treated in a muffle furnace at 400 °C for five minutes in air. Afterwards, the films were transferred into a tube furnace and heated in H₂/Ar flow with 5 K/min up to 400 °C for 15 min, followed by subsequent cooling down in H₂/Ar flow to room temperature.

Synthesis of Ru-containing mesoporous carbon films

Ru/OMC catalyst films were synthesized nearly identically as RuPt/OMC films. The polymer compound was synthesized in the same way as described above. The white precipitate was produced in the same way and dissolved in 5 mL of THF containing 43.2 mg of dissolved Ru(acac)₃. A clear dispersion with vinaceous color was obtained and used for dip-coating. Films were deposited and thermally treated as described above.

Synthesis of Pt/C/Nafion reference coatings

Pt/C/Nafion reference catalysts were prepared according to established routes reported in literature.^{103, 116} In a typical synthesis 5 mg of Pt/Vulcan powder (10 wt% Pt) were dispersed in 3.98 ml of water. 20 µl of Nafion solution (5%) were added. After addition of 1 ml of isopropanol the mixture was sonicated for 15 min (Branson Sonifier, 6 W output power). The resulting ink was immediately deposited onto cleaned GC substrates via drop-casting and subsequently dried at 60 °C.

Physico-chemical characterization

SEM images were collected on a JEOL 7401F at 10 kV. TEM images were recorded on a FEI Tecnai G² 20 S-TWIN operated at 200 kV on fragments of film samples scraped off the substrates and deposited on carbon-coated copper grids. STEM/EDX investigations were carried out at a JEOL JEM 2200FS field-emission microscope operated at 200 kV. Images were evaluated with Image J program, version 1.39u (<http://rsbweb.nih.gov/ij>).

Amounts of Ru and Pt in the films, the mass depth was calculated using STRATAGEM film analysis software (v. 4.8) based on wavelength dispersive X-ray (WDX) spectra analyzed with a JEOL JXA-8530F electron microprobe at 10 kV.

Additionally Ru and Pt loadings were confirmed by ICP-OES from solutions of microwave digested films. Films coated on both sides of double side polished Si-wafers were digested for 40 min at 180 °C and 18 bar in a mixture of aqua regia and concentrated

sulphuric acid with a microwave instrument (Discover SP-D from CEM). ICP-OES was performed with a 715-ES from Varian. A four point calibration with the same acid mixture was employed.

Films coated on thin silicon wafers (50 μm) were used for 2D-SAXS measurements. 2D-SAXS patterns were collected at the B03 beamline at DESY synchrotron (Hamburg, Germany) with a calibrated radiation energy of 12.956 keV. The SAXS data were processed with the software FIT2D Version V12.077. XRD data were recorded on a Bruker D8 Advance (Cu K_α radiation) with grazing incident beam (1°). X-ray diffraction reflections were assigned using the Powder Diffraction Files database.

Two-point sheet conductivity measurements were performed with a Keithley Model 6517B Electrometer employing a 8x8 pin probe head with an altering polarity sequence of the pins.

Kr and N_2 isotherms were measured at 77 K with a Quantachrome Autosorb-iQ. The samples were degassed in vacuum at 150 $^\circ\text{C}$ for 2 h prior to physisorption analysis. The surface area was evaluated with BET. Pore size evaluation was done with a QSDFT equilibrium transition kernel assuming slit-like micropores and cylindrical mesopores.

X-ray induced photoelectron spectra (XPS) of film surfaces were recorded with an AXIS Ultra DLD electron spectrometer manufactured by Kratos Analytical, UK. Monochromated Al- K_α excitation was employed. Spectra were taken by setting the instrument to the hybrid lensmode and the slot mode providing approximately an analysis area of $300 \times 700 \mu\text{m}^2$. The binding energy scale was corrected for charging using an electron binding energy of 284.6 eV for the C_{1s} level of graphite. Peak fitting of XP spectra was performed with a Lorentzian-Gaussian sum function peak shape model using the Unifit 2013 software (Unifit Scientific Software GmbH, Leipzig, Germany). For all spectra Shirley backgrounds were used.

Adhesion of a carbonized RuPt/OMC coating to a glassy carbon substrate was tested by the "tape test" as describe in ASTM D3359 Standard Test Methods for Measuring Adhesion by Tape Test (<http://www.astm.org/Standards/D3359.htm>). An X-cut was made through the coating penetrating the substrate. An adhesive tape (Scotch-Tape) was applied over the cut. The tape was smoothed and then pulled away. Poorly adhered coatings would peel away with the tape whereas well-adhered coatings would be stable. SEM images before and after the test were taken.

Electrocatalytic testing in the hydrogen evolution reaction

Electrocatalytic testing was performed using a three-electrode disc setup (Pine MSR rotator, BioLogic SP-200 potentiostat) using a reversible hydrogen electrode "RHE" (Gaskatel, HydroFlex) as a reference, Pt gauze (Chempur, 1024 mesh cm⁻², 0.06 mm wire diameter, 99.9%) as counter electrode, and a coated GC disk as working electrode (WE). All potentials are referenced to the RHE. The WE was prepared by cutting 5 mm circular discs from larger Me/OMC coated GC substrates and mounting them on a rotating disk shaft. During testing the disc was rotated at 2000 rpm in the electrolyte (0.5 M H₂SO₄, Fixanal, Fluka Analytical). Prior to testing the electrolyte solution was purged for at least 30 minutes with N₂. HER performance was studied by cyclic voltammetry in a potential window of 50 to -250 mV with a scan rate of 20 mV s⁻¹. Impedance spectroscopy was measured to correct for ohmic losses.

5.3 Results and discussion

The first two sub-chapters describe the morphology of monometallic Ru and bimetallic RuPt/OMC catalyst films. The following part addresses the electrocatalytic performance in the HER of RuPt/OMC in comparison to monometallic Me/OMC (Pd, Pt, Ru) catalyst films. Finally, the electrocatalytic performance in the HER is compared to a commercial reference catalyst, i.e. Pt/Vulcan catalyst deposited with a Nafion binder.

Physico-chemical properties of Ru/OMC films

Ru/OMC films were synthesized by depositing films via dip-coating from a dispersion containing a RF-compound, a structure-directing template (F127) and dissolved Ru(acac)₃ in THF. Figure 12 shows structural features of a Ru/OMC film carbonized in H₂/Ar atmosphere at 800 °C. The figure presents SEM images in top-view (a) and cross-section (b), a TEM micrograph (c), a HR-TEM image (d), a XRD measurement with grating incidence beam (e) as well as a XPS measurement in the region of Ru 3d_{3/2} (f).

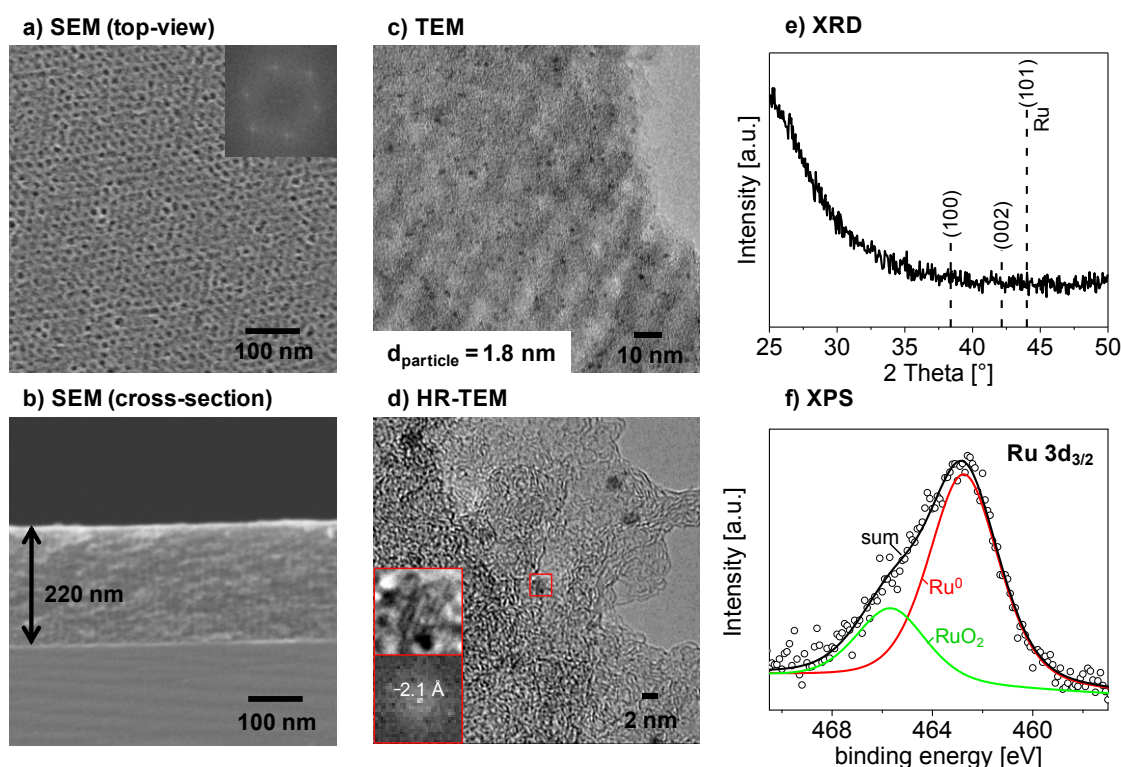


Figure 12. Physico-chemical analytics of a F127-templated Ru/OMC film carbonized at 800 °C in H₂/Ar. a) Top-view SEM image with FFT-inset. b) Cross-section SEM image with illustrated film thickness of 220 nm. c) TEM micrograph of a scraped off film sample. The dark dots represent small nanoparticles inside a mesoporous (light areas) carbon matrix. d) High-resolution TEM (HR-TEM) image. One marked particle is magnified in an inset alongside its FFT image. e) Grating-incidence XRD measurement with indicated reflection positions of hexagonal Ru (06-0663). f) XP spectrum and deconvolution of the Ru 3d_{3/2} regions.

A top-view SEM image of the film (Figure 12a) shows a homogeneous mesoporous morphology of the external film surface. The mesopores have a diameter of 9 nm. A FFT of the SEM image (inset) confirms the ordering of the pores, as numerous bright spots are arranged on an isotropic ring. The corresponding spacing of the mesopores amounts to 15 nm. A cross-section SEM image (Figure 12b) shows that mesopores are well arranged throughout the film volume. The film has a thickness of 220 nm. The mesopores have an ellipsoidal shape which originates from an uniaxial film shrinkage during template removal.⁹⁷

The geometric mass depth was determined via WDX measurements. A Ru/OMC film with a thickness of 220 nm has geometric loading of 22 $\mu\text{g}/\text{cm}^2$ of carbon, 2.2 $\mu\text{g}/\text{cm}^2$ of oxygen and 0.33 $\mu\text{g}/\text{cm}^2$ of ruthenium.

The pore morphology can be estimated from N_2 physisorption analysis of a corresponding Ru/OMC powder sample (see Supplement Figure S9). The steep rise of the isotherm at low relative pressures indicates the presence of microporosity. A hysteresis loop (a) suggests the abundant presence of mesopores. QSDFT evaluation (b) of the physisorption data indicates a narrow pore size distribution around 5.0 nm. About 65% of the total pore volume of 0.44 cm^3/g can be attributed to mesopores, 35% to micropores. The total accessible surface area from QSDFT analysis amounts to 883 m^2/g .

Ru/OMC films carbonized at 800 °C are highly electrically conductive. The conductivity amounts to 495 S/cm. This value is one order of magnitude higher than values reported in literature for OMC films containing cobalt oxide or vanadium oxide (20 – 40 S/cm after carbonization at 800 °C).⁶⁵

A TEM micrograph of a film segment confirms the abundant presence of templated mesopores inside the film (Figure 12c). Dark spots correspond to well-dispersed Ru particles inside the pore system with a diameter of 1.8 ± 0.4 nm. Lattice fringes in high-resolution (HR) TEM images (Figure 12d) suggest a high crystallinity of the particles. The regular distance of the fringes from a FFT (inset) amounts to 2.1 Å. This distance can be attributed to the (002) plane of hexagonal Ru (06-0663, 2.1 Å) or the (111) plane of cubic Ru (01-088-2333, 2.2 Å).

GI-XRD measurements of Ru/OMC films (Figure 12e) show no diffraction signal which can be attributed to Ru species. The absence of diffraction of Ru species is most likely caused by a small particle size, a low Ru concentration and a low film thickness. The increase of intensity towards lower angles (30-25°) can be attributed to a broad reflection from stacks of graphite at 24°.⁷⁶

A deconvoluted XP spectrum of a Ru/OMC film (Figure 12f) gives evidence for two present Ru species. A smaller signal with a maximal binding energy at 465.5 eV can be attributed to RuO_2 ¹⁴³ and a more intense peak at 462.7 eV can be attributed to metallic

Ru¹⁴⁴. The ratio from peak integration of Ru/RuO₂ is 74/26. Hence, the particles are basically composed of metallic and partially oxidized Ru. The surface of nanocrystalline Ru oxidizes at room temperature in air.¹⁴⁵

Altogether, we could show that Ru/OMC films carbonized at 800 °C contain Ru particles of about 1.8 nm in diameter. The mesopores are interconnected and the films show a high surface area. The film formation, including ordering of the mesophase, carbonization and template removal works well despite the presence of the Ru species.

Physico-chemical properties of RuPt/OMC films

Physico-chemical characterizations of a RuPt/OMC film are presented in Figure 13: Top-view (a) and cross-section (b) SEM image, corresponding 2D-SAXS patterns measured in transmission with a X-ray incident angle of $\beta = 90^\circ$ and 20° (c), X-ray diffraction pattern measured in grating-incidence (e), XP spectra measured in the regions of Pt 4f (d) and Ru 3d (f).

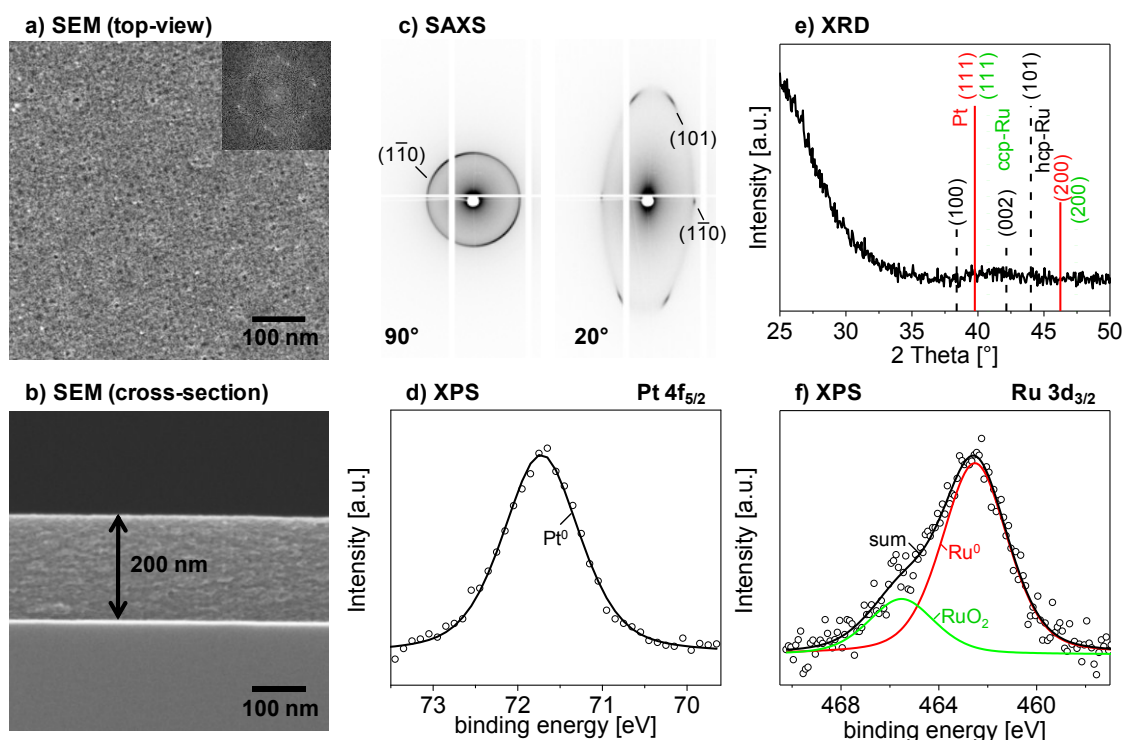


Figure 13. Physico-chemical analytics of a F127-templated RuPt/OMC film carbonized at 800 °C in H₂/Ar. a) Top-view SEM image with FFT-inset. b) Cross-section SEM image. c) 2D-SAXS pattern recorded in transmission mode with an incident angle of 90° and 20°, scattering reflections are assigned to a contracted cubic pore structure. e) Grating-incidence XRD measurement with indicated reflection positions of cubic Pt (04-0802), cubic Ru (01-088-2333) and hexagonal Ru (06-0663). d) and f) XP spectra and deconvolutions in the regions of Pt 4f_{5/2} (d) and Ru 3d_{3/2} (f).

A top-view SEM image (Figure 13a) shows a homogeneous surface of mesopores (dark areas) arranged at the surface plane. White dots can be attributed to metallic nanoparticles. The average diameter of the mesopores amounts to 8 nm. A FFT (inset in Figure 13a) of the SEM image shows bright spots arranged on a ring. The corresponding pore spacing amounts to circa 15 nm. Cross-section SEM images (Figure 13b) confirm a homogeneous film thickness (ca. 200 nm). Ordered mesopores are arranged throughout the film volume. The mesopores have an ellipsoidal shape.

The geometric mass loading of the film was determined by WDX analysis via StrataGem software. The mass depths of all component elements of a RuPt/OMC film with a

thickness of 565 nm amount to: carbon with $61 \mu\text{g}/\text{cm}^2$, oxygen with $1.5 \mu\text{g}/\text{cm}^2$, platinum with $0.55 \mu\text{g}/\text{cm}^2$ and ruthenium with $1.45 \mu\text{g}/\text{cm}^2$. Accordingly, the weight loadings of Pt and Ru amount to 0.85 wt% and 4.3 wt%, respectively. The loadings of Pt and Ru were additionally confirmed with ICP-OES.

The pore ordering is studied in detail by SAXS (Figure 13c) recorded in transmission mode (90° and 20° in respect to the film surface). The measurement in 90° (left pattern) shows an isotropic ring which can be attributed to the $(1\bar{1}0)$ plane of the pore system with a periodic distance of 13.5 nm. The SAXS pattern recorded in a tilted incidence angle of 20° shows an ellipsoidal diffraction ring. Scattering spots on the ring can be attributed to lattice planes: $(1\bar{1}0)$ with a periodic distance of 13.5 nm and (101) with a periodic distance of 6.1 nm. The regular pore distance perpendicular to the substrate amounts to 3.3 nm. Accordingly, the film contracted about 75% in direction perpendicular to the surface during template removal and carbonization. This anisotropic film shrinkage is a common phenomenon for soft-templated films and described for metal oxide⁷⁸⁻⁸⁰ and carbon^{44, 45, 81} films. During thermal removal of the template micelle the film contracts unidirectionally and the mesopores flatten.

The BET surface area was determined by Kr physisorption. A RuPt/OMC film carbonized at 800°C in H_2/Ar with a film thickness of 565 nm had a surface area of 554 m^2 per m^2 of geometric surface area. The impact of the additional heat treatment for electrochemical activation was also observed. After additional heat treatment at 400°C for 15 min in air the Kr-BET surface area of the same sample amounted to $661 \text{ m}^2/\text{m}^2$. After subsequent reduction in H_2/Ar the BET surface area was $687 \text{ m}^2/\text{m}^2$. The results prove that the film structure is not harmed by the additional thermal treatment. WDX/StrataGem evaluation gives a film density of $1.1 \text{ g}/\text{cm}^3$ of RuPt/OMC. The derived specific BET surface area amounts to $1105 \text{ m}^2/\text{g}$. This high value indicates a strong degree of microporosity besides the surface area from the mesoporous network. The group of Zhao reported surface areas ranging from $670 - 1490 \text{ m}^2/\text{g}$ for similar OMC materials.¹⁴⁶

The electrical conductivity is an important requirement for active electrocatalysts. The electrical conductivity of a RuPt/OMC film with a film thickness of 565 nm amounts to $800 \text{ S}/\text{cm}$. The conductivity exceeds the one of metal containing OMC films reported in literature by one order of magnitude.⁶⁵ Adhesion of a RuPt/OMC film to a glassy carbon substrate was tested by the tape test. No carbon film was peeled off after pulling off the tape indicating good mechanical stability and strong adhesion of the carbon film.

The crystallinity of the metallic components in the film was studied with GI-XRD. Figure 13e shows a weak and broad diffraction signal at $2\theta = 42^\circ$. The most intense reflections of Pt (ccp, PDF 04-0802), cubic Ru (01-088-2333) and hexagonal Ru (06-0663) are indicated. As the indicated reflections are rather proximate to each other the

observed signal cannot be attributed to one single phase. The broadness of the reflection indicates a small crystallite size.

The surface composition of the metallic particles is studied with XPS in the regions of Pt 4f_{7/2} (Figure 13d) and Ru 3d_{3/2} (Figure 13f). The binding energies of Pt can be attributed to metallic Pt (71.7 eV)¹⁴⁷. The deconvoluted spectra in the region of Ru 3d_{3/2} can be attributed to RuO₂ (465.5 eV)¹⁴³ and metallic Ru (462.4 eV)¹⁴³. Integration of the peaks gives a Ru/RuO₂ ratio of 78/22. These results suggest that the particle surface is dominated by metallic species. However, the surface of nanoscopic Ru partially oxidizes at room temperature in air.¹⁴⁵

STEM-EDX was employed to study size and composition of the nanoparticles of RuPt/OMC films. Figure 14 presents results from studies of a film which was carbonized at 800 °C, thermally treated at 400 °C in air and afterwards reduced at 400 °C in H₂/Ar.

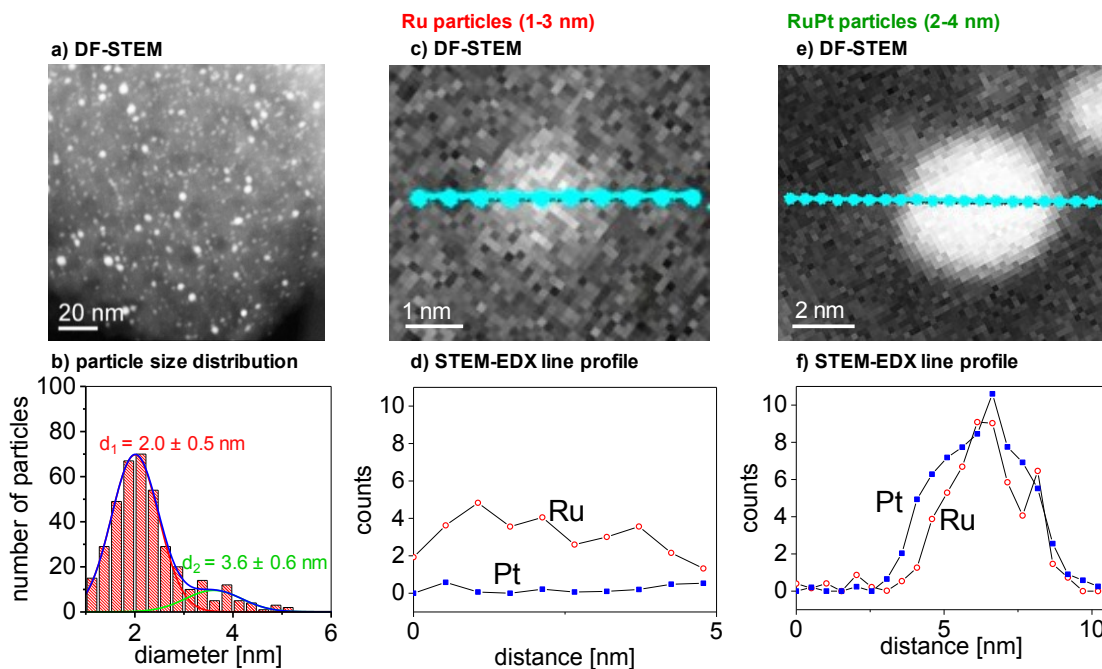


Figure 14. Dark-Field scanning TEM (DF-STEM) micrographs of a F127-templated RuPt/OMC film carbonized at 800 °C in H₂/Ar, additionally treated at 400 °C in air and subsequently reduced at 400 °C in H₂/Ar. a) STEM image displaying small nanoparticles (white dots) inside a mesoporous (dark areas) carbon matrix. b) Histogram of particle size distribution derived from a STEM image a) and two Gaussian fits. The derived mean particle diameters amount to 2.0 ± 0.5 nm and 3.6 ± 0.6 nm. c) DF-STEM image of a typical small Ru particle and EDX (d) line profile extracted from the spectrum along the blue line in c). e) and f) show a DF-STEM micrograph and corresponding EDX line scan of a typical bigger RuPt nanoparticle (2-4 nm).

Figure 14a shows a STEM micrograph in dark-field mode. Nanoparticles as white dots are well-distributed throughout the sample and the mesopores of the carbon matrix (dark areas) are recognizable. The particle size distribution drawn in a histogram (Figure 14b)

shows a bimodal size distribution. From Gaussian fits two mean particle diameter are derived: 2.0 ± 0.5 nm as well as 3.6 ± 0.6 nm.

Figure 14 shows DF-STEM images (c and e) and corresponding EDX line scans (d and f) of both types of particles. The EDX line profile (Figure 14d) of a smaller particle (1-3 nm in diameter, Figure 14c) detects only Ru and no Pt. The particle diameter is similar to the one in Ru/OMC films (see Figure 12d). In contrary, the EDX measurement of a larger particle (2-4 nm in diameter, Figure 14f) detects Ru and Pt. As the intensity profiles of both elements are similar an alloy conformation is likely. Additional STEM images and corresponding EDX line scans of particles with 2-4 nm in diameter are presented in Supplement Figure S10. All particles show an equal distribution of Pt and Ru throughout the particle. The line-scans give no hint for the formation of a core-shell structure. Nevertheless, the lateral resolution of the shown STEM-EDX is limited and a monolayer of one metal species on the external surface of the particle will most likely not be observable. In conclusion, the results prove the successful synthesis of crack-free conductive carbon films with a templated mesoporosity. Small nanoparticles are well-distributed throughout the carbon matrix. STEM-EDX investigations indicate the co-existence of a bimetallic RuPt alloy and monometallic Ru particles. In the following sub-chapter the electrochemical performances of Ru/OMC and RuPt/OMC films in the hydrogen evolution reaction are presented.

Electrochemical performance of mono- and bimetallic Me/OMC films in the HER

Figure 15 presents the electrochemical performances of a Ru/OMC ($0.4 \mu\text{g}_{\text{Ru}}/\text{cm}^2$), Pt/OMC ($1.2 \mu\text{g}_{\text{Pt}}/\text{cm}^2$), a RuPt/OMC ($0.5 \mu\text{g}_{\text{Ru}}/\text{cm}^2$ and $0.2 \mu\text{g}_{\text{Pt}}/\text{cm}^2$) and a Pt/C/Nafion reference catalyst ($1.0 \mu\text{g}_{\text{Pt}}/\text{cm}^2$) in the HER. Figure 15a shows the current responses during the 3rd cycle of cyclic voltammetric (CV) testing, Figure 15b shows the 25th cycle and Figure 15c depicts the Tafel evaluation of the 3rd cycle.

Me/OMC catalysts were exposed to a mild oxidative cleaning procedure prior to electrocatalytic testing. Ru-containing catalysts showed a severe sensitivity towards thermal treatment in air. Accordingly, the time of treatment in air was varied to avoid combustion of film volume. Ru/OMC and RuPt/OMC were additionally exposed to a reducing atmosphere for optimal catalytic activity. The catalysts were treated as follows:

- Ru/OMC: 400 °C for 5 min in air + 400 °C for 15 min in H₂/Ar
- Pt/OMC: 400 °C for 20 min in air
- RuPt/OMC: 400 °C for 15 min in air + 400 °C for 15 min in H₂/Ar

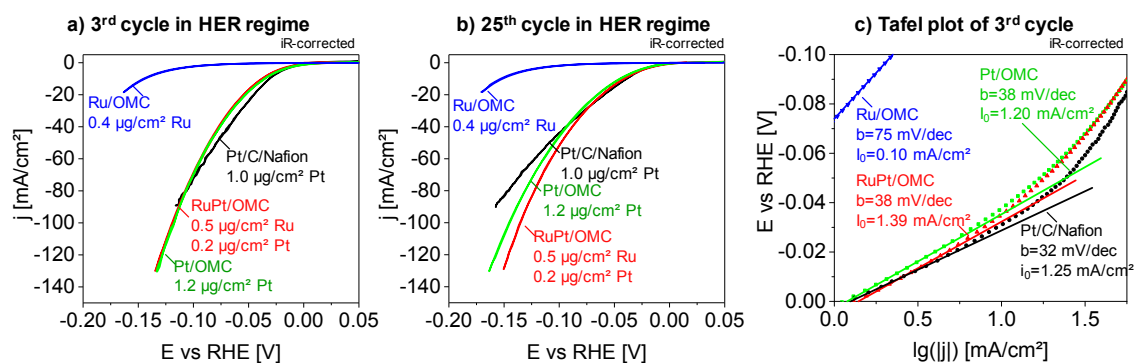


Figure 15. Electrochemical performance of Me-containing catalyst films in 0.5 M sulfuric acid. A Ru/OMC with Ru loading of 0.4 $\mu\text{g}/\text{cm}^2$, a Pt/OMC with 1.2 $\mu\text{g}_{\text{Pt}}/\text{cm}^2$, a RuPt/OMC with 0.5 $\mu\text{g}_{\text{Ru}}/\text{cm}^2$ and 0.2 $\mu\text{g}_{\text{Pt}}/\text{cm}^2$ are compared to a commercial Pt/C/Nafion catalyst with 1.0 $\mu\text{g}_{\text{Pt}}/\text{cm}^2$. a) 3rd cycle and b) 25th cycle of a cyclic voltammetry measurement recorded in the HER regime with 20 mV/s. c) Tafel evaluation of the 3rd cycle (potential E vs. log(current density)). The mass loading of the Me/OMC catalyst films was determined by WDX and StrataGem software.

Figure 15a depicts the current response of the 3rd cycle during CV testing. Ru/OMC shows a rather low activity in the HER. The potential necessary to reach $-10 \text{ mA}/\text{cm}^2$ amounts to -145 mV . Ru needs higher overpotentials in the HER than Pt.¹⁴⁸ By contrast, all Pt-containing catalysts show an excellent HER activity. RuPt/OMC behaves similarly to Pt/OMC and Pt/C/Nafion although the geometric Pt loading of RuPt/OMC is five to six times lower.

After 25 cycles (Figure 15b) all tested catalysts, especially Pt/C/Nafion, show a decrease of the current response of 25 - 40% during cycling. Such decreasing HER performances of Pt-containing catalysts can originate from organic impurities found even in highly purified electrolytes.⁸⁷ RuPt/OMC shows the strongest activity after 25 cycles despite having a considerably lower Pt loading. The bimetallic particles appear to be similarly or more active than Pt nanoparticles. Moreover, the high conductivity and the homogeneous porous morphology of the RuPt/OMC catalyst result in an improved electron and mass transport.

The reduced performance of the Pt/C/Nafion reference catalysts at higher current densities can be attributed to several phenomena. Transport limitations by lack of porosity may play a role as well as insufficient electric contacting. Blocking of pores and active sites by Nafion can also have a detrimental effect.

Tafel plots (Figure 15c) give insights into mechanistic aspects. The potential is plotted as a function of the logarithmic current density. The Tafel slope b can be correlated to the rate-determining step during the HER.¹⁸ b values around 40 mV/dec are attributed to electrochemical formation of molecular hydrogen (Heyrovsky reaction, $\text{MeH}_{\text{ads}} + \text{H}^+ + \text{e}^- \rightleftharpoons \text{Me} + \text{H}_2$), whereas values around 30 mV/dec refer to limitations by chemical H_2 desorption via recombination of adsorbed H atoms (Tafel reaction,

$2 \text{MeH}_{\text{ads}} \rightleftharpoons 2 \text{Me} + \text{H}_2$). Tafel slopes observed for the studied RuPt/OMC and Pt/OMC catalysts amount to 38 mV/dec (Figure 15c). Both catalysts show a similar mechanistic behavior although RuPt/OMC has a significantly lower Pt content. The rate determining step can be assigned to the Heyrovsky reaction. RuPt catalysts from Hunt et al. report Tafel slopes of 31 - 33 mV/dec. In this case the Tafel reaction seems to be the dominant mechanism. Also the shown Pt/C/Nafion catalyst follows the Tafel mechanism with a slope of $b = 32$ mV/dec. This value agrees well with data reported in literature for different Pt/C/Nafion catalysts tested in 0.5 M H_2SO_4 .^{129, 130}

Synthesis conditions, film morphology and information about the activity in the HER of Me/OMC films are summarized in Table 2. A highly active catalyst possesses a low Tafel slope, a high exchange current density j_0 and high mass-based current density. Accordingly, the activity of Me/OMC catalysts can be sorted as follows: $\text{Pd} < \text{Ru} < \text{Pt} < \text{RuPt}$. RuPt/OMC shows the highest mass-based current density with $-24 \text{ mA}/\mu\text{g}_{\text{Ru+Pt}}$. When only Pt is taken into account the current density reaches $-85 \text{ mA}/\mu\text{g}_{\text{Pt}}$.

Recently published commercial RuPt catalysts on Vulcan prepared with Nafion reach mass-based activities of $-0.54 \text{ mA}/\mu\text{g}_{\text{Pt}}$ at -50 mV vs RHE in 0.1 M HClO_4 at $30 \text{ }^\circ\text{C}$.¹⁴⁰ Nanoparticles with RuPt shell on a WC core deposited on Vulcan with Nafion reach $-1.1 \text{ mA}/\mu\text{g}_{\text{Pt}}$ under identical conditions.¹⁴⁰ Commercial Pt/Vulcan/Nafion catalysts with $56 \mu\text{g}_{\text{Pt}}/\text{cm}^2$ tested in 0.5 M H_2SO_4 achieved $-0.43 \text{ mA}/\mu\text{g}_{\text{Pt}}$. RuPt/OMC films show more than 75 times higher mass activities than the Nafion-based reference catalysts in literature.

Table 2. Synthesis conditions, film parameters and information about the initial activity in the HER of F127-templated Me/OMC films. Resorcinol and formaldehyde act as carbon precursors in an acidic polycondensation reaction employing F127 as a structure-directing agent. The formed polymeric compound is dispersed in THF which contains dissolved metal ions. The resulting solution is employed for dip-coating at 25 °C and 30% relative humidity. Films are thermo-polymerized at 100 °C for at least 12 h and subsequently carbonized at the given temperature and atmosphere for 3 h. For enhanced catalytic performance the films are additionally treated under the given conditions. The pore diameter parallel to the surface of the resulting film is listed. The pore diameter perpendicular to the substrate's surface amounts to 2 nm. The average nanoparticle diameter is given. OMC films were tested in 0.5 M H₂SO₄ (degassed with N₂) at room temperature. The initial HER activity in the Tafel regime is summarized. The mass activity of the 3rd cycle at -50 mV is given. Activities of reference catalysts are given in the bottom part of the table.^{131, 140}

Me/OMC	Synthesis conditions					Film morphology		HER activity			
	Mass loading [μg/cm ²]	Precursor	T _{carb} [°C]	Atmosphere	Activation procedure	Pore size [nm]	Particle size [nm]	Tafel slope <i>b</i> [mV/dec]	Exch. current density <i>j</i> ₀ [mA/cm ²]	<i>j</i> _{mass} at -50 mV [mA/μg _{metal}]	
	WDX					SEM	TEM	3 rd cycle CV	3 rd cycle CV	3 rd cycle CV	3 rd cycle CV
OMC	-	-	800	N ₂	-	7	-	-	-	-	-
Pd/OMC	1.2	Pd(acac) ₂	600	N ₂	5 min, 400°C, air + 15 min, 400°C, H ₂ /Ar	7	14.3	94	0.07	-0.2	-
Pt/OMC	1.2	Pt(NO ₃) ₂	700	N ₂	20 min, 400°C, air	9	2.7	38	1.20	-15	-15
Ru/OMC	0.4	Ru(acac) ₃	800	H ₂ / Ar	5 min, 400°C, air + 15 min, 400°C, H ₂ /Ar	9	1.8	75	0.10	-1.3	-
RuPt/OMC	0.5 (Ru) 0.2 (Pt)	Ru(acac) ₃ Pt(NO ₃) ₂	800	H ₂ / Ar	5 min, 400°C, air + 15 min, 400°C, H ₂ /Ar	8	2.0 (Ru) 3.6 (Ru+Pt)	38	1.39	-24	-85
Reference catalysts			HER testing conditions				HER activity				
Author	Mass loading [μg/cm ²]	Catalyst composition		Electrolyte	Temperature [°C]	Tafel slope <i>b</i> [mV/dec]	Exch. current density <i>j</i> ₀ [mA/cm ²]	<i>j</i> _{mass} at -50 mV [mA/μg _{metal}]			
Hunt et al. ¹³	51 (Ru+Pt)	Commercial RuPt/Vulcan/Nafion		0.1 M HClO ₄	30	33.5	1.14	-0.27	-0.54		
Hunt et al. ¹³	20 (Ru+Pt)	RuPt-shell on WC-core /Vulcan/Nafion		0.1 M HClO ₄	30	31.3	1.16	-0.72	-1.1		
Gao et al. ⁵⁷	56	Pt/Vulcan/Nafion		0.5 M H ₂ SO ₄	RT	30	0.71	-0.43	-0.43		
herein	1	Pt/Vulcan/Nafion		0.5 M H ₂ SO ₄	RT	32	1.25	-24	-24		

A comparison of the mass-based HER activity of RuPt/OMC catalysts with Pt/C/Nafion catalysts is shown in Figure 16. The current densities of the 2nd and 25th cycle at an overpotential of -85 mV as a function of the geometric Pt loading of catalysts with varying thicknesses are plotted in Figure 16a and b. Each point represents one measured catalyst of RuPt/OMC and Pt/C/Nafion. In the margin of error the activity correlates linearly with the geometric loading (dashed lines). In the 2nd as well as the 25th cycle RuPt/OMC catalysts reach the same activity as Pt/C/Nafion at four times lower geometric Pt loadings. Accordingly, the RuPt/OMC films clearly outperform the commercial reference catalyst in the fresh as well as in the aged state.

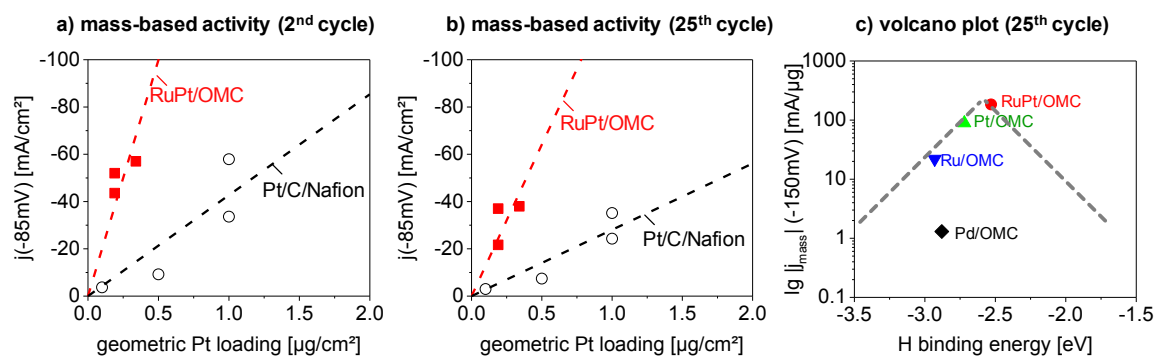


Figure 16. Electrocatalytic performance of catalyst films in 0.5 M sulfuric acid. a, b) Current density at an potential of -85 mV vs. RHE at the 2nd cycle (a) and 25th cycle (b) are plotted against the geometric Pt loading of RuPt/OMC and Pt/C/Nafion reference catalysts. Each point represents one measured catalyst. The mass loading of RuPt/OMC was determined by WDX and StrataGem software. c) Volcano plot: $\lg(\text{mass-based current at } -150 \text{ mV of the } 25^{\text{th}} \text{ cycle})$ of different Me/OMC catalyst systems versus the H binding energies taken from literature.¹⁴⁹ The calculation assumes that Ru and Pt form a near surface alloy. Furthermore, the authors assume that hydrogen covers 0.25 ML of the surface. Mesoporous Ru/OMC catalyst had a loading of Ru: $0.4 \mu\text{g}_{\text{Ru}}/\text{cm}^2$, Pt/OMC: $1.2 \mu\text{g}_{\text{Pt}}/\text{cm}^2$, Pd/OMC: $1.2 \mu\text{g}_{\text{Pd}}/\text{cm}^2$ and RuPt/OMC: $0.5 \mu\text{g}_{\text{Ru}}/\text{cm}^2 + 0.2 \mu\text{g}_{\text{Pt}}/\text{cm}^2$.

The experimental data enable the generation of a Volcano plot for the HER of Me/OMC catalysts. To describe the activity during hydrogen production the mass-based current was chosen as a function of calculated hydrogen binding energy obtained from a fundamental study by Greeley and Mavrikakis.¹⁴⁹ The calculation of the hydrogen binding energy of RuPt assumes that Ru and Pt form a near surface alloy in a ratio of 1:1. Although the real surface composition of the presented RuPt/OMC is not known the trend towards a lower binding energy appears reasonable. As displayed by the dotted volcano line the higher mass-activity of RuPt/OMC gives a hint that the optimal H binding energy for a high HER activity lies at slightly lower H binding energies than the H binding energy of Pt. The slightly lower H binding energy can explain the advanced performance of the bimetallic RuPt/OMC catalyst in the acidic HER.

5.4 Conclusion

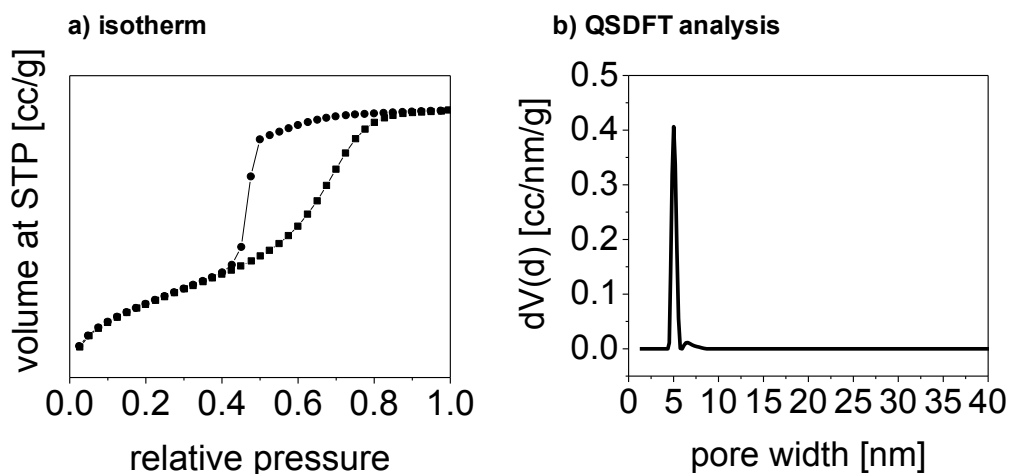
We presented the first bimetallic nanoparticles in ordered mesoporous carbon films obtained from a simple synthesis route. The concept is based on dip-coating of polymeric carbon precursors in the presence of structure-directing polymer micelles as well as ionic metal precursors. The synthesis omits the use of a binding species like Nafion, which could block active sites or pores. The resulting films are homogeneous, highly electrically conductive as well as mechanically, chemically and thermally stable. The films contain two kinds of well-dispersed small nanoparticles: monometallic Ru and bimetallic RuPt. In the hydrogen evolution reaction RuPt/OMC catalyst films show the highest Pt-mass based activity reported in literature so far. The films need four times less Pt than commercially available Pt/C/Nafion catalysts to achieve the same catalytic performance.

Further improvements in the composition can lead to even higher HER performances and lower costs for noble metals. Moreover, the proposed concept enables the synthesis of many kinds of stable bimetallic catalysts, which can be applied in many fields like heterogeneous catalysis.

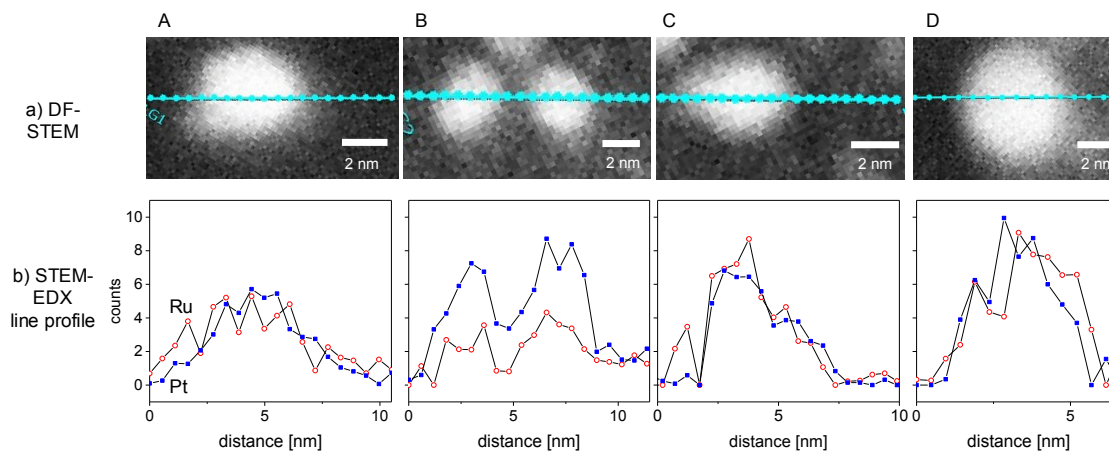
5.5 Acknowledgement

The authors thank ZELMI (TU-Berlin) for providing infrastructure for electron microscopy. We thank Ines Häusler for support with STEM and Andreas Lippitz for XPS measurements. SAXS measurements were conducted on beamline B03 at light source PETRA III at DESY with assistance by Ulla Vainio. We thank Kornelia Weh and Astrid Müller-Klauke for support with ICP-OES analytics. DB, MB and RK acknowledge generous funding from BMBF under contract FKZ 03EK3009. RK particularly appreciates support from the Einstein Stiftung Berlin (EJF-2011 -95).

5.6 Supporting Information



Supplement Figure S9. N_2 physisorption analysis of Ru/OMC powder. The material was carbonized for 3 h in H_2/Ar atmosphere at 800 °C and additionally treated for 400 °C in air and subsequently treated at 400 °C in H_2/Ar . a) full isotherm measured at 77 K, b) QSDFT evaluation of the full isotherm employing an equilibrium transition kernel based on a slit-pore model (pore diameter < 2 nm) and a cylindrical pore model (pore diameter > 2 nm). The calculated specific surface area amounts to 883 m^2/g . The pore diameter amounts to 5 nm.



Supplement Figure S10. Dark-Field scanning TEM (DF-STEM) micrographs and corresponding EDX line profiles of a F127-templated RuPt/OMC film carbonized at 800 °C in H₂/Ar, additionally treated at 400 °C in air and subsequently reduced at 400 °C in H₂/Ar. a) STEM images and b) EDX line profile extracted from the spectrum along the blue lines of four different positions (A-D).

6 Incorporation of preformed Pt colloids into mesoporous carbon films

Submitted to ACS Catalysis

Outstanding HER performance of supported Pt nanoparticles: Incorporation of preformed colloids into mesoporous carbon films

Denis Bernsmeier¹, René Sachse¹, Michael Bernicke¹, Roman Schmack¹, Frieder Kettemann², Peter Strasser¹, Jörg Polte², Ralph Kraehnert¹

¹ Department of Chemistry, Technische Universität Berlin, Straße des 17. Juni 124, 10623 Berlin

² Department of Chemistry, Humboldt-Universität zu Berlin, Brook-Taylor-Str. 2, 12489 Berlin

Abstract

Platinum is the best HER catalyst known so far in acidic environments, but it is also a scarce and expensive resource. Maximizing its performance per metal atom is essential in order to reduce costs. The deposition of small Pt nanoparticles onto electrically conductive, highly accessible and stable carbon supports leads to active catalysts. However, blocking of pores and active sites by Nafion, which acts as a binding species, reduces the catalytic activity. Moreover, inaccessible Pt located in micropores diminishes an efficient exploitation of the noble metal.

We report a new synthesis approach to ordered mesoporous carbon coatings with preformed Pt nanoparticles. The particles are exclusively located inside the mesopores. Furthermore, no Nafion binder is needed. As a consequence, the PtNP/OMC catalyst film outperforms Pt/C catalysts reported in literature particularly at high current densities.

6.1 Introduction

Platinum is a noble metal with unique properties for the activation of small molecules. It therefore plays a central role in many heterogeneously catalyzed reactions as well as electrocatalysis. Pt catalyzes e.g. the oxidation of ammonia¹⁵⁰, glycerol¹⁵¹ or aromatic compounds¹⁵², the hydrogenation of aromatic compounds¹⁵³ and fatty acids¹⁵⁴, the dehydrogenation of tetralin¹⁵⁵ and decalin¹⁵⁶ as well the electrocatalytic hydrogen evolution reaction^{157, 158}.

High price and limited availability of Pt impose efficient utilization of the noble metal. One approach to improve catalytic utilization is the use of Pt in the form of nanoparticles dispersed on support material. The support typically provides stabilization and accessibility to the particles and in some instance also a modified reactivity as well as additional adsorption sites. In the case of hydrogenation and electrocatalytic reactions porous carbon proves to be a sufficiently stable support that provides a high surface area and reasonable accessibility.

The synthesis of Pt/C catalysts is typically performed via wet impregnation of a dissolved ionic Pt-species followed by drying and reduction.^{159, 160} Yet, this approach provides limited control over particle size and distribution.¹⁶¹ Improved size distribution can be obtained via deposition of colloidal nanoparticles on carbon supports.¹⁶² Preformed colloidal Pt nanoparticles are usually deposited onto a porous carbon derived from sources like pyrolyzed organic compounds or charcoal (e.g. Vulcan XC72)^{163, 164} or onto carbon nanotubes.¹⁵⁹

For their application in electrocatalysis catalyst powders need to be processed to electrode coatings. This is done by casting an ink onto conductive electrode substrates. The ink typically consists of a fine-grained Pt/C catalyst powder, a binder species like Nafion (a fluoropolymer copolymer) and solvents.¹⁶⁵ A significant drawback of this approach is the partial blocking of pores and active sites by the binder, which can result in a decreased catalytic activity.³²⁻³⁴ Moreover, the reproducible casting of homogeneous ink-based films is rather challenging.^{35, 166} Inhomogeneities result in locally insufficient electrical conductivity and decreased electrocatalytic performance.

OMC films possess all typical properties desired in a catalyst support, i.e. high surface area, control over pore size and pore connectivity^{44, 50, 52}, chemical stability⁴⁸, electrical conductivity¹¹² and strong film adhesion to a variety of substrates¹⁶⁷. Typical synthesis procedures for OMC films start by dispersion and pre-polymerization of low-molecular weight carbon precursors (e.g. resins made from phenol¹⁴², resorcinol⁴⁶ or phloroglucinol⁵² and formaldehyde) in presence of pore templates, e.g. micelles of amphiphilic block copolymers. Film casting and structure formation typically proceeds via dip-coating⁴⁸ or spin-coating⁵⁰. Subsequent thermal treatments densify the precursor polymer, decompose

the template molecules and transform the remaining porous structure into a partially graphitized carbon.

Voigt et al. recently demonstrated the synthesis of OMC films modified with either cobalt oxide or vanadium oxide.^{65, 66} The incorporation of the oxide particles into OMC films succeeded via co-deposition of the polymer precursor, ionic metal precursors and subsequent thermal processing. However, the co-deposition of metal and polymer precursors followed by thermal or chemical reduction during processing of the carbon can have detrimental effects on the activity. The formation of small particles inside micropores of the carbon can lead to transport limitations inside the catalyst. Another aspect is that a fraction of the employed precursor can remain enclosed in the carbon walls, i.e. inaccessible to the educts. In this context the introduction of preformed nanoparticles into the synthesis of OMC films is a promising alternative as the nanoparticles will be located inside the mesopores ensuring their accessibility.

The present contribution reports for the first time the synthesis of mesoporous PtNP/OMC catalyst films employing colloidal size-controlled Pt nanoparticles. Pt-NPs in THF are mixed with a polymer resin consisting of resorcinol-formaldehyde and a structure-directing agent (Pluronic F127). The colloid in organic solvent, i.e. THF, proves to be vital for a successful film preparation as it is compatible with the micelle-structured polymer.

The deduced procedure for colloid synthesis is based on recipes published by Bönemann and co-workers^{72, 73, 168} as briefly summarized in Scheme 9. First, Tetraoctylammoniumtriethylhydroborate ($\text{N}(\text{octyl})_4\text{BEt}_3\text{H}$) is synthesized in the absence of oxygen and purified. It is added to PtCl_2 in THF and serves as reducing and stabilizing agent (see Experimental for details).^{75, 168}

As illustrated in Scheme 10 a structure-directing block copolymer (Pluronic F127) and resorcinol are dissolved in ethanol. HCl and formaldehyde solution are added to initiate a polycondensation reaction. The formed polymer resin is separated, washed, freeze-dried and then redissolved in THF. The PtNP colloid is added to this mixture and the resulting suspension employed for film casting via dip-coating. The derived films are cross-linked and stabilized at 100 °C in air. Subsequently, the films are carbonized under H_2/Ar flow at 700 °C resulting in template removal and formation of a highly conductive and partially graphitized mesoporous films. A brief treatment in air (20 min, 300 °C) removes residual carbon species from the Pt particles and produces catalyst films that are tested in the electrocatalytic hydrogen evolution reaction (HER).

The following sections describe the properties of the employed PtNP colloid. Thereafter morphology, surface area and phase composition of the obtained carbonized PtNP/OMC films are described. Moreover, HER activity and kinetic parameters of the PtNP/OMC catalysts are reported and compared to commercial Pt/C catalyst based on Nafion inks.

6.2 Experimental

Chemicals

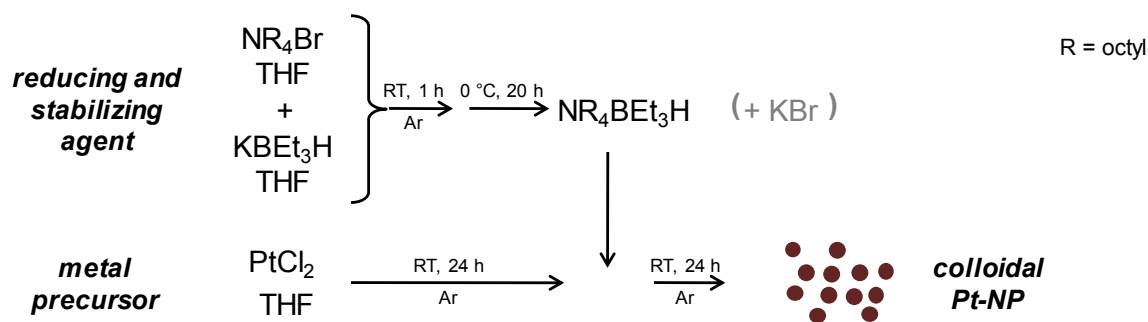
MilliQ water was employed for all synthesis procedures. Ethanol (EtOH, >99.9%, absolute) was obtained from VWR and tetrahydrofuran (THF, >99.9%, absolute) from Roth. For the colloid synthesis PtCl₂ (99.99+%) from Alfa Aesar as well as tetraoctylammonium bromide (TOAB, N(C₈H₁₇)₄Br, 98%) and potassium triethylborohydride solution (KB(C₂H₅)₃H; KBET₃H, 1.0 M in THF) from Sigma Aldrich were used. Resorcinol and formaldehyde (37 wt% in water), Pluronic F127 (PEO₁₀₆-*b*-PPO₇₀-*b*-PEO₁₀₆, M_w = 12 600 g/mol), 5%-Nafion solution and isopropanol were purchased from Sigma-Aldrich. 3 M hydrochloric acid (HCl) was prepared from 12 M HCl (Alfa Aesar). All chemicals were used without further purification. Pt on Vulcan (BASF, XC 72R (Cat. No. 181, 10 wt% Pt) was employed as a reference catalyst.

Pretreatment of substrates

Catalyst films were synthesized on different substrates, i.e. single side polished and double side polished Si wafer with (100)-orientation (University Wafers), glassy carbon "Sigradur G" (HTW) and SiO₂ glass microscopy slides (Science Services). Si wafer substrates were cleaned with a tissue containing ethanol and calcined in air (2 h, 600 °C) prior to film deposition. Glassy carbon (GC) substrates were polished with 0.05 μm alumina dispersion and immersed and ultrasonicated two times in water and ethanol and then rinsed with ethanol. SiO₂ glass substrates for conductivity measurements were ultrasonicated in ethanol and then wiped with a tissue containing ethanol prior to coating.

Synthesis of PtNP colloid

Scheme 9 illustrates schematically the synthesis of PtNP colloids as described by Bönemann.¹⁶⁸ The reducing agent Tetraoctylammoniumtriethylhydroborate (N(C₈H₁₇)₄BH(C₂H₅)₃) was synthesized under Ar atmosphere (O₂ < 1 ppm; H₂O < 1 ppm) in a glovebox. 549 mg of TOAB was initially dissolved in 1.2 ml THF. During stirring 1.0 ml of KBET₃H solution was added and a white precipitation formed. The mixture was stirred for 1 h and kept tightly sealed in a freezer (ca. 0 °C) for 20 hours. Thereafter the mixture was brought to room temperature in the glovebox and a white precipitate of KBr was removed by filtration (syringe filter, 5.0 μm, PTFE) and washed with 0.55 ml THF. The filtrate and washing solution was filtrated again (syringe filter, 0.2 μm, Nylon) and a colorless solution was obtained.

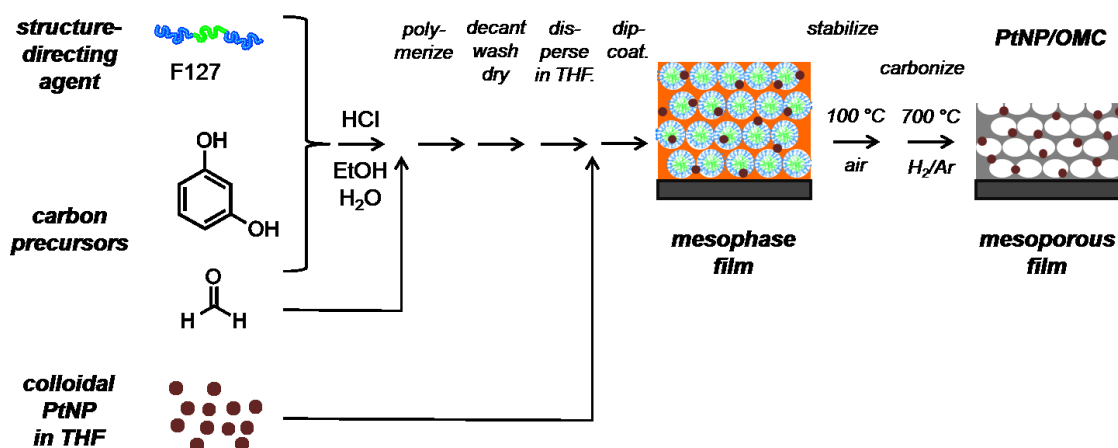


Scheme 9. Illustration of the synthesis approach to colloidal Pt nanoparticle in THF.¹⁶⁸ The stabilizing and reducing agent N(octyl)₄BEt₃H is formed by mixing TOAB in THF with KBet₃H in THF at room temperature in Ar atmosphere. After 20 hours at circa 0 °C the KBr is removed by filtration. The colloidal Pt is synthesized by dispersing PtCl₂ in THF and addition of a freshly prepared solution of N(octyl)₄BEt₃H in THF. After mixing for 24 h at room temperature the Pt colloid is obtained.

The PtNP colloid synthesis was performed under Ar atmosphere in a glovebox. 52.7 mg PtCl₂ were dispersed in 5 ml of THF and stirred for 24 h at room temperature. The precursor dissolved only partially and a brown precipitate remained visible. 1 ml of freshly prepared N(octyl)₄BEt₃H/THF was then added, upon which the PtCl₂/THF mixture turned black immediately. The mixture was stirred for another 24 hours during which nearly all precipitate was dissolved. After precipitate removal (filtration, syringe filter 0.2 μm, Nylon) a homogeneous black colloidal solution was obtained.

Synthesis of polymer precursor and PtNP/OMC film

Scheme 10 illustrates the synthesis of the polymer precursor and PtNP/OMC film. Initially 1.1 g of resorcinol and 300 mg of the pore template Pluronic F127 were dissolved in 4.5 mL of EtOH in a centrifuge tube until a clear solution was obtained. Then 4.5 mL of 3 M HCl were added and the tube was shaken for 30 minutes. Thereafter 1.2 ml of formaldehyde solution (37% in water) were added with continued shaking. Circa four minutes later the solution became turbid. Ten minutes after addition of formaldehyde a white precipitate was separated via centrifugation (7500 rpm, 10 min) and the remaining solution discarded. The white precipitate was washed with water and centrifuged again two times. The obtained polymer/template phase was subsequently freeze dried for 12 h to remove all volatile components, resulting in 836 mg of resin, which corresponds to ca. 31% of the employed components (resorcinol, formaldehyde, F127).



Scheme 10. Illustration of the synthesis approach employed to mesoporous PtNP/OMC catalyst films. The structure-directing triblock copolymer F127 (PEO-PPO-PEO) and resorcinol are dissolved in ethanol. After addition of hydrochloric acid, formaldehyde solution is added to start the polycondensation reaction. The derived polymeric resin is separated by centrifuging, washed and freeze-dried. The polymeric compound is redissolved in THF and the Pt colloid added. Under controlled conditions a substrate is dipped into the mixture to obtain a homogeneous mesophasic film. After thermal treatment at 100 °C in air and a subsequent carbonization under H₂/Ar atmosphere at 700 °C for 3 h a mesoporous PtNP/OMC film is obtained.

For the PtNP/OMC film synthesis the freeze-dried polymer precursor was dissolved in 3.3 ml of THF under Ar atmosphere and shaken for 10 min. 1.7 ml of PtNP colloid in THF were added. The mixture was shaken for another 10 min. The resulting homogeneous black suspension was employed for film casting. Catalyst films were deposited via dip-coating at room temperature in Ar atmosphere inside a glove-box. The withdrawal speed was varied (60, 150, 300 mm/min) to obtain films of different thicknesses. The coated substrates were transferred to a drying furnace and then treated for 12 h at 100 °C in air for film stabilization. The stabilized films were transferred into a tube furnace and heated with 3 K/min in H₂/Ar (4 vol% H₂) flow to 700 °C, holding this temperature for 3 h, and subsequent naturally cooling down to room temperature. Films were additionally treated in a tube furnace for 20 min at 300 °C in air flow to remove carbon residues from the PtNPs surface prior to electrocatalysis.

Synthesis of catalytic reference coatings Pt-Vulcan/Nafion

Coatings of the reference catalyst based on Nafion and commercial Pt/Vulcan were prepared according to established routes reported in literature with 1 µg/cm² geometric Pt loading.^{116, 117} Typically, 5 mg of Pt/Vulcan powder (10 wt% Pt) were dispersed in 3.98 ml of water. 20 µl of Nafion solution (5%) was added as well as 1 ml of isopropanol and the mixture sonicated for 15 min (Branson Sonifier, 6 W output power). The resulting ink was immediately drop-casted onto cleaned GC substrates and subsequently dried at 60 °C in air.

Physico-chemical characterization

SEM images were collected on a JEOL 7401F at 10 kV. Image J program, version 1.39u (<http://rsbweb.nih.gov/ij/>), was employed to determine pore diameters, film thicknesses, sizes of Pt particles and to obtain fast Fourier transformations (FFT) of images. TEM images were recorded on a FEI Tecnai G² 20 S-TWIN operated at 200 kV. Colloidal PtNP or fragments of scraped off film segments were deposited on carbon-coated copper grids. To determine the amount of Pt contained in the Pt/OMC films, the mass depth was calculated using the STRATAGem film analysis software (v 4.3) based on wavelength dispersive X-ray (WDX) spectra analyzed with a JEOL JXA-8530F electron microprobe at 7 and at 10 kV.

SAXS analysis of colloidal PtNP in THF was performed using a SAXSess instrument (Anton Paar GmbH). Obtained scattering curves were analyzed with the assumptions of spherical shape, homogeneous electron density and a Schulz–Zimm size distribution.

SAXS analysis of PtNP/OMC films was measured at BESSY mySpot beamline with 12.518 keV and sample-to-detector distance of 753.671 mm. A marCCD detector with 3072 x 3072 px was employed.

XRD data were recorded on a Bruker D8 Advance (Cu K_α radiation) with grazing incident beam (1°). X-ray diffraction reflections were assigned using the Powder Diffraction Files database. The obtained diffraction patterns were further analyzed using Rietveld refinement and the software Topas V4.2 (Bruker-AXS). Profiles of the reflections were fitted using the Fundamental Parameter approach of the software. The background was fitted using 4th order Chebyshev polynomial. Scale factor, lattice parameters of the phases and broadening of the reflections by Gaussian and Lorentzian contributions were refined. Zero point errors were taken into account. The coherence length of the crystallites was estimated using Scherrer equation and the volume-weighted full width at half maximum (FWHM). The determined FWHM was corrected for contributions from instrumental broadening.

The electrical conductivity of PtNP/OMC coatings on SiO₂ substrates was measured with a Keithley Model 6517B Electrometer employing an 8x8 pin probe head with an alternating polarity sequence of the pins.

Pt loading values of PtNP/OMC films were obtained from WDX/StrataGem analyzes and confirmed by ICP-OES analyzes. For ICP-OES analysis PtNP/OMC films coated on both sides of double-side polished Si wafers were digested for 40 min at 180 °C and 18 bar in a mixture of aqua regia and concentrated sulphuric acid with a microwave instrument (Discover SP-D from CEM) and the obtained solution analyzed with a Varian 715-ES. A four point calibration with the same acid mixture was employed.

The pore system of PtNP/OMC was analyzed via N₂ physisorption isotherms recorded at 77 K on powder samples using a Quantachrome Autosorb-iQ. The samples were degassed in vacuum at 150 °C for 2 h prior to physisorption analysis. The surface area and pore size was evaluated with a NLDFT equilibrium Kernel and a model assuming cylindrical pores. The surface area of PtNP/OMC films coated on both sides of double side polished Si wafers was measured with Kr physisorption at 77 K using an Autosorb-iQ (Quantachrome). Prior to adsorption measurement the samples were degassed for 2 h at 150 °C in vacuum. The surface area was calculated via the Brunauer-Emmett-Teller (BET) method.

Electrocatalytic testing in the hydrogen evolution reaction

All electrocatalytic testing was performed using a three-electrode disc setup (Pine MSR rotator, BioLogic SP-200 potentiostat) employing a reversible hydrogen electrode "RHE" (Gaskatel, HydroFlex) as a reference and Pt gauze (Chempur, 1024 mesh cm⁻², 0.06 mm wire diameter, 99.9%) as a counter electrode, and a catalyst coated GC disk as a working electrode. All potentials in this work are referenced to the RHE. The working electrode was prepared by cutting 5 mm circular discs from the larger PtNP/OMC coated GC substrates and mounting them on a rotating disk shaft. During testing the disc was rotated at 2000 rpm in the supporting electrolyte (0.5 M H₂SO₄, Fixanal, Fluka Analytical). Prior to catalytic testing the electrolyte solution was purged for at least 30 minutes with nitrogen. Hydrogen evolution performance was studied by cyclic voltammetry (CV) in a potential window of 50 to -250 mV vs. RHE with a scan rate of 20 mV s⁻¹. Impedance spectra were recorded before CV testing to correct for ohmic losses.

6.3 Results and discussion

Platinum nanoparticles were synthesized as a colloidal solution in THF in analogy to the synthesis route by Bönemann et al.^{72, 73, 168} The first part describes the crystallinity and the size distribution of the PtNP. In the following part film and pore morphology of the carbonized PtNP/OMC film is discussed. Moreover, crystallinity and size distribution of the PtNP inside the carbon matrix are assessed by TEM and XRD. Finally, the electrochemical performance of the PtNP/OMC films in the acidic hydrogen evolution reaction (HER) is studied and compared to the performance of a commercial reference catalyst.

Crystallinity and particle size distribution of colloidal PtNP in THF

Colloidal PtNP in THF were synthesized as explained in Scheme 9 by dispersion of PtCl_2 in THF and reduction with $\text{N}(\text{octyl})_4\text{BEt}_3\text{H}$ at room temperature. Figure 17 presents the physico-chemical characterization of the colloidal PtNP.

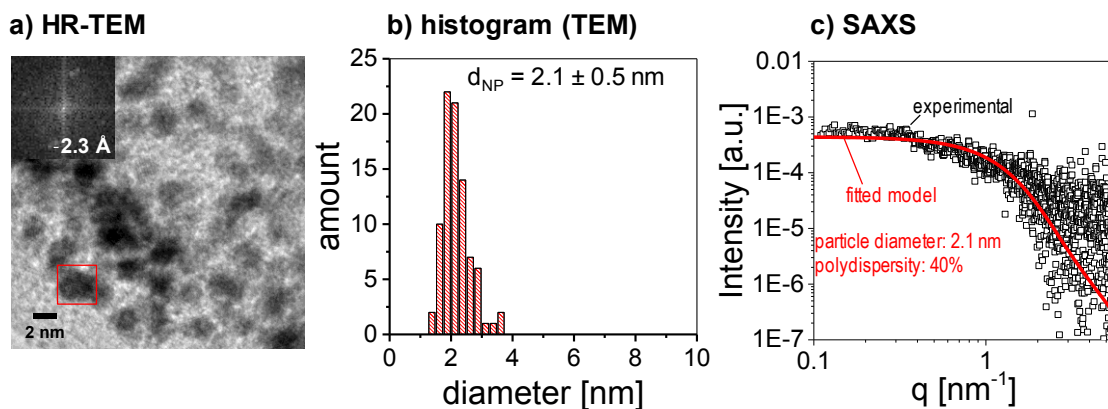


Figure 17. Colloidal platinum nanoparticles synthesized in THF. PtCl_2 is reduced and stabilized by $\text{N}(\text{octyl})_4\text{BEt}_3\text{H}$ in THF at room temperature. a) HR-TEM image of colloidal nanoparticles deposited on a carbon-coated copper TEM grid with a corresponding FFT image of one marked particle. The indicated distance of 2.3 Å can be attributed to the (111) lattice plane of cubic Pt (PDF: 04-0802). b) Histogram of measured particle diameters: The average diameter from 86 measurements amounts to $2.1 \pm 0.5 \text{ nm}$. c) SAXS scattering curves and mathematical fits of colloidal stabilized PtNP (65 mg/L) in THF. The intensity is plotted against the scattering vector q . A spherical shape, a homogeneous electron density and a Schulz–Zimm size distribution are assumed. The particle mean diameter amounts to 2.1 nm

A HR-TEM image (Figure 17a) of colloidal Pt-NP shows spherical nanoparticles. Lattice fringes suggest a high crystallinity of the particles. The FFT of one marked particle gives a regular distance of the fringes of 2.3 Å, which corresponds to (111) lattice planes of cubic Pt (04-0802, $\text{Fm}\bar{3}\text{m}$). Figure 17b shows a histogram of 86 measured particle diameters determined from TEM micrographs. The particle size distribution is narrow and the average particle diameter amounts to $2.1 \pm 0.5 \text{ nm}$.

In order to confirm the particle diameter present in colloidal solution and to evaluate whether particle aggregates are formed in solution SAXS measurements were performed. Figure 17c shows the scattering curve of colloidal PtNP (65 mg/L) and the corresponding fit. The fit indicates a particle diameter of 2.1 nm and a polydispersity of 40%. The diameter of 2.1 nm was confirmed by SAXS and no significant formation of particle aggregates was observed. The synthesis route leads to a well-defined colloid of crystalline Pt in THF. The following section will evaluate the morphology of the carbonized PtNP/OMC film.

Morphology of the carbonized PtNP/OMC film

The synthesis procedure of the PtNP/OMC films is illustrated in Scheme 10. After carbonization at 700 °C PtNP/OMC films are black and homogeneous. Characterization with SEM and physisorption of the pore morphology is shown in Figure 18.

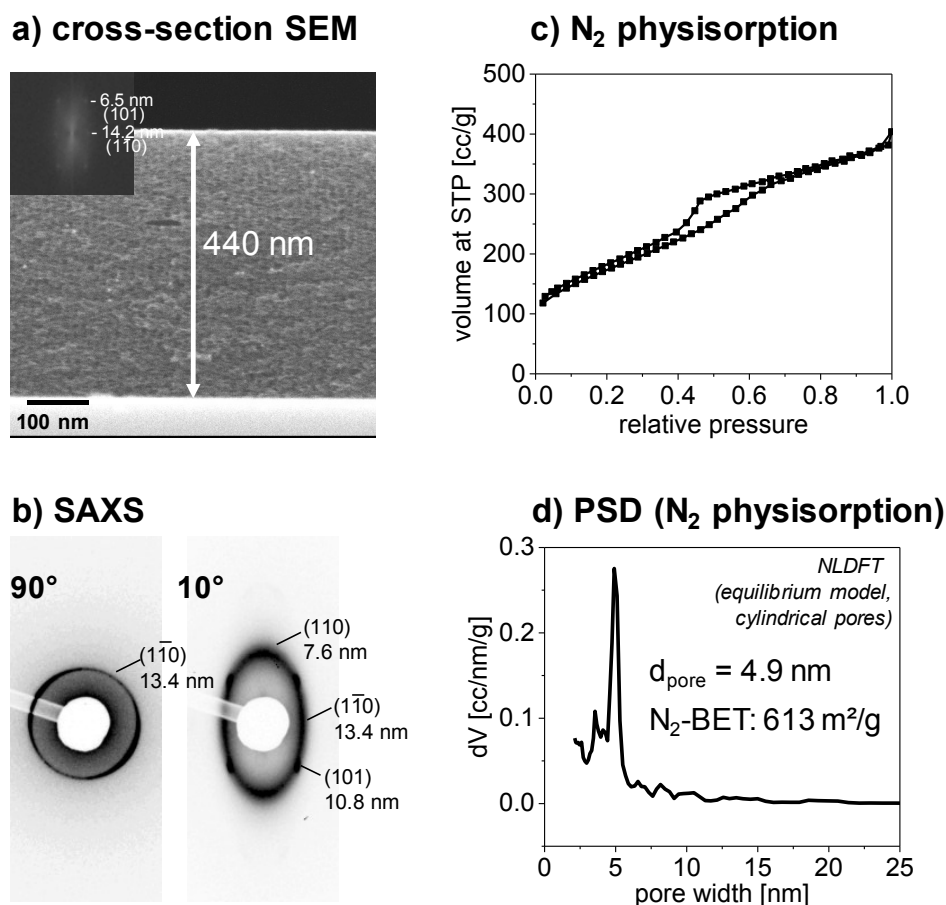


Figure 18. SEM and SAXS characterization of a F127-templated PtNP/OMC film with 2.3 wt% of Pt, carbonized at 700 °C in H₂/Ar and subsequently treated at 300 °C in air: a) cross-section SEM image and FFT image (inset) with indicated values of regular pore distances. b) 2D-SAXS pattern recorded in transmission mode with an incident angle of 90° and 10°. c) isotherm of a N₂ physisorption measurement at 77 K of corresponding powder sample. d) NLDFT evaluation of the isotherm (c) with assumption of a cylindrical pore configuration. The calculated specific surface area amounts to 613 m²/g.

A cross-section SEM image in Figure 18a shows a crack-free and homogeneous porous film with a film diameter of 440 nm. Throughout the film volume small ellipsoidal mesopores are arranged. The pore diameter from SEM is 8 nm parallel and 4 nm normal to the surface plane. A FFT of the cross-section SEM image (inset in Figure 18a) shows spots arranged on a ring with an elliptical shape. The regular distances of the pores derived from FFT can be attributed to a pore system in body-centred cubic (bcc) configuration with a contraction of ca. 75%. The ellipsoidal shape of pores in a soft-

templated film is a well-known phenomenon observed for oxide (TiO_2 ⁷⁸, IrO_2 ⁶⁸, NiO ¹⁰²) and carbon^{44, 45} films. During thermal removal of the polymer micelle the film is contracted in direction of the film normal and the pores flatten.

Small angle X-ray scattering (SAXS) analysis in Figure 18b of PtNP/OMC films proves a high degree of pore ordering. The pattern recorded with an incident angle of 90° in respect to the surface plane shows an isotropic ring which can be attributed to a d -spacing value of 13.4 nm for the $(1\bar{1}0)$ plane of the mesopore lattice. The SAXS measurement in a tilted angle (10°) shows diffraction spots on an ellipsoidal ring that indicates. The scattering spots can be assigned to the (101) and $(1\bar{1}0)$ lattice planes of a contracted cubic pore system.¹²² The d -spacing of the $(1\bar{1}0)$ plane amounts to 7.6 nm, indicating a film contraction of ca. 50% during template removal and carbonization.

Pore size distribution and surface area are studied with N_2 physisorption analysis of a PtNP/OMC powder sample which was thermally treated in the same way. The hysteresis loop of the isotherm (Figure 18c) can be attributed to the presence of interconnected mesopores. The steep increase at low relative pressures is caused by a high extent of microporosity. A NLDFT evaluation shown in Figure 18d indicates a narrow pore size distribution of 4.9 nm. About 85% of the total pore volume of $0.57 \text{ cm}^3/\text{g}$ can be attributed to mesopores, about 15% to micropores. The total accessible surface area derived from NLDFT analysis of the physisorption data amounts to $660 \text{ m}^2/\text{g}$. The surface area derived from BET evaluation of the N_2 measurement amounts to $613 \text{ m}^2/\text{g}$. BET surface area of a Kr physisorption measurement of equally treated PtNP/OMC films provides $685 \text{ m}^2/\text{g}$.

Hence, the PtNP/OMC films exhibit a well ordered system of ellipsoidal mesopores. The mesopores are interconnected and ordered in a contracted bcc configuration with a high surface area and pore connectivity. The presence of preformed PtNP during the film deposition, mesophase formation, thermal treatment and carbonization does not have a degrading influence on the formation of mesoporous structure.

The geometric mass loading of Pt in the film was determined with WDX/StrataGem and independently confirmed via ICP-OES. A film with a thickness of 440 nm has a geometric Pt loading of $1.6 \mu\text{g}_{\text{Pt}}/\text{cm}^2$ from WDX/StrataGem ($1.6 \mu\text{g}_{\text{Pt}}/\text{cm}^2$ from ICP-OES). The volumetric Pt loading derived from these measurements amounts to 2.3 wt%. The electrical conductivity of the PtNP/OMC film amounts to 30 S/cm. This value is in good agreement with values reported for e.g. OMC films containing cobalt oxide or vanadia ($20 - 40 \text{ S/cm}$ after carbonization at 800°C).⁶⁵

To achieve high activities in the electro-catalytic performance of the PtNP/OMC films a preservation of the small PtNP size is required. To prevent intensive sintering the particles need to be confined inside the mesoporous system. In Figure 19 the particle morphology

of the PtNP/OMC film after carbonization at 700 °C in H₂/Ar and additional heat treatment at 300 °C in air is characterized by TEM and XRD.

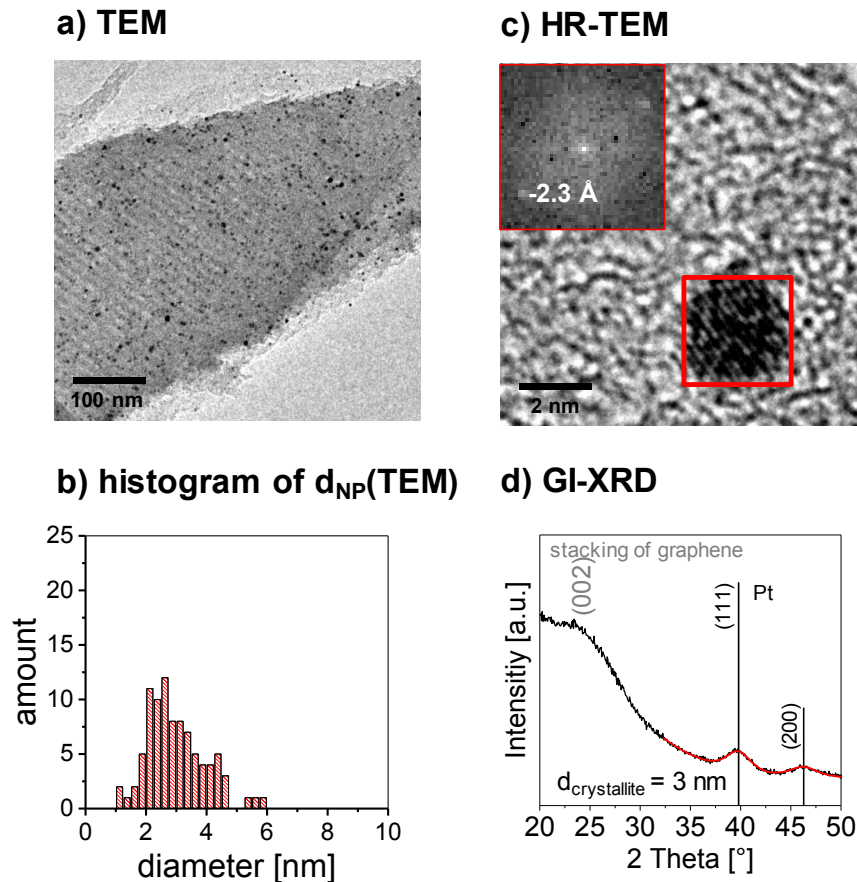


Figure 19. TEM and XRD characterization of a F127-templated PtNP/OMC film with 2.3 wt% Pt, carbonized at 700 °C in H₂/Ar and subsequently treated at 300 °C in air: a) TEM micrographs in bright field mode. b) Histogram of measured particle diameters: mean diameter of 90 particles amounts to 3.0 ± 1.0 nm. c) HR-TEM image of a particle with corresponding FFT inset. The indicated distance of 2.3 Å can be attributed to the (111) lattice plane of cubic Pt (PDF: 04-0802). d) Gracing incidence (1°) XRD characterization: The reflections can be attributed to cubic Pt (04-0802), the broad reflection at 24° can be attributed to a stacking of graphene (002) of the OMC film. A fit from Rietveld refinement is shown in red. The crystallite size estimated via Rietveld amounts to 3.0 ± 0.7 nm.

In a TEM micrograph (Figure 19a) of a scraped off film sample the well-ordered pore structure and abundant presence of mesopores inside the film volume is confirmed. Moreover, small dark spots are distributed throughout the sample. They can be attributed to well-dispersed Pt particles. A histogram of nanoparticle diameters is presented in Figure 19b. The average particle diameter amounts to 3.0 ± 1.0 nm and is slightly higher and more polydisperse than the particle diameter of the initial colloid (2.1 ± 0.5 nm, compare Figure 17b). The size increase can be attributed to some sintering during the carbonization procedure. Nevertheless, the increase is not significant. Confinement effects of the mesopores are likely to retain the small particle size during the carbonization step. Schüth et al. observed nanoparticle confinement of Pt particles inside hollow

graphite spheres⁷⁰ and of AuPt particles inside porous carbon shells¹²⁵ at high temperatures (900-1000 °C).

Lattice fringes visible in a high-resolution (HR)-TEM micrograph (Figure 19c) indicate the high crystallinity of the particles. The lattice planes of the particle (FFT inset in Figure 19c) have a distance of 2.3 Å and correspond to (111) lattice planes of cubic Pt (04-0802, Fm $\bar{3}$ m).

In GI-XRD (Figure 19d) measurements two broad reflections at 39.8° and 46.2° appear which can be attributed to the (111) and (200) lattice planes of metallic platinum (PDF 04-0802). Additionally, a broad reflection at 24° can be assigned to the (002) lattice plane of disordered small graphene stacks.⁷⁶ The Pt crystallite size estimated via Rietveld refinement (Figure 19d) (3.0 ± 0.7 nm) is in good agreement with the particle size obtained from TEM analysis (3.0 ± 1.0 nm).

The results suggest that the incorporation of preformed nanoparticles into the synthesis of conductive OMC films was successful. Pt particles are retained homogeneously dispersed throughout the film volume. Presumably, confinement effects of the synthesized mesopores have a major contribution that no larger particle aggregates form during the harsh conditions of the carbonization. A very sinter-resistant Pt-containing material is obtained. As a consequence, the well-structured conductive PtNP/OMC catalyst film should show a high activity in the hydrogen evolution reaction.

Performance in the HER and comparison to commercial reference catalyst

To study the catalytic performance of F127-templated PtNP/OMC (2.6 wt% Pt) in the HER a series of five catalysts with varying film thickness was tested. The film thickness and thus geometric Pt loading was adjusted by changing the withdrawal speed during the dip-coating procedure: 0.8, 1.1, 1.6 $\mu\text{g}_{\text{Pt}}/\text{cm}^2$. After carbonization for 3 h at 700 °C in H₂/Ar each PtNP/OMC catalyst was exposed to a mild oxidative cleaning procedure (20 min at 300 °C in air) prior to HER testing. Moreover, Pt/Vulcan catalyst films deposited from a Nafion-based ink were tested under identical conditions as references.

Figure 20 shows (a) the current responses of the 2nd cycle of a cyclic voltammetric testing and the geometric current density as a function of the geometric loading of the 2nd cycle (b) and the 50th cycle (c) at a potential of -75 mV vs. RHE of PtNP/OMC catalyst films and Pt/Vulcan/Nafion reference catalysts.

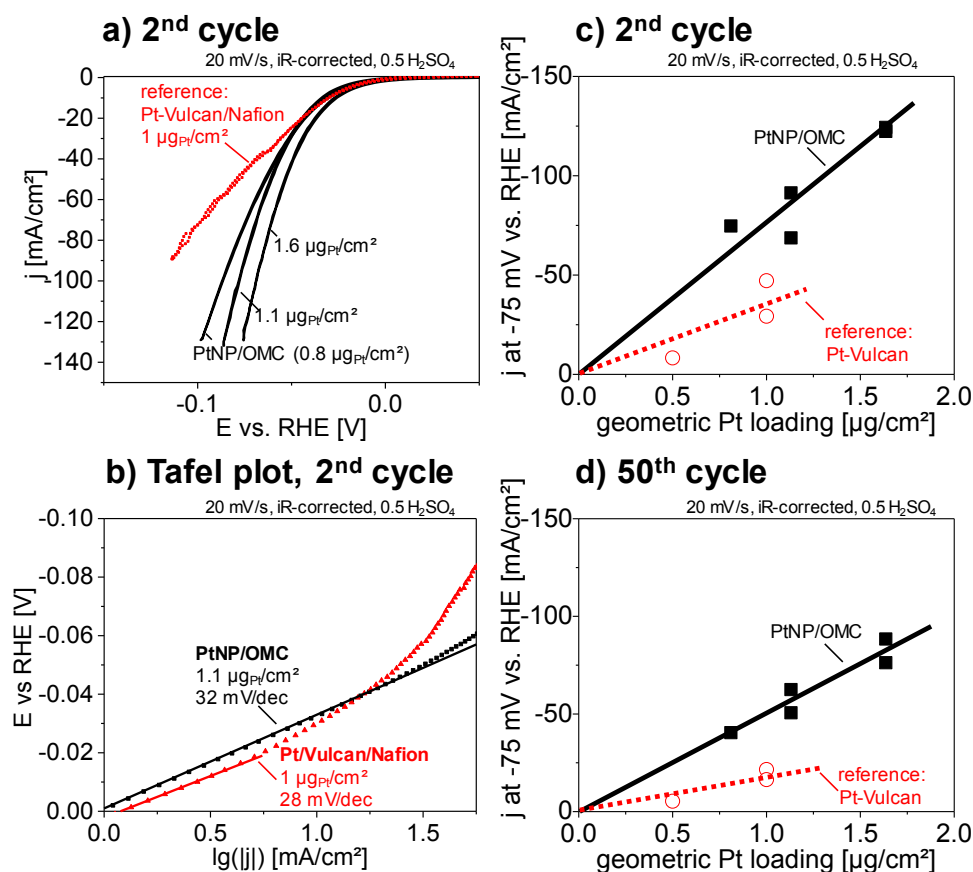


Figure 20. Electrochemical performance of F127-templated PtNP/OMC catalyst films with 2.3 wt% Pt carbonized for 3 h at 700 °C in H₂/Ar and subsequently treated at 300 °C in air. Cyclic voltammograms were recorded in the HER regime with 20 mV/s in 0.5 M sulfuric acid. a) 2nd cycle of PtNP/OMC films with different film thicknesses (geometric Pt-loading between 0.8 - 1.6 µg_{Pt}/cm²) in comparison to Pt/Vulcan reference catalysts. b) Tafel evaluation of the 2nd cycle (potential *E* vs. log(current density)). c, d) Current density responses of the 2nd cycle (c) and 50th cycle (d) reached at an overpotential of -75 mV of PtNP/OMC and Pt/Vulcan films as a function of the geometric Pt loading. Each point represents a measured catalyst.

The 2nd cycle of the cyclic voltammogram (Figure 20a) proves that all measured PtNP/OMC catalysts show a high activity in the HER. At higher current densities ($|j| > 25 \text{ mA/cm}^2$) the current density scales with the geometric Pt loading. In the low-current regime Pt/Vulcan/Nafion (1 µg_{Pt}/cm²) shows a similar current response as the PtNP/OMC catalysts but needs a significantly higher overpotential to reach higher currents.

Mechanistic insights can be obtained by Tafel evaluation of the current response (Figure 20b) for the 2nd cycle by plotting the potential *E* vs. log of the current density. According to literature the Tafel slope *b* is indicative for the rate-determining step of the HER.¹²

Values around 30 mV/dec are typically attributed to rate limitation by recombination of adsorbed H atoms (so-called Tafel reaction, $2 \text{ MeH}_{\text{ads}} \rightleftharpoons 2 \text{ Me} + \text{H}_2$). Tafel slopes

observed for the studied PtNP/OMC catalysts amount to 32 mV/dec ($1.1 \mu\text{g}_{\text{Pt}}/\text{cm}^2$) and 28 mV/dec for Pt/Vulcan/Nafion. This value agrees well with data reported in literature for different Pt/C/Nafion catalysts tested in 0.5 M H_2SO_4 , i.e. 29 to 34 mV/dec.^{108, 128-130}

A reasonable comparison between the two types of catalysts is gained by plotting the current responses versus the geometric Pt loading for 2nd (Figure 20c) and 50th cycle (Figure 20d). At a potential of -75 mV the PtNP/OMC catalysts reach current densities between 69 and 124 mA/cm² for geometric Pt loadings of 0.8 - 1.6 $\mu\text{g}_{\text{Pt}}/\text{cm}^2$. The commercial Pt/Vulcan/Nafion reference catalysts reach 8 and 47 mA/cm² for geometric Pt loadings of 0.5 - 1.0 $\mu\text{g}_{\text{Pt}}/\text{cm}^2$. In the margin of error the current densities of both catalyst systems correlate linearly with the geometric loading (see trend lines). The catalytic behavior of the catalysts in the used state (50th cycle) is plotted in Figure 20d. All catalysts show a decreased activity by 40 - 50% of the initial current density. Again, for both systems the current density correlates linearly with the loading. In the fresh and in the used state PtNP/OMC catalysts reach a two times higher HER activity than the Pt/Vulcan/Nafion reference catalyst at -75 mV vs. RHE.

Transport phenomena might be one reason for the advanced catalytic performance. As shown in the Tafel plot (Figure 20b) PtNP/OMC obeys the Tafel equation is much broader current density regime than Pt/Vulcan/Nafion. The deviation from the linear relationship gives a strong indication that the Nafion-based catalyst is influenced by transport limitations at current densities higher than -10 mA/cm². Due to the synthesis procedure the morphology of the PtNP/OMC catalyst is more homogeneous than the Pt/Vulcan/Nafion catalyst films. The constant film thickness and pore morphology might be advantageous for an efficient transport. Furthermore, the binding species (Nafion) can block active sites and pores.

The HER performance of the PtNP/OMC is considerably high at very low geometric Pt loadings in comparison to Pt/C catalyst reported in literature. PtNP/OMC ($1.6 \mu\text{g}_{\text{Pt}}/\text{cm}^2$) catalyst reaches -100 mA/cm² at -80 mV vs. RHE (50th cycle). A commercial Pt/C reference catalysts (40 wt% Pt on carbon black from Johnson Matthey) deposited with Nafion with a 200 times higher Pt loading of 320 $\mu\text{g}_{\text{Pt}}/\text{cm}^2$ reached current density of -100 mA/cm² at -40 mV vs. RHE in 0.5 M H_2SO_4 published by Wu et al.¹²⁹ Other commercial Pt/C catalysts reached -100 mA/cm² in 0.5 M H_2SO_4 at following loadings: 2240 $\mu\text{g}_{\text{Pt}}/\text{cm}^2$ (20 wt% Pt/C) at -80 mV¹⁶⁹; 400 $\mu\text{g}_{\text{Pt}}/\text{cm}^2$ at -60 mV vs. RHE.¹⁷⁰

In summary, the PtNP/OMC film catalyst is highly active in the acidic HER. It shows a comparably stable performance as a Pt/Vulcan/Nafion reference catalyst. In the fresh as well as in the used state the PtNP/OMC catalyst reaches two times higher current densities than the commercial Pt/C catalysts in respect to geometric Pt content.

6.4 Conclusion

For the first time colloidal Pt nanoparticles are introduced into the synthesis procedure of ordered mesoporous carbon coatings. After carbonization the PtNP/OMC films are homogeneous, conductive and show a high surface area. The particle size of the colloidal particles can be retained despite the high temperatures during carbonization due to confinement effects inside the well-ordered mesopores. The synthesis approach ensures that no Pt is trapped in pore walls or micropores. The coating attaches without any binding species which would block active sites or pores. The electrocatalytic performance in the acidic hydrogen evolution reaction is high and proves that the Pt component is very efficiently employed. PtNP/OMC clearly outperforms Nafion-based Pt/C catalysts in HER especially at high current densities. The synthesis concept can be extended to all kinds of metal species including bimetallic nanoparticles.

6.5 Acknowledgement

The authors thank ZELMI (TU-Berlin) for providing infrastructure for electron microscopy. SAXS measurements were conducted at the BESSY mySpot beamline under assistance of Katrin Schulz. Arno Bergmann is acknowledged for Rietveld refinement. We thank Kornelia Weh and Astrid Müller-Klauke for support with ICP-OES analytics. DB, MB and RK acknowledge generous funding from BMBF under contract FKZ 03EK3009. RK particularly appreciates support from the Einstein Stiftung Berlin (EJF-2011-95).

7 General discussion

This chapter will discuss the results of chapters 3, 4, 5 and 6. Chapter 7.1 will study the influence of the employed metal precursor species, i.e. an ionic precursors (route 1) or a colloidal precursor (route 2) on film morphology, particle size distribution, particle crystallinity and electrocatalytic activity in the HER. Chapter 7.2 will compare the impact of the composition (Pd/OMC, Pt/OMC, Ru/OMC and RuPt/OMC, synthesized via route 1) on film morphology, particle size and particle composition as well as on the performance in the HER. The catalytic performance in respect to the metal content will be discussed. Furthermore, reasons for the high activity of RuPt/OMC will be addressed. Chapter 7.3 will present the Tafel evaluation (see chapter 1.3) of a Pt/OMC, a PtNP/OMC and a Pt/Vulcan/Nafion reference catalyst and will try to correlate their behavior in the Tafel regime with their structure. The final chapter 7.4 will compare the developed OMC catalysts with state-of-the-art catalysts in literature.

7.1 Influence of the metal precursor on structure and activity

In chapter 2, two synthesis routes towards metal containing OMC films were introduced. As explained in chapter 2.2, route 1 relies on the co-deposition of a polymeric carbon precursor and a structure-directing agent together with dissolved metal ions. Films synthesized via route 1 are denoted as Me/OMC. Route 2 employs preformed colloidal metallic nanoparticles which are deposited together with a polymeric carbon precursor and a structure-directing agent (see chapter 2.3). Films synthesized via route 2 are abbreviated by MeNP/OMC.

The current chapter will compare characteristics of Pt containing OMC films prepared by both routes. The films possess comparably high weight loadings in order to study the influence of the metal precursor species on film and pore morphology as well as the influence on nanoparticle size and crystallinity. Moreover, the performance in the electrocatalytic HER is compared.

Pore morphology

The pore morphologies of a metal-free OMC, a Pt/OMC and a PtNP/OMC film are studied in Figure 21 by cross-section SEM analyzes (Figure 21a) and SAXS (Figure 21b). All films were synthesized with F127 as structure directing agent. The OMC film was carbonized at 800 °C in N₂, Pt/OMC at 700 °C in N₂ and PtNP/OMC at 700 °C in H₂/Ar. (see chapter 2 for experimental details). Pt/OMC has a weight loading of 2.9 wt%_{Pt} and PtNP/OMC of 2.3 wt%_{Pt}, as determined by WDX/StrataGem evaluation at 10 keV.

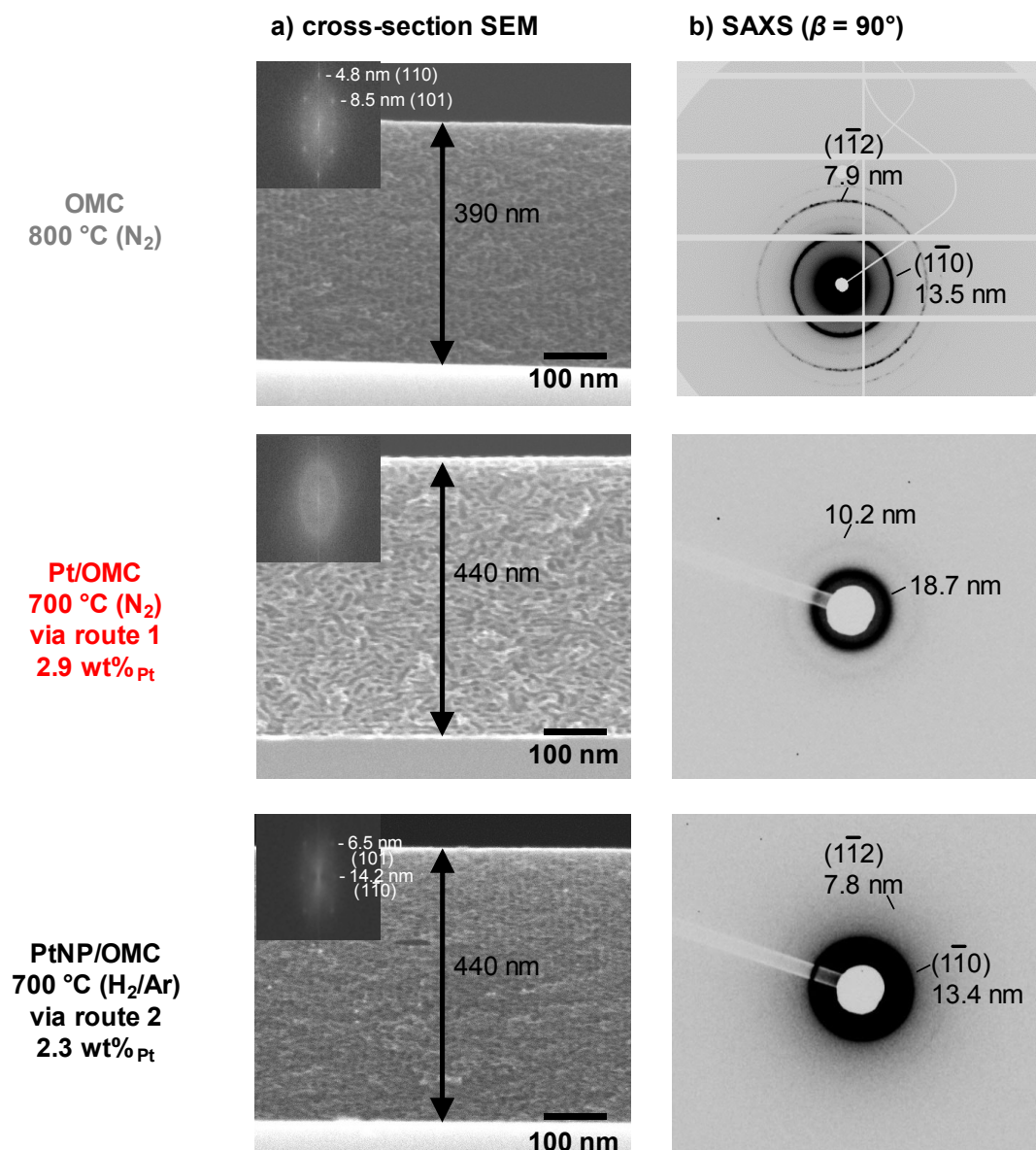


Figure 21. SEM and SAXS analyses of an OMC, a Pt/OMC (route 1) and a PtNP/OMC (route 2) film. F127 was used as templating agent and the films were carbonized for 3 h under the given conditions. a) Cross-section SEM images with FFT insets, b) SAXS patterns with incident angles of $\beta = 90^\circ$. The isotropic rings in (b) can be attributed to regular pore lattice distances.

Cross-section SEM (Figure 21a) confirms that all films are homogeneous and completely penetrated by ordered mesopores. The pores of Pt/OMC via route 1 appear less ordered and less densely packed than the pores of OMC and PtNP/OMC via route 2. The FFTs of the cross-section SEM images (insets in Figure 21a) of OMC and PtNP/OMC show spots which can be attributed to distinct pore lattice planes indicating ordered pore systems. The FFT of the SEM image of Pt/OMC shows an anisotropic ring confirming a locally ordered pore structure without a higher degree of pore ordering.

SAXS studied the pore structure of all films. Each pattern recorded in transmission with 90° (Figure 21b) features at least two circular diffraction rings. The periodic distances of

these most dominant reflections amount to 7.9 nm and 13.5 nm for OMC and 7.8 nm and 13.4 nm for PtNP/OMC, respectively. The distances attributed to these two reflections are circa 25% smaller than the distances observed for Pt/OMC (10.2 nm and 18.7 nm). The smaller periodic distances prove that OMC and PtNP/OMC possess a more densely packed pore system. In case of OMC and PtNP/OMC the ratios of the periodic distances of (1 $\bar{1}$ 2) to (1 $\bar{1}$ 0) equal $3^{1/2} \approx 1.7$. Accordingly, the diffraction rings can be assigned to the (1 $\bar{1}$ 0) and the (1 $\bar{1}$ 2) planes of a cubic pore lattice.⁸⁰ The diffraction pattern of Pt/OMC cannot be assigned to a cubic pore system which confirms the observation of SEM analyses that the pore system of Pt/OMC is less densely packed. Yet, the appearances of two distinct rings indicate a higher degree of ordering.

Since the OMC film as well as the PtNP/OMC in Figure 21 show a high degree of pore ordering, neither the atmosphere nor the temperature during carbonization have a significant influence on the mesostructure. However, the development of a densely packed pore system of Pt/OMC films via route 1 is disturbed. In chapter 4, Pt/OMC with lower loadings (1.5 wt%_{Pt}) showed a higher pore ordering than the film studied in this chapter (2.9 wt%_{Pt}). Apparently, metal ions in a high concentration hinder the formation of an ordered mesophase. A closer look at the formation of a micelle-structured mesophase helps to explain this observation. As discussed in chapter 1.5 a successful synthesis of OMC needs to fulfill three basic conditions⁴⁵:

The first condition says that the polymer needs to get an impetus to form micelles and has to show a strong affinity to the precursor species. The high concentration of metal ions has most likely no strong influence on micelle formation since mesopores are abundantly present in the Pt/OMC films with higher Pt loading. However, the mesopores which are visible in cross-section SEM appear wormhole-like and not ellipsoidal. The chemical affinity of the micelles towards the carbon precursor is probably not influenced as the functional groups of both species are not structurally changed. Yet, the metal ions interact with the PEO chains of the copolymer micelles.¹⁷¹ Maybe these interactions induce lamellar or other representations of the block copolymers leading to wormhole-like mesopores.

The second condition states that the carbon precursor has to be able to cross-link. In this case the metal ions may hinder the cross-linking because the metal ions also interact with hydroxyl or other functional groups of the carbon precursor (in this case a resorcinol-formaldehyde resin). It is possible that functional groups of the carbon precursor coordinate to the metal ion and thus are not available for building cross-links. A variation of the metal ion concentrations during the synthesis route 1 could examine this effect. The disruption of the mesostructure of OMC will be more intense the higher the metal

concentration is. In case of Pt/OMC films this effect begins to be severe at loading higher than 2.5 wt%_{Pt}.

The third requirement is that the cross-linked precursor species has to show a higher stability than the template species during thermal removal of the template. This condition is most likely not influenced by the presence of metal ions.

PtNP/OMC films with comparably high metal loadings show a well-ordered structure and a mesopore packing as dense as metal-free OMC films. According to this, neither the comparatively large nanoparticles nor the ammonium-based stabilizing agent disturb the mesophase formation. However, it is probable that higher nanoparticle concentrations will also disturb the pore ordering since they are sterically demanding.

Particle size, particle crystallinity and degree of graphitization

Particle size and crystallinity of nanoparticles in Pt/OMC (2.9 wt%_{Pt}, via route 1) and PtNP/OMC (2.3 wt%_{Pt}, via route 2) films are studied in Figure 22 with TEM (Figure 22a), HR-TEM (Figure 22c) and XRD (Figure 22d).

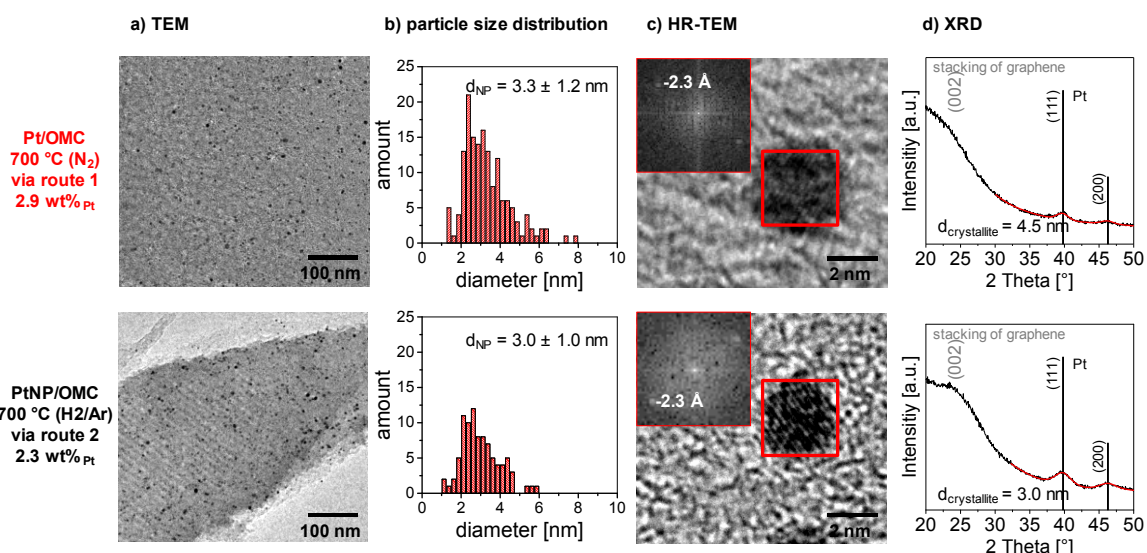


Figure 22. TEM, HR-TEM and XRD analyzes of a Pt/OMC (route 1) and a PtNP/OMC (route 2) film. F127 was used as templating agent and the films were carbonized at 700 °C in the given atmosphere. a) TEM micrograph of a scraped off film segment, b) particle size distribution of Pt nanoparticles determined by TEM, c) HR-TEM of a Pt particle with corresponding FFT inset and d) XRD pattern, indicated reflections of cubic Pt (04-0802) and Rietveld refinement (red).

TEM micrographs of Pt/OMC and PtNP/OMC films confirm an abundant presence of templated mesopores (Figure 22a). The pores of PtNP/OMC appear more ordered than the pores of Pt/OMC (compare to Figure 21). Dark spots evidence well-distributed Pt nanoparticles. The average diameters of Pt nanoparticles in Pt/OMC amount to 3.3 ± 1.2 nm. The average diameter is slightly larger than the particles in PtNP/OMC with 3.0 ± 1.0 nm in diameter (Figure 22b). The particle size distribution of Pt/OMC is broader

than of PtNP/OMC. Large particles with a diameter higher than 5 nm are more numerous in the Pt/OMC sample.

Lattice fringes in HR-TEM (Figure 22c) indicate a high crystallinity of the observed Pt nanoparticles. The spacing of the lattice planes amount to 2.3 Å for both systems. This distance fits with the (111) lattice plane of cubic Pt (04-0802, $Fm\bar{3}m$). The crystallinity and crystallite size was additionally evaluated with XRD (Figure 22d). Both films show reflections at 40° and 46° which can be attributed to cubic Pt. Rietveld refinements give crystallite diameters of 4.5 nm for Pt/OMC and 3.0 nm for PtNP/OMC. The crystallite size of PtNP/OMC corresponds well to the particle size from TEM measurements (Figure 22b). The crystallite diameter of Pt/OMC is larger than the average nanoparticle diameter determined by TEM which is indicative for larger Pt particles which were also observed by TEM.

The reason that larger particles (> 5 nm in diameter) are more numerous in highly-loaded Pt/OMC than PtNP/OMC films can be attributed to the formation mechanism of the nanoparticles. As explained in chapter 4.3, Pt nanoparticles in Pt/OMC films via route 1 are detectable by TEM at carbonization temperatures higher than 600 °C. At elevated temperatures Pt atoms and small Pt clusters are moving inside the mesoporous carbon network to form nanoparticles. (A detailed discussion about the mobility of metals during carbonization will be given in chapter 7.2.) When the process of nanoparticle formation is finished at temperatures around 700 °C, the particles are confined inside the mesopores and do not grow larger. The average particle diameters of the confined Pt nanoparticles amount to ca. 3.5 nm for all studied Pt/OMC films which were carbonized at 700 °C independent of the loading (see chapter 4.3). As known from literature, thermal reduction of nanoparticles at high temperatures usually leads to a high polydispersity.¹⁷² In case of OMC films the mesoporous structure suppresses the formation of even larger nanoparticles.⁷⁰ It is possible that also smaller Pt clusters form during thermal reduction of Pt/OMC films. These smaller particles (< 1 nm in diameter) are not detectable by TEM analysis. A part of these small Pt clusters might be trapped inside micropores or pore walls and thus is not available for the HER.

Preformed nanoparticles which are introduced into the film synthesis via route 2 undergo a different process during carbonization. As shown in chapter 6.3 the particle diameter of the colloidal particles amounts to 2.1 nm. During carbonization some Pt species are moving inside the carbon network. Sinter processes at elevated temperatures lead to slightly larger particles (3.0 nm) and a higher polydispersity. Nevertheless, the final particle diameter of Pt in PtNP/OMC is lower than in Pt/OMC since the mobility is lower and the degree of pore confinement effect most likely more pronounced for large preformed nanoparticles.

The degree of graphitization of the carbon film can be described by the XRD reflection at $2\theta = 24^\circ$ which can be assigned to stacking of graphene. Figure 22d shows that the reflection at 24° is more pronounced for PtNP/OMC than for Pt/OMC. The electrical conductivity also corresponds to the graphitization of the film. The conductivity of PtNP/OMC (30.4 S/cm) is four times higher than the conductivity of Pt/OMC (8.3 S/cm). Both observations indicate that PtNP/OMC has a higher degree of graphitization.

Most of the carbon in OMC films is graphitic as shown in chapters 3.3 and 4.3. The majority of the carbon precursor (resorcinol) is aromatic. During carbonization the aromatic mesoporous polymer is transformed into graphitic carbon.⁵⁴ As discussed before, Pt ions which are present during synthesis via route 1 may interact with functional groups of the carbon precursor compound and reduce their ability to cross-link. During this process the stacking of sp^2 -hybridized structures may be disturbed. This could explain the weak reflection at 24° in the X-ray pattern of Pt/OMC (see Figure 22d).

The lower conductivity could also be explained by another effect. As boron and nitrogen are present in the colloidal solution and the stabilizing agent these heteroatoms might enter the carbon network during film synthesis and carbonization. When boron substitutes carbon it alters its electronic structure¹⁷³ and can result in an increase in electrical conductivity of the carbon network.¹⁷⁴ Nitrogen doping also enhances electrical conductivity of OMC materials.¹⁷⁵ However, due to facts that the RF polymer has already formed when B and N species are added (see chapter 2.3) and the low content of B and N in the syntheses of PtNP/OMC the effect should be marginal. Conductivity studies with OMC films which were synthesized with additional stabilizing agent could verify this matter.

In conclusion, synthesis route 2 leads to a more defined film morphology for Pt-containing OMC films at higher Pt weight loadings than route 1. The templated mesopores of PtNP/OMC are densely packed and more ordered than the mesopores of Pt/OMC. Both synthesis routes lead to crystalline particles. However, the Pt nanoparticles in PtNP/OMC are smaller. Moreover, the degree of graphitization in the PtNP/OMC sample is higher, making the film more electrically conductive. The ionic precursor in route 1 disturbs interactions of carbon precursors and template micelles during film synthesis leading to a lower degree of graphitization. Whereas, preformed nanoparticles apparently have a less pronounced impact.

HER performance

The electrocatalytic performances of Pt/OMC catalyst films prepared via route 1 and a PtNP/OMC via route 2 were studied in a RDE setup with 0.5 M sulfuric acid using repeated potential cycles. Both catalysts exhibit similar weight loadings (Pt/OMC: 2.9 wt%_{Pt}, PtNP/OMC: 2.3 wt%_{Pt}). Figure 23a depicts the 2nd recorded cycle of a

Pt/OMC catalyst with a geometric loading of $1.2 \mu\text{g}_{\text{Pt}}/\text{cm}^2$ and a PtNP/OMC catalyst with $1.1 \mu\text{g}_{\text{Pt}}/\text{cm}^2$.

The film thickness and thus geometric Pt loading was adjusted by changing the withdrawal speed during the dip-coating procedure. Figure 23 plots the current density at -75 mV vs. RHE as a function of Pt loading during the 2nd cycle (b) and the 50th cycle (c), respectively. Each point in the diagram represents one measured catalyst film.

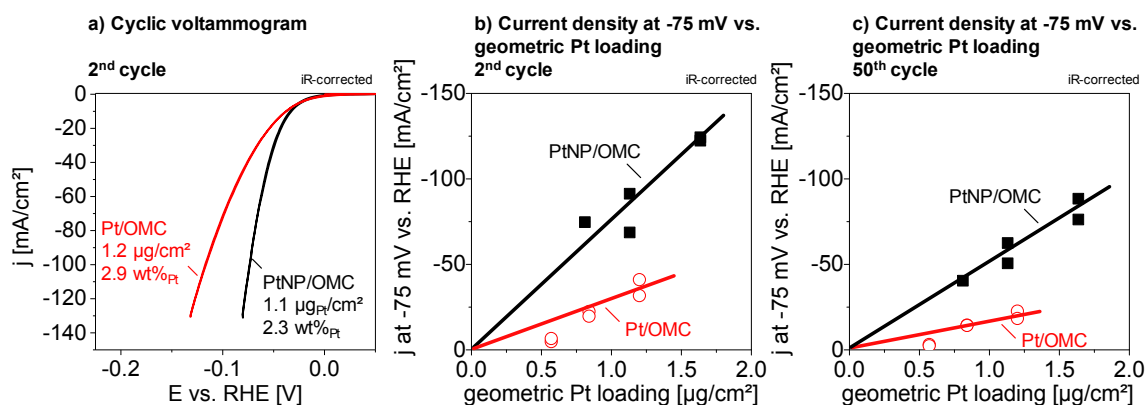


Figure 23. Electrochemical performance of F127-templated Pt-containing catalyst films in 0.5 M sulfuric acid. All films were carbonized at $700 \text{ }^\circ\text{C}$ for 3 h. Pt/OMC was carbonized in N_2 and PtNP/OMC in H_2/Ar . a) 2nd cycles of Pt/OMC (route 1) catalysts with Pt loading of $1.2 \mu\text{g}/\text{cm}^2$ compared to a PtNP/OMC catalysts (route 2) with $1.1 \mu\text{g}/\text{cm}^2$. b) and c) Current density at a potential of -75 mV vs. RHE at the 2nd (b) and 50th (c) cycle plotted against the geometric Pt loading of Pt/OMC and PtNP/OMC reference catalysts. Each point represents one measured catalyst. The mass loading of Pt/OMC was determined by WDX and StrataGem software.

Both types of catalysts are active in the HER, but the difference in structural properties like pore ordering, conductivity as well as nanoparticle size and accessibility influence the activity (compare Figure 23a). At current densities higher than $-10 \text{ mA}/\text{cm}^2$ PtNP/OMC clearly outperforms Pt/OMC. A Tafel evaluation of the second cycle in chapter 7.3 will discuss the electrocatalytic activity at low current densities in detail. Figure 23b and c show that the observed HER current scales (within the margin of error) linearly with the geometric loading for both types of catalyst. PtNP/OMC catalysts need 2-4 times less Pt to reach the same current density in the fresh (2nd cycle, Figure 23b) as well as in the used state (50th cycle, Figure 23c).

The enhanced activity of PtNP/OMC in the HER could be explained by improved transport properties and a better utilization of Pt inside the catalyst film. Pore morphology and particle size of PtNP/OMC help to explain this behavior. The pore morphology has an influence on transport properties. The mesopores in PtNP/OMC are ordered and more densely packed than in Pt/OMC which leads to a better interconnectivity of the pore system resulting in improved transport of electrolyte and H_2 molecules. PtNP/OMC films

show a higher degree of graphitization which results in lower ohmic resistance and thus reduced transport limitations of electrons. The average diameter of Pt nanoparticles in PtNP/OMC is smaller than in Pt/OMC. The particles in PtNP/OMC show fewer large Pt particles after carbonization. Moreover, the formation of small Pt particles is prevented, which could be trapped inside micropores or pore walls. These effects lead to more accessible active surface area in Pt/OMC films for the HER.

In summary, pore ordering, electrical conductivity as well as nanoparticle size and accessibility contribute to the HER activity of the discussed catalysts. It is not possible to distinguish which property contributes most to the enhanced performance of PtNP/OMC in comparison to Pt/OMC.

7.2 Influence of composition on structure and activity

The synthesis of OMC films with monometallic and bimetallic noble metal systems with the described synthesis approach (Scheme 3 on page 13) were demonstrated in chapters 3, 4 and 5. In order to avoid degradation effects or destruction of the carbon network during carbonization the conditions need to be chosen carefully. Table 3 summarizes the optimized carbonization conditions in terms of temperature and atmosphere.

Table 3. Synthesis conditions of F127-templated Me/OMC (route 1) films. Resorcinol and formaldehyde act as carbon precursor components in an acidic polycondensation reaction employing F127 as a structure-directing agent. The formed polymeric compound is re-dissolved in THF containing metal ions. The resulting solution is employed for dip-coating at 25 °C and 30% relative humidity. Films are thermo-polymerized at 100 °C for at least 12 hours and subsequently carbonized at the given temperature in the given atmosphere for 3 hours.

Synthesis conditions			
Me/OMC	Precursor	T_{carb}	Atmosphere
[°C]			
OMC	-	800	N ₂
Pd/OMC	Pd(acac) ₂	600	N ₂
Pt/OMC	Pt(NO ₃) ₂	700	N ₂
Ru/OMC	Ru(acac) ₃	800	H ₂ / Ar
RuPt/OMC	Ru(acac) ₃ Pt(NO ₃) ₂	800	H ₂ / Ar

The choice of the right carbonization conditions is critical for a successful Me/OMC film synthesis. Pd/OMC films are carbonized in nitrogen atmosphere at a moderate temperature (600 °C) since particle sintering effects are observed at higher temperatures. As explained in detail in chapter 4, Pt/OMC catalysts show optimal morphological properties and the highest HER performance at a carbonization temperature of 700 °C in N₂.

Ru-containing OMC films carbonized in N₂ showed severe carbon degradation effects and thus need a reducing atmosphere (H₂/Ar) during carbonization. Small Ru particles form at temperatures higher than 700 °C. Ru/OMC films which were carbonized at 800 °C showed HER activity. On the other hand, Pt/OMC as well as Pd/OMC catalyst films showed a tendency to form enlarged particles in reducing gas atmospheres like H₂/Ar. This behavior can be explained by a higher mobility of Pd and Pt in reducing atmosphere. Pilger et al. observed that the mobility of Pt clusters in Pt/CeO₂ is increased during thermal treatment in reducing (H₂/Ar) atmosphere.¹⁷⁶

This chapter discusses differences of OMC films prepared via route 1. The first sub-chapter debates the film morphology, the particle size and the mobility of metals at high temperatures during carbonization. The second sub-chapter discusses the catalytic activity as a function of the composition.

Film morphology, particle size and particle crystallinity

Figure 24 compares the structures of OMC and Me/OMC films prepared via route 1 with Me = Cu, Pd, Pt, Ru, RuPt. The overview illustrates the film morphology, nanoparticle morphology and crystallinity studied via top-view SEM (Figure 24a), cross-section SEM (b), TEM (c), high-resolution TEM (d) and XRD (e).

Generally, the morphology of the carbon matrix of Pd, Pt, Ru and RuPt/OMC films is similar. SEM images in Figure 24a and b proof that mesopores are well-ordered at the external surface and throughout the film volume. The films are crack-free and homogeneous in thickness. The pore diameters in all films range from 7 nm to 9 nm parallel to the substrate. Pd/OMC shows dispersed Pd particles of ca. 15 nm in diameter and some larger particle of ca. 50 nm at the external surface in Figure 24a. SEM images of the other Me/OMC films display small nanoparticles. In contrast, Cu/OMC exhibits a disrupted film structure with large cavities of ca. 20 - 100 nm in the film volume and large particles of ca. 50 nm at the external surface.

TEM micrographs in Figure 24c confirm the presence of well-dispersed particles inside the porous system for Pd, Pt, Ru and RuPt/OMC. The particle diameters vary significantly with the employed metal species. Pd/OMC films show particles with a diameter of ca. 14 nm, Pt particles in Pt/OMC have a diameter of 3 - 4 nm, Ru particles possess a diameter of 2 nm and bimetallic RuPt/OMC show particles between 2 - 4 nm (details in chapter 5.3). No nanoparticles were identified in Cu/OMC.

The differences in particle dimensions might be connected to the mobility of the metal at the corresponding temperature. The melting temperature of the bulk metals gives a very rough indication of this mobility. It amounts to 1555 °C for Pd, 1773 °C for Pt and 2500 °C for Ru.¹⁷⁷ The higher the melting temperature the smaller the particle diameter of the monometallic nanoparticle for OMC catalysts prepared via thermal reduction.

The so-called Tammann temperature correlates mobility of solid material with its melting point. It describes the temperature at which the thermal generation of defects inside a solid material leads a drastic increase of its reactivity.^{178, 179} The increased reactivity is correlated to the mobility in a premelting zone.¹⁷⁸ As a consequence, at temperatures above the Tammann temperature ($T_{Tammann}$) sintering occurs.¹⁸⁰ $T_{Tammann}$ is derived by multiplying the melting temperature (in Kelvin) with a factor. Tammann himself found a factor of 0.5 for oxides. Table 4 summarizes the employed carbonization temperature (T_{carb}) of the presented Me/OMC films, $T_{Tammann}$ (with factor of 0.5) of the employed metal and the nanoparticle diameter from TEM analysis.

Table 4. Carbonization temperature of F127-templated Me/OMC films via route 1. Films were carbonized at the given temperature for 3 h. The Tammann temperature ($T_{Tammann}$) for the employed metal species as well as the average nanoparticle diameter from TEM analysis is given.

Me/OMC	T_{carb} [°C]	$T_{Tammann}$ [°C]	Particle size [nm]
			TEM
Pd/OMC	600	641 (Pd)	14.3
Pt/OMC	700	750 (Pt)	3.5
Ru/OMC	800	1113 (Ru)	1.8
RuPt/OMC	800	1113 (Ru) 750 (Pt)	2.0 (Ru) 3.6 (Ru+Pt)

The optimized carbonization temperatures T_{carb} for Me/OMC films are below $T_{Tammann}$ for Pd, Pt and Ru. For Pd/OMC the difference ΔT between T_{carb} and $T_{Tammann}$ amounts to 40 °C, for Pt/OMC ΔT is 50 °C and for Ru/OMC ΔT is higher than 300 °C. The data suggest the higher ΔT is, the smaller the nanoparticle diameter becomes in the carbonized Me/OMC film. Yet, this hypothesis is not completely sound. The strong deviation in nanoparticle size of Pd in respect to Pt and Ru is not reflected in the differences of ΔT of the three metals.

Moreover, effects like melting point depression of nanoparticles most likely play a role. For example, the melting points of Pd and Pt nanoparticles are significantly lowered for particles with a diameter smaller than 20 nm.¹⁸¹ Also, the particle shape has an influence on the melting point.¹⁸¹

However, metals with $T_{Tammann}$ lower than 600 °C like Cu ($T_{Tammann} = 405$ °C)¹⁸² cannot be used. SEM and TEM images in Figure 24 showed that Cu in Cu/OMC films forms large metal structures outside the mesoporous network after carbonization at 600 °C. Lower carbonization temperatures are not applicable for Me/OMC syntheses as the removal of the mesopore template is not completed and the film not electrically conductive (see chapter 4.3).

The crystallinity of the particles is studied via HR-TEM (Figure 24d) and XRD (Figure 24e). HR-TEM measurements of Pd nanoparticles showed no lattice fringes. Nevertheless, the crystallinity of the Pd nanoparticles was confirmed by XRD which detected Pd in its metallic state. Lattice fringes visible in HR-TEM images of Pt, Ru and RuPt indicate a high crystallinity of the particles. The spacing of the fringes of Pt and Ru amounts to 2.3 Å and 2.1 Å, respectively. These values agree well with the (111) lattice planes present in the cubic Pt structure (04-0802, $Fm\bar{3}m$) and the (101) lattice planes of

hexagonal Ru (06-0663, P63/mmc), respectively. The XRD of Pt/OMC shows weak reflections which can be attributed to metallic Pt. Ru/OMC shows no detectable XRD signal as the particles are too small and additionally the amount of Ru in the film too low. As already discussed in chapter 5 the determination of the crystal structure of the nanoparticles present in RuPt/OMC is difficult. From electron and X-ray diffraction it is not possible to clearly differentiate between Ru and Pt. However, STEM-EDX measurements clarified that small Ru nanoparticles of 2 - 3 nm and larger bimetallic RuPt nanoparticles of 3-5 nm are present. The results were described in detail in chapter 5.3.

The electrical conductivity of Pt/OMC films depends on the carbonization temperature as described in chapter 4.3. Pd/OMC films carbonized at 600 °C in N₂ show a conductivity of 0.02 S/cm. Pt/OMC (700 °C in N₂) films exhibit a conductivity of 200 S/cm, Ru/OMC films (800 °C in H₂/Ar) of 500 S/cm and RuPt/OMC films (800 °C in H₂/Ar) of 800 S/cm. Figure 25 summarizes these results and combines them with the T_{carb} -study of Pt/OMC presented in Figure 10. The electrical film conductivity (log scale) is plotted as a function of the carbonization temperature.

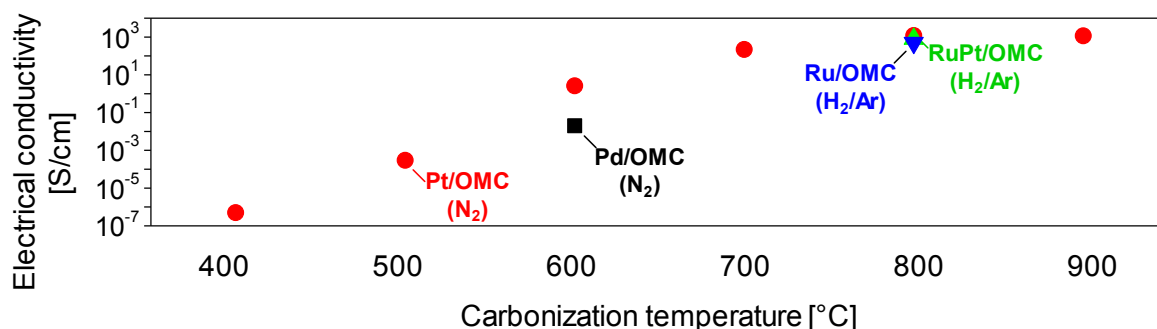


Figure 25. Influence of the carbonization temperature on F127-templated Me/OMC films on their electrical conductivity from sheet conductivity measurements. The films were carbonized for 3 h under the given conditions.

Graphitization at higher temperatures leads to an increase in conductivity as found for Pt/OMC in chapter 4.3. This trend seems to be valid for all Me/OMC films with small nanoparticles. Ru/OMC and RuPt/OMC have a similar conductivity as Pt/OMC at 800 °C. The choice of atmosphere has no considerable influence on the conductivity. Pd/OMC shows a significantly lower conductivity than Pt/OMC at 600 °C. This observation is contradictory since XRD characterization in Figure 6 proved that Pd/OMC has a comparable degree of graphitization as Pt/OMC (Supplement Figure S6). The large Pd nanoparticles in Pd/OMC may have a detrimental effect on the conductivity. In order to clarify this matter, the results need to be reproduced and the conductivity of Pd/OMC as a function of the carbonization temperature should be studied.

To conclude, monometallic Me/OMC films have been prepared with Me = Pd, Pt, Ru and bimetallic RuPt via route 1. The films are crack-free and show a templated mesoporosity. The films possess well-dispersed crystalline nanoparticles throughout the film volume. The size of nanoparticles depends on the melting temperature and thus $T_{Tammann}$ of the employed metal. The smaller the difference ΔT is between T_{carb} and $T_{Tammann}$ the larger the metal nanoparticles get. Me/OMC cannot be synthesized via route 1 with metals which have a $T_{Tammann}$ lower than 600 °C, e.g. Cu. The conductivity of Me/OMC films depends on T_{carb} and seems not to be influenced by the metal species or the atmosphere during carbonization.

HER performance

The electrochemical performance of Pd/OMC, Pt/OMC, Ru/OMC and RuPt/OMC prepared via route 1 was tested in the HER with a RDE setup in 0.5 M sulfuric acid. Figure 26 presents an evaluation of the electrochemical performance in the HER of Me/OMC films during the 2nd cycle of CV testing.

Each catalyst was exposed to a mild oxidative cleaning procedure prior to electrocatalytic testing. Since all Ru-containing catalysts showed a severe sensitivity towards thermal treatment in air slight variations were made to avoid combustion of film volume. All catalyst except the Pt/OMC were also re-reduced after air treatment for optimal catalytic activity. The catalysts were treated as follows:

- Pd/OMC: 400 °C for 20 min in air + 400 °C for 15 min in H₂/Ar
- Pt/OMC: 400 °C for 20 min in air
- Ru/OMC: 400 °C for 5 min in air + 400 °C for 15 min in H₂/Ar
- RuPt/OMC: 400 °C for 5 min in air + 400 °C for 15 min in H₂/Ar

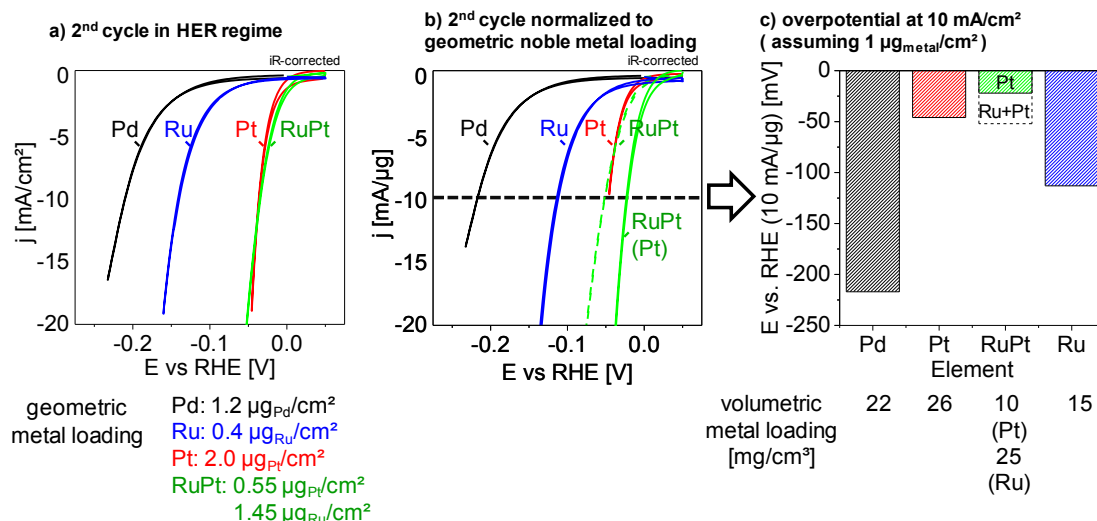


Figure 26. Electrochemical performance of F127-templated Me/OMC catalyst films. All films were carbonized and thermally treated differently for optimal performance. Cyclic voltammetric (CV) measurements were recorded in the HER regime with 20 mV/s in 0.5 M sulfuric acid. a) 2nd cycle of a CV measurement. In order to compare the specific activity of each catalyst the metal loading was determined by WDX/StrataGem. The noble metal loading is given below the plot. b) Current density of the 2nd cycle divided by the geometric loading against the potential. The curve of the RuPt/OMC catalyst is related to the total metal loading (Ru + Pt, dashed green line) as well as solely to the Pt loading (solid green line). c) Overpotential when the current of the 2nd cycle divided by the metal loading reaches 10 mA/μg. For the RuPt/OMC catalyst the overpotential is related to the Pt loading (green column) as well as related to the total metal loading of Ru and Pt (dashed column).

All catalysts showed HER activity, however, the potential needed to reach the same current response varies as expected from literature.¹⁸³ Figure 26a depicts the current response of the 2nd cycle of Pd/OMC, Ru/OMC, Pt/OMC as well as RuPt/OMC. Figure 26b plots the current density of the 2nd cycle normalized to the geometric loading against the potential. The curve of the RuPt/OMC catalyst is related to the total metal loading (Ru + Pt, dashed green line) as well as solely to the Pt loading (solid green line). Figure 26c compares the potentials at a current density of -10 mA/cm² normalized to geometric loading of 1 μg/cm². The overpotential of RuPt/OMC is normalized to the total metal loading (Ru+Pt, dotted column) as well as to the Pt loading (Pt, green column). The volumetric metal loading (in mg/cm³) which is derived from the film thickness and the geometric mass loading is given below the graphs. Although the films have different film thicknesses and geometric loadings, they exhibit comparable volumetric metal loadings between 15 mg/cm³ and 35 mg/cm³.

Pd/OMC with a film thickness of 440 nm has a Pd loading of 1.2 μg_{Pd}/cm². It shows the highest overpotential and reaches -10 mA/μg_{Pd} at about -218 mV. Ru/OMC with a film thickness of 250 nm has a geometric loading of 0.4 μg_{Ru}/cm². Ru/OMC is more active than Pd/OMC. The potential necessary to reach -10 mA/μg_{Ru} amounts to -113 mV. The Pt-containing catalysts need lower overpotentials. Pt/OMC has a film thickness of 780 nm and a loading of 2.0 μg_{Pt}/cm²: It reaches a current of -10 mA/μg_{Pt} at about -46 mV.

RuPt/OMC with a film thickness of 565 nm has a geometric loading of $0.55 \mu\text{g}_{\text{Pt}}/\text{cm}^2$ and $1.45 \mu\text{g}_{\text{Ru}}/\text{cm}^2$. It shows a similar activity as the Pt/OMC catalyst though it contains four times less Pt. At -52 mV RuPt/OMC reaches $-10 \text{ mA}/\mu\text{g}_{\text{Ru+Pt}}$. When the current per mass of Pt is considered, a potential of -22 mV is needed to reach $-10 \text{ mA}/\mu\text{g}_{\text{Pt}}$ which is explicitly smaller than for Pt/OMC.

Trasatti claimed that Ru has a higher overpotential in the HER than Pd.¹⁴⁸ The weaker activity of Pd/OMC than Ru/OMC might be influenced by the higher particle diameter of Pd and consequently a lower active surface area. Furthermore, the smaller electrical conductivity of Pd/OMC can weaken the catalyst performance.

Synthesis conditions, film morphology and information about the activity in the HER of Me/OMC films are summarized in Table 5.

Table 5. Synthesis conditions, film parameters and information about the initial activity in the HER of F127-templated Me/OMC films via route 1. Resorcinol and formaldehyde act as carbon precursors in an acidic polycondensation reaction employing F127 as a structure-directing agent. The formed polymeric compound is dispersed in THF which contains ionic metal precursors. The resulting solution is employed for dip-coating at $25 \text{ }^\circ\text{C}$ and 30% relative humidity. Films are thermo-polymerized at $100 \text{ }^\circ\text{C}$ for at least 12 h and subsequently carbonized at the given temperature and atmosphere for 3 h. For enhanced catalytic performance the films are additionally treated under the given conditions. The pore diameter parallel to the surface of the resulting film is listed. The pore diameter perpendicular to the substrate amounts to 2 nm. The average nanoparticle diameter is given. The potential to reach $10 \text{ mA}/\text{cm}^2$ as well as $10 \text{ mA}/\mu\text{g}_{\text{Me}}$ is summarized.

Me/OMC	Synthesis conditions						Film morphology		HER activity		
	Mass loading	Volumetric mass loading	Precursor	T_{carb}	Atmosphere	Activation procedure	Pore size	Particle size	Potential E at $-10 \text{ mA}/\text{cm}^2$	Potential E at $-10 \text{ mA}/\mu\text{g}$	
	$[\mu\text{g}/\text{cm}^2]$	$[\text{mg}/\text{cm}^3]$		$[^\circ\text{C}]$			$[\text{nm}]$	$[\text{nm}]$	$[\text{mV}]$	$[\text{mV}]$	
	WDX	WDX					SEM	TEM	2 nd cycle CV	2 nd cycle CV	
OMC	-	-	-	800	N_2	-	7	-	-	-	-
Pd/OMC	1.2	22	$\text{Pd}(\text{acac})_2$	600	N_2	20 min, $400 \text{ }^\circ\text{C}$, air + 15 min, $400 \text{ }^\circ\text{C}$, H_2/Ar	7	14.3	-212	-217	
Pt/OMC	2.0	26	$\text{Pt}(\text{NO}_3)_2$	700	N_2	20 min, $400 \text{ }^\circ\text{C}$, air	9	3.5	-36	-41	
Ru/OMC	0.4	15	$\text{Ru}(\text{acac})_3$	800	H_2 / Ar	5 min, $400 \text{ }^\circ\text{C}$, air + 15 min, $400 \text{ }^\circ\text{C}$, H_2/Ar	9	1.8	-142	-118	
RuPt/OMC	1.45 (Ru) 0.55 (Pt)	25 (Ru) 10 (Pt)	$\text{Ru}(\text{acac})_3$ $\text{Pt}(\text{NO}_3)_2$	800	H_2 / Ar	5 min, $400 \text{ }^\circ\text{C}$, air + 15 min, $400 \text{ }^\circ\text{C}$, H_2/Ar	8	2.0 (Ru) 3.6 (Ru+Pt)	-35	-52 ($10 \text{ mA}/\mu\text{g}_{\text{Ru+Pt}}$) -22 ($10 \text{ mA}/\mu\text{g}_{\text{Pt}}$)	

The observation that RuPt/OMC is as active as Pt/OMC is remarkable as the Pt content is much lower. The high activity can be explained by assuming that RuPt nanoparticles are at least as active as pure Pt nanoparticles. At low negative potentials only the larger bimetallic RuPt nanoparticles contribute to the HER activity since Ru has a higher overpotential. EDX-STEM analyses in Figure 14 and Supplement Figure S10 prove that Ru and Pt are equally distributed in the larger particles present in RuPt/OMC. When Ru atoms in an alloyed particle behave like Pt one can assume a doubled Pt loading of the RuPt/OMC film. For the RuPt/OMC catalyst listed in Table 5 that would result in a hypothetical Pt loading of $1.1 \mu\text{g}_{\text{Pt}}/\text{cm}^2$ instead of $0.55 \mu\text{g}_{\text{Pt}}/\text{cm}^2$. The resulting potential

needed to reach $-10 \text{ mA}/\mu\text{g}_{\text{Pt}}$ in this hypothetical case amounts to -36 mV which is similar to that of Pt/OMC (-41 mV). In addition, RuPt/OMC and Pt/OMC also show the same Tafel slope $b = 38 \text{ mV/dec}$ as shown in Figure 15.

Reasons for the high activity of RuPt/OMC were already addressed in chapter 5.3 and Figure 16. DFT calculations showed that RuPt alloys possess a slightly lower hydrogen binding energy than pure Pt.¹⁴⁹ It is possible that the slightly lower binding energy is advantageous for the HER. Yet, a validation of this assumption requires detailed DFT calculations in combination with in-depth analytics of the surface composition as well as the shape of the bimetallic particles for the RuPt/OMC system.

The particle size distribution in Figure 14 shows that ca. 85% of the particles in RuPt/OMC consist of monometallic Ru. It is possible that Ru nanoparticles contribute to the high HER activity. To study if the Ru particles have a positive effect on the catalyst performance it would be necessary to control the fraction of monometallic Ru particles in the catalyst film. However, the composition of the nanoparticles of RuPt/OMC films via route 1 with a varied Ru to Pt ratio was not studied. Therefore, it is not known if the fraction of monometallic Ru particles can be controlled via route 1. An approach via route 2 employing preformed monometallic Ru as well as preformed bimetallic RuPt nanoparticles seems more promising to achieve control over the film composition.

A reaction which is comparable to the HER is the hydrogen oxidation reaction (HOR). The HOR follows the same reaction mechanisms as the HER.¹⁸⁴ RuPt catalysts are studied in the HOR because they show high activity and a high CO tolerance.¹⁸⁵ Adžić and coworkers studied bimetallic RuPt catalysts with submonolayer amounts of Pt which showed high activities in the hydrogen oxidation reaction.^{186, 187} They explained that the high activity of Pt is retained even when only small islands or clusters are deposited on Ru.¹⁸⁸ In this context the high activity of the presented bimetallic RuPt catalysts can be explained as Pt clusters or facets may have formed on the particle surface. However, the formation of faceted Pt or core-shell structure in the case of RuPt/OMC contradicts Alayoglu et al..¹⁸⁹ They demonstrated that RuPt core-shell particles tend to form alloy structures upon annealing at temperatures above $500 \text{ }^\circ\text{C}$. The question why RuPt/OMC shows such a high activity is not trivial to answer. It is most likely that Ru and Pt form an alloy during synthesis of RuPt/OMC via route 1. The alloyed RuPt nanoparticles maintain the high HER activity of pure Pt or are even more active.

To conclude, synthesis route 1 towards Me/OMC films is successful for monometallic Pd, Ru, Pt as well as for bimetallic RuPt. The films exhibit an ordered mesoporous carbon matrix with incorporated and well dispersed nanoparticles. The order of electrocatalytic performance of Me/OMC films in the HER is as follows: $\text{Pd} < \text{Ru} < \text{Pt} = \text{RuPt}$. RuPt/OMC needs about two to four times less Pt than Pt/OMC to reach the same catalytic activity.

7.3 Tafel evaluation of Pt-containing carbon catalyst films

Mechanistic aspects of the HER can be studied by Tafel evaluation of current-voltage curves as explained in chapter 1.3. The potential E is plotted versus the logarithm of the current density j . The Tafel slope b indicates the rate-determining step of the HER. Values of 40 mV/dec refer to electrochemical formation of molecular H_2 (Heyrovsky reaction, $MeH_{ads} + H^+ + e^- \rightleftharpoons Me + H_2$), whereas values of 30 mV/dec are attributed to rate limitations by chemical H_2 desorption via recombination of adsorbed H atoms (Tafel reaction, $2 MeH_{ads} \rightleftharpoons 2 Me + H_2$).

Figure 27 compares the Tafel slopes of Pt/OMC via route 1, PtNP/OMC via route 2 and a commercial Pt/Vulcan catalyst prepared with Nafion via an ink-casting procedure. All films have a geometric Pt loading of ca. $1 \mu g_{Pt}/cm^2$. The Tafel plots of the 2nd cycle of cyclic voltammetric testing in the HER regime is shown in Figure 27a.

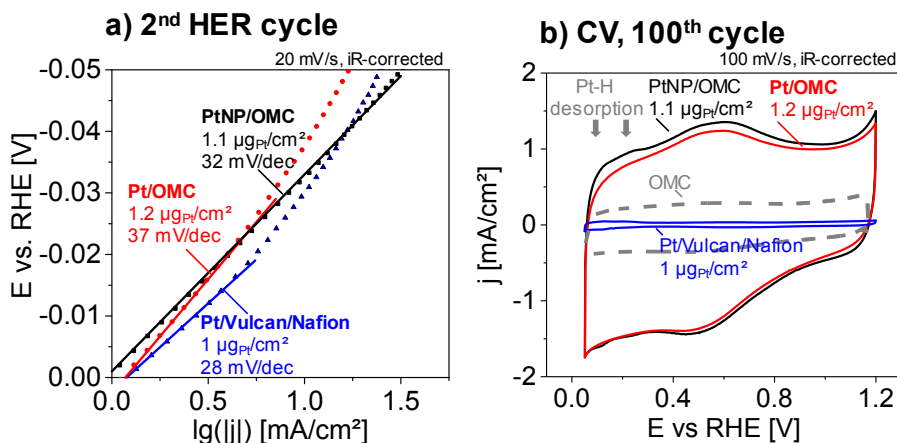


Figure 27. Electrocatalytic evaluation of Pt-containing catalyst films in 0.5 M sulfuric acid. A Pt/OMC (route 1) catalyst with a Pt loading of $1.2 \mu g/cm^2$, a PtNP/OMC (route 2) catalyst with $1.1 \mu g_{Pt}/cm^2$ OMC catalyst and a Pt/Vulcan/Nafion reference catalyst with $1.0 \mu g_{Pt}/cm^2$ are compared. Tafel evaluation (potential E vs. $\log(\text{current density})$) of the 2nd cycle (a) of a cyclic voltammetry measurement recorded in the HER regime with 20 mV/s. b) CV measurements recorded between 50 and 1200 mV: PtNP/OMC (700 °C, H_2/Ar), Pt/OMC (700 °C, N_2) and Pt/Vulcan/Nafion are compared to OMC film without Pt (800 °C, N_2) with a film thickness of 390 nm.

The Tafel slopes b during the cathodic sweep of the 2nd cycle (Figure 27a) amount to 37 mV/dec (Pt/OMC), 32 mV/dec (PtNP/OMC) and 28 mV/dec (Pt/Vulcan/Nafion). Accordingly, the rate-determining step of Pt/OMC can be attributed to the Heyrovsky reaction mechanism. PtNP/OMC and Pt/Vulcan/Nafion show a Tafel slope consistent with a Volmer-Tafel mechanism. PtNP/OMC shows a linear Tafel behaviour in a broader current density regime than Pt/OMC and Pt/Vulcan/Nafion.

The regimes in which Pt/OMC and Pt/Vulcan/Nafion follow the Tafel equation range up to current densities of 6 mA/cm² (10^{0.75} mA/cm²) and 4 mA/cm² (10^{0.6} mA/cm²), respectively. In contrast, PtNP/OMC shows a larger regime of linear correlation which ranges from 1 mA/cm² (10⁰ mA/cm²) to ca. 30 mA/cm² (10^{1.5} mA/cm²). Consequently, the HER activity of PtNP/OMC is not as restricted by transport limitations as Pt/OMC and Pt/Vulcan/Nafion in the regime of current densities up to 30 mA/cm².

Electrochemical analyses of the accessible Pt surface area would help to discuss the *b* values observed and to distinguish surface facets of the Pt nanoparticles for the different types of Pt catalysts. Usually, the electrochemical active surface area (ECSA) of Pt/C catalysts can be studied by evaluation of the underpotentially adsorbed hydrogen (H_{upd}) or CO-stripping experiments.^{190, 191} Now, these techniques are not applicable for the presented OMC-based catalysts as the carbon support shows a high extend of capacitive currents due to double layer charging.

Figure 27b compares the current responses during the 100th cycle of CV measurements between 50 and 1200 mV of a PtNP/OMC, a Pt/OMC, a Pt/Vulcan/Nafion and a Pt-free OMC film. The OMC based films exhibit a large hysteresis which indicates capacitive currents.¹⁹² The capacitive currents are so high that currents from underpotential adsorption or desorption of hydrogen cannot be detected. In comparison the H_{upd} peak of Pt/Vulcan/Nafion with 10wt%_{Pt} is clearly detectable. It is known that Vulcan shows a low capacitive current.¹⁹³ The Pt-free OMC film shows a hysteresis which is several times smaller. This is probably caused by the higher carbonization temperature which leads to fewer functional groups and a reduced microporosity.¹⁹⁴ The application of these OMC films as materials for supercapacitors is possible.¹⁷³

In conclusion, all Pt-based catalysts show a similar behaviour in the Tafel regime. During the 2nd HER cycle PtNP/OMC seems to be less restricted by transport limitations than Pt/OMC and Pt/Vulcan/Nafion at current densities between 10 mA/cm² and 30 mA/cm². Furthermore, Pt/Vulcan/Nafion deviates stronger from the linear behaviour at low current densities compared to the regime at higher currents densities than the OMC-based catalysts. As discussed in chapter 7.1, PtNP/OMC catalysts have a higher mesopore ordering, a more densely packed pore system, show a higher degree of graphitization and a higher electrical conductivity. Small nanoparticles are well-dispersed throughout the film volume. The particles are not trapped in micropores or pore walls. These properties most likely decrease transport limitations of electrolyte, H₂ or electrons.

7.4 Comparison to literature

The most prominent HER catalyst is platinum.⁶ Since Pt is expensive and scarce a lot of research is done to replace Pt by cheaper catalysts. A lot of candidates have been identified showing a high HER activity. Figure 28a summarizes the overpotential of different types of HER catalysts which were published in recent years.^{18, 106, 107, 128-131, 157, 169, 195-201} For sake of comparison the common benchmark of -10 mA/cm^2 was chosen, although this current density is rather low in respect to the necessary current densities in commercial electrolyzers. Pt/C catalysts clearly show the lowest overpotential (-15 to -50 mV) of all catalysts. For comparison, Pd/C catalysts reach the same current density at -40 mV and higher. NiMo, NiW, WO_x , MoS_2 and MoSe_2 are among the most active non-noble metal catalysts published so far. They reach -10 mA/cm^2 at overpotentials between -45 mV and -65 mV . These overpotentials are still regarded as too high for application.²⁰²

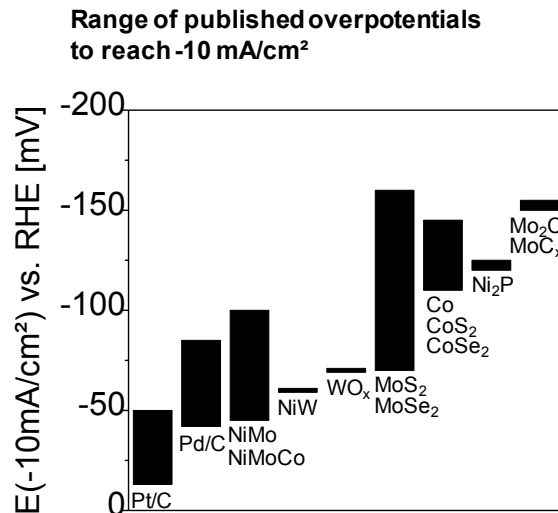


Figure 28. Necessary potential of HER catalysts to reach at 10 mA/cm^2 . a) Range of recently published overpotentials for different types of HER catalysts. Values were taken from following publications: Pt/C^{18, 107, 128-131, 169, 195, 196}, PdC^{106, 107}, NiMo¹⁹⁷, NiW¹⁹⁷, WO_x ¹³⁰, MoX_2 ^{18, 131}, CoX ^{131, 157, 169, 198}, Ni_2P ¹⁹⁹ and MoC_x ^{129, 200, 201}.

Figure 29 compares the performance of the developed OMC-based catalysts to Pt/C catalysts reported in literature.^{106, 107, 128-131, 157, 195, 196} Most of the Pt/C catalysts in literature were deposited with Nafion. The figure plots the overpotential required to reach -10 mA/cm^2 vs. the geometric Pt loading (in logarithmic scale). A catalyst which is located left in the diagram requires a low Pt loading to achieve a certain HER performance. All of the developed OMC catalysts possess a low Pt loading. In contrast, catalysts reported in literature have significantly higher Pt loadings.

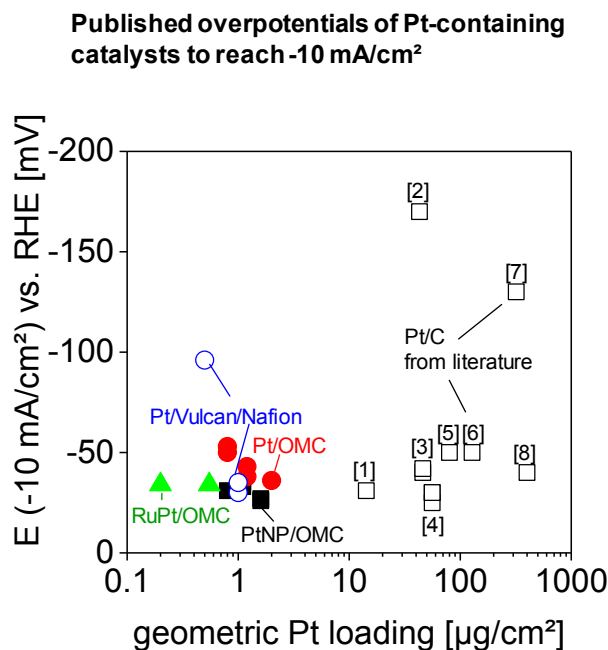


Figure 29. Overpotential at 10 mA/cm² of Pt-containing catalysts against the geometric Pt loading. The herein presented catalysts are compared to published overpotentials of Pt/C catalysts from literature. They exhibit a much smaller geometric Pt loading than Pt/C catalysts from literature at comparably low overpotentials. The values are taken from following publications: [1]¹³⁰, [2]¹⁰⁶, [3]¹⁰⁷, [4]^{131, 195}, [5]¹⁹⁶, [6]¹⁵⁷, [7]¹²⁹ and [8]¹²⁸

The Pt/C catalysts reported in literature are usually prepared by an ink-casting procedure which employs an ionomer binder (e.g. Nafion) to adhere the catalyst to the substrate. The Pt loadings range between 15 $\mu\text{g}_{\text{Pt}}/\text{cm}^2$ and 400 $\mu\text{g}_{\text{Pt}}/\text{cm}^2$. Most of the Pt/C catalysts reported in literature need about -25 mV to -50 mV to reach -10 mA/cm².

The catalysts studied in this thesis have significantly lower Pt loadings. Pt/OMC catalysts via route 1 (see chapter 4) achieve -10 mA/cm² at potentials between -38 mV and -53 mV at a geometric loading of 0.8 $\mu\text{g}_{\text{Pt}}/\text{cm}^2$ to 2.0 $\mu\text{g}_{\text{Pt}}/\text{cm}^2$. PtNP/OMC catalysts via route 2 (see chapter 6) need lower overpotentials of -26 mV to -35 mV at geometric loadings of 0.8 $\mu\text{g}_{\text{Pt}}/\text{cm}^2$ to 1.6 $\mu\text{g}_{\text{Pt}}/\text{cm}^2$ for the same HER performance. Accordingly, the overpotential is about 35% lower than that of Pt/OMC catalysts. RuPt/OMC catalysts via route 1 (see chapter 5) require lower Pt loadings for a similar performance. The geometric loadings amount to 0.2 $\mu\text{g}_{\text{Pt}}/\text{cm}^2$ and 0.55 $\mu\text{g}_{\text{Pt}}/\text{cm}^2$ to reach -10 mA/cm² at an overpotential of -34 mV. RuPt/OMC needs about four times less Pt to achieve the same HER performance as Pt/OMC catalysts. Pt/Vulcan/Nafion reference catalysts prepared via an ink-casting procedure with Pt loadings of 0.5 $\mu\text{g}_{\text{Pt}}/\text{cm}^2$ and 1.0 $\mu\text{g}_{\text{Pt}}/\text{cm}^2$ reached -10 mA/cm² at overpotentials between -30 mV and -96 mV. The HER performance is comparable to that of Pt containing OMC catalysts. However, as shown in chapters 4 and 6, Pt/OMC and PtNP/OMC catalysts outperform Pt/Vulcan/Nafion catalysts with similar loadings at higher overpotentials.

General discussion

To summarize, Pt-containing Me/OMC and MeNP/OMC catalysts reach the same HER performance as Pt/C catalysts in literature at much lower Pt loading. The presented OMC-based catalysts show the highest HER performance in terms of Pt loading of all HER catalysts reported so far.

8 Conclusions and outlook

This thesis presented two new synthesis routes for binder-free metal-containing ordered mesoporous carbon (OMC) catalyst films with homogeneous morphology. The film syntheses used two different kinds of metal precursors which were deposited via dip-coating together with polymeric carbon precursors in the presence of structure-directing polymer micelles. One approach employed dissolved metal ions as metal precursor (Me/OMC) and the other preformed colloidal metal nanoparticles (MeNP/OMC).

The developed synthesis routes produce homogeneous coatings comprised of small nanoparticles located in size-controlled mesopores in a partially graphitized carbon structure. The confinement of nanoparticles inside the mesopores has a stabilizing effect and suppresses aggregation and sintering. The mesoporous coatings possess a high surface area, good pore connectivity as well as excellent electrical conductivity, i.e. all properties required for good electrocatalysts.

Pd/OMC films prove to be highly active in the gas-phase hydrogenation of butadiene as well as in the electrocatalytic HER. In butadiene hydrogenation the obtained Pd/OMC coatings provide significantly higher space-time-yields than all reported Pd/C catalysts. When tested in the HER, the catalysts outperform reported Pd/C catalysts by a factor of three.

Pt/OMC catalyst films are more active than conventional Nafion-based Pt/C catalysts in HER in particular at high current densities that approach practical operation conditions. The enhanced performance can be explained by the abundant presence of mesopores, the improved accessibility of active centers and the absence of detrimental Nafion influences.

PtNP/OMC achieved the same HER performance as Pt/OMC catalysts at about 35% lower overpotentials. The use of preformed Pt nanoparticles prevents the formation of large Pt structures or Pt clusters which are inaccessible in micropores or pore walls. As a consequence, the active surface area of Pt can be utilized very efficiently for the HER. Kinetic studies showed that PtNP/OMC catalysts are suffered by transport limitations at higher current densities than Pt/OMC or Nafion-based commercial Pt/C catalysts.

RuPt/OMC catalyst films show the highest Pt-mass based HER activity reported in literature so far. Alloyed RuPt particles retain the high catalytic activity of pure Pt. As a consequence, the films need four times less Pt than commercially available Pt/C/Nafion catalysts to achieve the same catalytic performance.

RuPtNP/OMC catalyst films are expected to combine the described advantages. Preformed RuPt nanoparticles would be accessible inside an OMC coating leading to the best utilization of Pt for the HER. Future works will validate this assumption.

Yet, the proposed concept has limitations. The synthesis of Me/OMC films was only successful employing metals with a Tammann temperature higher than the necessary carbonization temperature of 600 °C. Furthermore, the optimal conditions for the carbonization process have to be identified individually for each metal. For example, Ru-containing OMC are carbonized in slightly reducing atmosphere (H_2/Ar) whereas Pd/OMC and Pt/OMC need an inert atmosphere (N_2). The ideal carbonization temperatures for the studied systems range between 600 °C and 800 °C. The metal content has also limitations. Above certain weight loadings of the metal component the advanced structural properties get lost. Pt/OMC films, for example, lose their high degree of mesopore ordering at loading higher than ca. 2.5 wt%_{Pt}.

However, the presented concept paves the way to the controlled synthesis of a wide range of highly active catalytic coatings that employ carbon as a support. Other metals such as Rh and other bimetallic systems can be studied under defined reaction conditions. Moreover, the catalyst properties can be easily tuned and enable the investigation of parameters such as pore size, film thickness and conductivity, and in particular the role of Nafion in electrocatalysis.

Further improvements in the composition can lead to even higher HER performances and lower costs for noble metals. Metal combinations in alloy or core-shell structure with M-H binding energies similar to that of Pt need to be identified. These metal combinations should form or be stable during the high temperatures of film carbonization. Moreover, they need to show stability in acidic medium and during HER. Obviously, the employed metals should be cheaper than Pt. DFT screenings can help to identify metal combinations that fulfill these requirements. In consequence, highly active and cheap catalysts with advanced structural properties can be realized with the presented synthesis strategies.

Bibliography

- (1) Kibler, L. A., Hydrogen Electrocatalysis. *ChemPhysChem* **2006**, 5, 985-991.
- (2) Marković, N. M.; Ross Jr, P. N., Surface science studies of model fuel cell electrocatalysts. *Surface Science Reports* **2002**, 4–6, 117-229.
- (3) Bjorketun, M. E.; Bondarenko, A. S.; Abrams, B. L.; Chorkendorff, I.; Rossmeisl, J., Screening of electrocatalytic materials for hydrogen evolution. *Physical Chemistry Chemical Physics* **2010**, 35, 10536-10541.
- (4) Greeley, J.; Jaramillo, T. F.; Bonde, J.; Chorkendorff, I.; Norskov, J. K., Computational high-throughput screening of electrocatalytic materials for hydrogen evolution. *Nature Materials* **2006**, 11, 909-913.
- (5) Skulason, E.; Karlberg, G. S.; Rossmeisl, J.; Bligaard, T.; Greeley, J.; Jonsson, H.; Norskov, J. K., Density functional theory calculations for the hydrogen evolution reaction in an electrochemical double layer on the Pt(111) electrode. *Physical Chemistry Chemical Physics* **2007**, 25, 3241-3250.
- (6) Zheng, Y.; Jiao, Y.; Jaroniec, M.; Qiao, S. Z., Advancing the Electrochemistry of the Hydrogen-Evolution Reaction through Combining Experiment and Theory. *Angewandte Chemie International Edition* **2015**, 1, 52-65.
- (7) Moussallem, I.; Jörissen, J.; Kunz, U.; Pinnow, S.; Turek, T., Chlor-alkali electrolysis with oxygen depolarized cathodes: history, present status and future prospects. *Journal of Applied Electrochemistry* **2008**, 9, 1177-1194.
- (8) Institute, T. C. Chlorine Manufacture. <http://www.chlorineinstitute.org/stewardship/about-chlorine/chlorine-manufacture.cfm> (07.01.2016), .
- (9) Stephens, I. E. L.; Chorkendorff, I., Minimierung des Platinbedarfs bei wasserstoffentwickelnden Elektroden. *Angewandte Chemie* **2011**, 7, 1512-1513.
- (10) Hirscher, M., Hydrogen Storage by Cryoadsorption in Ultrahigh-Porosity Metal–Organic Frameworks. *Angewandte Chemie International Edition* **2011**, 3, 581-582.
- (11) Carmo, M.; Fritz, D. L.; Mergel, J.; Stolten, D., A comprehensive review on PEM water electrolysis. *International Journal of Hydrogen Energy* **2013**, 12, 4901-4934.
- (12) Conway, B. E.; Tilak, B. V., Interfacial processes involving electrocatalytic evolution and oxidation of H₂, and the role of chemisorbed H. *Electrochimica Acta* **2002**, 22–23, 3571-3594.
- (13) Lasia, A., Hydrogen evolution reaction. In *Handbook of Fuel Cells*, John Wiley & Sons, Ltd: 2010..
- (14) Sabatier, P., *La catalyse en chimie organique*. 2e édition ed.; Paris, 1920..
- (15) Nørskov, J. K.; Bligaard, T.; Logadottir, A.; Kitchin, J. R.; Chen, J. G.; Pandelov, S.; Stimming, U., Trends in the Exchange Current for Hydrogen Evolution. *Journal of The Electrochemical Society* **2005**, 3, J23-J26.

- (16) Burstein, G. T., A hundred years of Tafel's Equation: 1905–2005. *Corrosion Science* **2005**, 12, 2858-2870.
- (17) Tafel, J., Über die Polarisation bei kathodischer Wasserstoffentwicklung. *Zeitschrift für physikalische Chemie* **1902**, 641-712.
- (18) Li, Y.; Wang, H.; Xie, L.; Liang, Y.; Hong, G.; Dai, H., MoS₂ Nanoparticles Grown on Graphene: An Advanced Catalyst for the Hydrogen Evolution Reaction. *Journal of the American Chemical Society* **2011**, 19, 7296-7299.
- (19) Laursen, A. B.; Kegnaes, S.; Dahl, S.; Chorkendorff, I., Molybdenum sulfides-efficient and viable materials for electro - and photoelectrocatalytic hydrogen evolution. *Energy & Environmental Science* **2012**, 2, 5577-5591.
- (20) Conway, B. E.; Salomon, M., Studies on the Hydrogen Evolution Reaction Down to -150°C and the Role of Proton Tunneling. *The Journal of Chemical Physics* **1964**, 10, 3169-3177.
- (21) Tavares, M. C.; Machado, S. A. S.; Mazo, L. H., Study of hydrogen evolution reaction in acid medium on Pt microelectrodes. *Electrochimica Acta* **2001**, 28, 4359-4369.
- (22) Laursen, A. B.; Varela, A. S.; Dionigi, F.; Fanchiu, H.; Miller, C.; Trinhammer, O. L.; Rossmeisl, J.; Dahl, S., Electrochemical Hydrogen Evolution: Sabatier's Principle and the Volcano Plot. *Journal of Chemical Education* **2012**, 12, 1595-1599.
- (23) Trasatti, S., Work function, electronegativity, and electrochemical behaviour of metals. *Journal of Electroanalytical Chemistry and Interfacial Electrochemistry* **1972**, 1, 163-184.
- (24) Joo, S. H.; Choi, S. J.; Oh, I.; Kwak, J.; Liu, Z.; Terasaki, O.; Ryoo, R., Ordered nanoporous arrays of carbon supporting high dispersions of platinum nanoparticles. *Nature* **2001**, 6843, 169-172.
- (25) Hasche, F.; Oezaslan, M.; Strasser, P., Activity, stability and degradation of multi walled carbon nanotube (MWCNT) supported Pt fuel cell electrocatalysts. *Physical Chemistry Chemical Physics* **2010**, 46, 15251-15258.
- (26) Jining, X.; Shouyan, W.; Aryasomayajula, L.; Varadan, V. K., Platinum decorated carbon nanotubes for highly sensitive amperometric glucose sensing. *Nanotechnology* **2007**, 6, 065503.
- (27) Li, Y.; Yang, R. T., Hydrogen Storage on Platinum Nanoparticles Doped on Superactivated Carbon. *The Journal of Physical Chemistry C* **2007**, 29, 11086-11094.
- (28) Lordi, V.; Yao, N.; Wei, J., Method for Supporting Platinum on Single-Walled Carbon Nanotubes for a Selective Hydrogenation Catalyst. *Chemistry of Materials* **2001**, 3, 733-737.
- (29) Liu, Z.; Ling, X. Y.; Su, X.; Lee, J. Y., Carbon-Supported Pt and PtRu Nanoparticles as Catalysts for a Direct Methanol Fuel Cell. *The Journal of Physical Chemistry B* **2004**, 24, 8234-8240.

- (30) Zhang, H.; Cui, H., Synthesis and Characterization of Functionalized Ionic Liquid-Stabilized Metal (Gold and Platinum) Nanoparticles and Metal Nanoparticle/Carbon Nanotube Hybrids. *Langmuir* **2009**, *5*, 2604-2612.
- (31) Wilson, M. S.; Gottesfeld, S., Thin-film catalyst layers for polymer electrolyte fuel cell electrodes. *J Appl Electrochem* **1992**, *1*, 1-7.
- (32) Tu, H.-C.; Wang, W.-L.; Wan, C.-C.; Wang, Y.-Y., Novel Method for the Synthesis of Hydrophobic Pt-Ru Nanoparticles and Its Application to Preparing a Nafion-Free Anode for the Direct Methanol Fuel Cell. *The Journal of Physical Chemistry B* **2006**, *32*, 15988-15993.
- (33) Kocha, S. S.; Zack, J. W.; Alia, S. M.; Neyerlin, K. C.; Pivovar, B. S., Influence of Ink Composition on the Electrochemical Properties of Pt/C Electrocatalysts. *ECS Transactions* **2013**, *2*, 1475-1485.
- (34) Shinozaki, K.; Pivovar, B. S.; Kocha, S. S., Enhanced Oxygen Reduction Activity on Pt/C for Nafion-free, Thin, Uniform Films in Rotating Disk Electrode Studies. *ECS Transactions* **2013**, *1*, 15-26.
- (35) Garsany, Y.; Ge, J.; St-Pierre, J.; Rocheleau, R.; Swider-Lyons, K. E., Analytical Procedure for Accurate Comparison of Rotating Disk Electrode Results for the Oxygen Reduction Activity of Pt/C. *Journal of The Electrochemical Society* **2014**, *5*, F628-F640.
- (36) Ahn, C.-Y.; Cheon, J.-Y.; Joo, S.-H.; Kim, J., Effects of ionomer content on Pt catalyst/ordered mesoporous carbon support in polymer electrolyte membrane fuel cells. *Journal of Power Sources* **2013**, 477-482.
- (37) Zhang, C.; Geng, Z.; Ma, J., Self-assembly synthesis of ordered mesoporous carbon thin film by a dip-coating technique. *Microporous and Mesoporous Materials* **2013**, *0*, 287-292.
- (38) Kataoka, S.; Yamamoto, T.; Endo, A.; Nakaiwa, M.; Ohmori, T., Synthesis and characterization of mesoporous carbon thin films from phloroglucinol/surfactant self-assembly. *Colloids and Surfaces A: Physicochemical and Engineering Aspects* **2009**, 1-3, 142-145.
- (39) Simanjuntak, F. H.; Jin, J.; Nishiyama, N.; Egashira, Y.; Ueyama, K., Ordered mesoporous carbon films prepared from 1,5-dihydroxynaphthalene/triblock copolymer composites. *Carbon* **2009**, *10*, 2531-2533.
- (40) Feng, D.; Lv, Y.; Wu, Z.; Dou, Y.; Han, L.; Sun, Z.; Xia, Y.; Zheng, G.; Zhao, D., Free-Standing Mesoporous Carbon Thin Films with Highly Ordered Pore Architectures for Nanodevices. *Journal of the American Chemical Society* **2011**, *38*, 15148-15156.
- (41) Qiang, Z.; Xue, J.; Cavicchi, K. A.; Vogt, B. D., Morphology Control in Mesoporous Carbon Films Using Solvent Vapor Annealing. *Langmuir* **2013**, *10*, 3428-3438.
- (42) Jin, J.; Nishiyama, N.; Egashira, Y.; Ueyama, K., Pore structure and pore size controls of ordered mesoporous carbons prepared from resorcinol/formaldehyde/triblock polymers. *Microporous and Mesoporous Materials* **2009**, 1-3, 218-223.

- (43) Kimura, T.; Emre, A. M.; Kato, K.; Hayashi, Y., Phenol resin carbonized films with anisotropic shrinkage driven ordered mesoporous structures. *Journal of Materials Chemistry A* **2013**, 47, 15135-15141.
- (44) Tanaka, S.; Katayama, Y.; Tate, M. P.; Hillhouse, H. W.; Miyake, Y., Fabrication of continuous mesoporous carbon films with face-centered orthorhombic symmetry through a soft templating pathway. *Journal of Materials Chemistry* **2007**, 34, 3639-3645.
- (45) Chuenchom, L.; Kraehnert, R.; Smarsly, B. M., Recent progress in soft-templating of porous carbon materials. *Soft Matter* **2012**, 42, 10801-10812.
- (46) Liang, C.; Hong, K.; Guiochon, G. A.; Mays, J. W.; Dai, S., Synthesis of a Large-Scale Highly Ordered Porous Carbon Film by Self-Assembly of Block Copolymers. *Angewandte Chemie International Edition* **2004**, 43, 5785-5789.
- (47) Song, L.; Feng, D.; Fredin, N. J.; Yager, K. G.; Jones, R. L.; Wu, Q.; Zhao, D.; Vogt, B. D., Challenges in Fabrication of Mesoporous Carbon Films with Ordered Cylindrical Pores via Phenolic Oligomer Self-Assembly with Triblock Copolymers. *ACS Nano* **2010**, 1, 189-198.
- (48) Tanaka, S.; Doi, A.; Nakatani, N.; Katayama, Y.; Miyake, Y., Synthesis of ordered mesoporous carbon films, powders, and fibers by direct triblock-copolymer-templating method using an ethanol/water system. *Carbon* **2009**, 11, 2688-2698.
- (49) Tang, C.; Tracz, A.; Kruk, M.; Zhang, R.; Smilgies, D.-M.; Matyjaszewski, K.; Kowalewski, T., Long-Range Ordered Thin Films of Block Copolymers Prepared by Zone-Casting and Their Thermal Conversion into Ordered Nanostructured Carbon. *Journal of the American Chemical Society* **2005**, 19, 6918-6919.
- (50) Tanaka, S.; Nishiyama, N.; Egashira, Y.; Ueyama, K., Synthesis of ordered mesoporous carbons with channel structure from an organic-organic nanocomposite. *Chemical Communications* **2005**, 16, 2125-2127.
- (51) Mitome, T.; Uchida, Y.; Egashira, Y.; Nishiyama, N., Synthesis of ordered mesoporous carbon films with a 3D pore structure and the electrochemical performance of electrochemical double layer capacitors. *Colloids and Surfaces A: Physicochemical and Engineering Aspects* **2014**, 0, 51-56.
- (52) Liang, C.; Dai, S., Synthesis of Mesoporous Carbon Materials via Enhanced Hydrogen-Bonding Interaction. *Journal of the American Chemical Society* **2006**, 16, 5316-5317.
- (53) Kataoka, S.; Yamamoto, T.; Inagi, Y.; Endo, A.; Nakaiwa, M.; Ohmori, T., Synthesis of ordered mesoporous carbon thin films at various temperatures in vapor infiltration method. *Carbon* **2008**, 10, 1358-1360.
- (54) Wang, X.; Liang, C.; Dai, S., Facile Synthesis of Ordered Mesoporous Carbons with High Thermal Stability by Self-Assembly of Resorcinol-Formaldehyde and Block Copolymers under Highly Acidic Conditions. *Langmuir* **2008**, 14, 7500-7505.
- (55) Sun, Z.; Sun, B.; Qiao, M.; Wei, J.; Yue, Q.; Wang, C.; Deng, Y.; Kaliaguine, S.; Zhao, D., A General Chelate-Assisted Co-Assembly to Metallic Nanoparticles-Incorporated Ordered Mesoporous Carbon Catalysts for Fischer-Tropsch Synthesis. *Journal of the American Chemical Society* **2012**, 42, 17653-17660.

- (56) Górka, J.; Jaroniec, M., Incorporation of Inorganic Nanoparticles into Mesoporous Carbons Synthesized by Soft Templating. *The Journal of Physical Chemistry C* **2008**, 31, 11657-11660.
- (57) Choma, J.; Jedynak, K.; Marszewski, M.; Jaroniec, M., Polymer-templated mesoporous carbons synthesized in the presence of nickel nanoparticles, nickel oxide nanoparticles, and nickel nitrate. *Applied Surface Science* **2012**, 8, 3763-3770.
- (58) Li, J.; Gu, J.; Li, H.; Liang, Y.; Hao, Y.; Sun, X.; Wang, L., Synthesis of highly ordered Fe-containing mesoporous carbon materials using soft templating routes. *Microporous and Mesoporous Materials* **2010**, 1–3, 144-149.
- (59) Zhai, Y.; Dou, Y.; Liu, X.; Tu, B.; Zhao, D., One-pot synthesis of magnetically separable ordered mesoporous carbon. *Journal of Materials Chemistry* **2009**, 20, 3292-3300.
- (60) Liu, R.; Ren, Y.; Shi, Y.; Zhang, F.; Zhang, L.; Tu, B.; Zhao, D., Controlled Synthesis of Ordered Mesoporous C–TiO₂ Nanocomposites with Crystalline Titania Frameworks from Organic–Inorganic–Amphiphilic Coassembly†. *Chemistry of Materials* **2008**, 3, 1140-1146.
- (61) Yao, J.; Li, L.; Song, H.; Liu, C.; Chen, X., Synthesis of magnetically separable ordered mesoporous carbons from F127/[Ni(H₂O)₆](NO₃)₂/resorcinol-formaldehyde composites. *Carbon* **2009**, 2, 436-444.
- (62) Gao, P.; Wang, A.; Wang, X.; Zhang, T., Synthesis of Highly Ordered Ir-Containing Mesoporous Carbon Materials by Organic–Organic Self-Assembly. *Chemistry of Materials* **2008**, 5, 1881-1888.
- (63) Gao, P.; Wang, A.; Wang, X.; Zhang, T., Synthesis and Catalytic Performance of Highly Ordered Ru-Containing Mesoporous Carbons for Hydrogenation of Cinnamaldehyde. *Catal Lett* **2008**, 3-4, 289-295.
- (64) Saha, D.; Deng, S., Hydrogen Adsorption on Ordered Mesoporous Carbons Doped with Pd, Pt, Ni, and Ru. *Langmuir* **2009**, 21, 12550-12560.
- (65) Dai, M.; Song, L.; LaBelle, J. T.; Vogt, B. D., Ordered Mesoporous Carbon Composite Films Containing Cobalt Oxide and Vanadia for Electrochemical Applications. *Chemistry of Materials* **2011**, 11, 2869-2878.
- (66) Bhaway, S. M.; Kisslinger, K.; Zhang, L.; Yager, K. G.; Schmitt, A. L.; Mahanthappa, M. K.; Karim, A.; Vogt, B. D., Mesoporous Carbon–Vanadium Oxide Films by Resol-Assisted, Triblock Copolymer-Templated Cooperative Self-Assembly. *ACS Applied Materials & Interfaces* **2014**, 21, 19288-19298.
- (67) Yu, J.-S.; Kang, S.; Yoon, S. B.; Chai, G., Fabrication of Ordered Uniform Porous Carbon Networks and Their Application to a Catalyst Supporter. *Journal of the American Chemical Society* **2002**, 32, 9382-9383.
- (68) Bernicke, M.; Ortel, E.; Reier, T.; Bergmann, A.; Ferreira de Araujo, J.; Strasser, P.; Kraehnert, R., Iridium Oxide Coatings with Templated Porosity as Highly Active Oxygen Evolution Catalysts: Structure-Activity Relationships. *ChemSusChem* **2015**, 11, 1908-1915.

- (69) Comotti, M.; Li, W.-C.; Spliethoff, B.; Schüth, F., Support Effect in High Activity Gold Catalysts for CO Oxidation. *Journal of the American Chemical Society* **2006**, 3, 917-924.
- (70) Galeano, C.; Meier, J. C.; Peinecke, V.; Bongard, H.; Katsounaros, I.; Topalov, A. A.; Lu, A.; Mayrhofer, K. J. J.; Schüth, F., Toward Highly Stable Electrocatalysts via Nanoparticle Pore Confinement. *Journal of the American Chemical Society* **2012**, 50, 20457-20465.
- (71) Valkama, S.; Nykänen, A.; Kosonen, H.; Ramani, R.; Tuomisto, F.; Engelhardt, P.; ten Brinke, G.; Ikkala, O.; Ruokolainen, J., Hierarchical Porosity in Self-Assembled Polymers: Post-Modification of Block Copolymer–Phenolic Resin Complexes by Pyrolysis Allows the Control of Micro- and Mesoporosity. *Advanced Functional Materials* **2007**, 2, 183-190.
- (72) Bönnemann, H.; Brijoux, W.; Brinkmann, R.; Joußen, T.; Korall, B.; Dinjus, E., Formation of Colloidal Transition Metals in Organic Phases and Their Application in Catalysis. *Angewandte Chemie International Edition in English* **1991**, 10, 1312-1314.
- (73) Bönnemann, H.; Braun, G.; Brijoux, W.; Brinkmann, R.; Tilling, A. S.; Seevogel, K.; Siepen, K., Nanoscale colloidal metals and alloys stabilized by solvents and surfactants Preparation and use as catalyst precursors. *Journal of Organometallic Chemistry* **1996**, 1–2, 143-162.
- (74) Bönnemann, H.; Brijoux, W.; Brinkmann, R.; Fretzen, R.; Jousen, T.; Koppler, R.; Korall, B.; Neiteler, P.; Richter, J., Preparation, Characterization, and Application of Fine Metal Particles and Metal Colloids Using Hydrotriorganoborates. *J Mol Catal* **1994**, 1-3, 129-177.
- (75) Schmidt, T. J.; Noeske, M.; Gasteiger, H. A.; Behm, R. J.; Britz, P.; Bönnemann, H., PtRu Alloy Colloids as Precursors for Fuel Cell Catalysts: A Combined XPS, AFM, HRTEM, and RDE Study. *Journal of The Electrochemical Society* **1998**, 3, 925-931.
- (76) Ruland, W.; Smarsly, B., X-ray scattering of non-graphitic carbon: an improved method of evaluation. *Journal of Applied Crystallography* **2002**, 5, 624-633.
- (77) Chuenchom, L. *Micelle-Templated Carbon Coatings and Their Applications for Catalysis*. Justus-Liebig-Universität Gießen, Gießen, 2013..
- (78) Ortel, E.; Fischer, A.; Chuenchom, L.; Polte, J.; Emmerling, F.; Smarsly, B.; Kraehnert, R., New Triblock Copolymer Templates, PEO-PB-PEO, for the Synthesis of Titania Films with Controlled Mesopore Size, Wall Thickness, and Bimodal Porosity. *Small* **2012**, 2, 298-309.
- (79) Ortel, E.; Reier, T.; Strasser, P.; Kraehnert, R., Mesoporous IrO₂ Films Templated by PEO-PB-PEO Block-Copolymers: Self-Assembly, Crystallization Behavior, and Electrocatalytic Performance. *Chemistry of Materials* **2011**, 13, 3201-3209.
- (80) Grosso, D.; Soler-Illia, G. J. d. A. A.; Crepaldi, E. L.; Cagnol, F.; Sinturel, C.; Bourgeois, A.; Brunet-Bruneau, A.; Amenitsch, H.; Albouy, P. A.; Sanchez, C., Highly Porous TiO₂ Anatase Optical Thin Films with Cubic Mesostructure Stabilized at 700 °C. *Chemistry of Materials* **2003**, 24, 4562-4570.

- (81) Chavez, V. L.; Song, L.; Barua, S.; Li, X.; Wu, Q.; Zhao, D.; Rege, K.; Vogt, B. D., Impact of nanopore morphology on cell viability on mesoporous polymer and carbon surfaces. *Acta Biomaterialia* **2010**, 8, 3035-3043.
- (82) Costacurta, S.; Falcaro, P.; Malfatti, L.; Marongiu, D.; Marmiroli, B.; Cacho-Nerin, F.; Amenitsch, H.; Kirkby, N.; Innocenzi, P., Shaping Mesoporous Films Using Dewetting on X-ray Pre-patterned Hydrophilic/Hydrophobic Layers and Pinning Effects at the Pattern Edge. *Langmuir* **2011**, 7, 3898-3905.
- (83) Arfsten, N. J.; Eberle, A.; Otto, J.; Reich, A., Investigations on the angle-dependent dip coating technique (ADDC) for the production of optical filters. *Journal of Sol-Gel Science and Technology* **1997**, 1, 1099-1104.
- (84) Song, L.; Feng, D.; Campbell, C. G.; Gu, D.; Forster, A. M.; Yager, K. G.; Fredin, N.; Lee, H.-J.; Jones, R. L.; Zhao, D.; Vogt, B. D., Robust conductive mesoporous carbon-silica composite films with highly ordered and oriented orthorhombic structures from triblock-copolymer template co-assembly. *Journal of Materials Chemistry* **2010**, 9, 1691-1701.
- (85) Li, X.; Larson, A. B.; Jiang, L.; Song, L.; Prichard, T.; Chawla, N.; Vogt, B. D., Evolution of mechanical, optical and electrical properties of self-assembled mesostructured phenolic resins during carbonization. *Microporous and Mesoporous Materials* **2011**, 1-3, 86-93.
- (86) Vogt, B. D.; Chavez, V. L.; Dai, M.; Arreola, M. R. C.; Song, L.; Feng, D.; Zhao, D.; Perera, G. M.; Stein, G. E., Impact of Film Thickness on the Morphology of Mesoporous Carbon Films Using Organic-Organic Self-Assembly. *Langmuir* **2011**, 9, 5607-5615.
- (87) Conway, B. E.; Bai, L., Determination of adsorption of OPD H species in the cathodic hydrogen evolution reaction at Pt in relation to electrocatalysis. *Journal of Electroanalytical Chemistry and Interfacial Electrochemistry* **1986**, 1, 149-175.
- (88) Lee, D. C.; Kim, J. H.; Kim, W. J.; Kang, J. H.; Moon, S. H., Selective hydrogenation of 1,3-butadiene on TiO₂-modified Pd/SiO₂ catalysts. *Applied Catalysis A: General* **2003**, 1, 83-91.
- (89) Oosthuizen, R. S.; Nyamori, V. O., Carbon Nanotubes as Supports for Palladium and Bimetallic Catalysts for Use in Hydrogenation Reactions. *Platinum Metals Review* **2011**, 3, 154-169.
- (90) Ortel, E.; Polte, J.; Bernsmeier, D.; Eckhardt, B.; Paul, B.; Bergmann, A.; Strasser, P.; Emmerling, F.; Kraehnert, R., Pd/TiO₂ coatings with template-controlled mesopore structure as highly active hydrogenation catalyst. *Applied Catalysis A: General* **2015**, 0, 25-32.
- (91) Seth, D.; Sarkar, A.; Ng, F. T. T.; Rempel, G. L., Selective hydrogenation of 1,3-butadiene in mixture with isobutene on a Pd/alumina catalyst in a semi-batch reactor. *Chemical Engineering Science* **2007**, 17, 4544-4557.
- (92) Silvestre-Albero, J.; Rupprechter, G.; Freund, H.-J., From Pd nanoparticles to single crystals: 1,3-butadiene hydrogenation on well-defined model catalysts. *Chemical Communications* **2006**, 1, 80-82.
- (93) Ghasemi, S.; Hosseini, S. R.; Nabipour, S.; Asen, P., Palladium nanoparticles supported on graphene as an efficient electrocatalyst for hydrogen evolution reaction. *International Journal of Hydrogen Energy* **2015**, 46, 16184-16191.

- (94) Darabdhara, G.; Amin, M. A.; Mersal, G. A. M.; Ahmed, E. M.; Das, M. R.; Zakaria, M. B.; Malgras, V.; Alshehri, S. M.; Yamauchi, Y.; Szunerits, S.; Boukherroub, R., Reduced graphene oxide nanosheets decorated with Au, Pd and Au-Pd bimetallic nanoparticles as highly efficient catalysts for electrochemical hydrogen generation. *Journal of Materials Chemistry A* **2015**, .
- (95) Zheng, J.-S.; Zhang, X.-S.; Li, P.; Zhu, J.; Zhou, X.-G.; Yuan, W.-K., Effect of carbon nanofiber microstructure on oxygen reduction activity of supported palladium electrocatalyst. *Electrochemistry Communications* **2007**, 5, 895-900.
- (96) Yang, S.; Shen, C.; Lu, X.; Tong, H.; Zhu, J.; Zhang, X.; Gao, H.-j., Preparation and electrochemistry of graphene nanosheets–multiwalled carbon nanotubes hybrid nanomaterials as Pd electrocatalyst support for formic acid oxidation. *Electrochimica Acta* **2012**, 0, 242-249.
- (97) Ortel, E.; Sokolov, S.; Zielke, C.; Lauermann, I.; Selve, S.; Weh, K.; Paul, B.; Polte, J.; Kraehnert, R., Supported Mesoporous and Hierarchical Porous Pd/TiO₂ Catalytic Coatings with Controlled Particle Size and Pore Structure. *Chemistry of Materials* **2012**, 20, 3828-3838.
- (98) Brezesinski, T.; Fischer, A.; Imura, K. i.; Sanchez, C.; Grosso, D.; Antonietti, M.; Smarsly, B. M., Generation of Self-Assembled 3D Mesoporous SnO₂ Thin Films with Highly Crystalline Frameworks. *Advanced Functional Materials* **2006**, 11, 1433-1440.
- (99) Crepaldi, E. L.; Soler-Illia, G. J. d. A. A.; Grosso, D.; Cagnol, F.; Ribot, F.; Sanchez, C., Controlled Formation of Highly Organized Mesoporous Titania Thin Films: From Mesoporous Hybrids to Mesoporous Nanoanatase TiO₂. *Journal of the American Chemical Society* **2003**, 32, 9770-9786.
- (100) Bernsmeier, D.; Ortel, E.; Polte, J.; Eckhardt, B.; Nowag, S.; Haag, R.; Kraehnert, R., Versatile control over size and spacing of small mesopores in metal oxide films and catalytic coatings via templating with hyperbranched core-multishell polymers. *Journal of Materials Chemistry A* **2014**, 32, 13075-13082.
- (101) Bockris, J. O. M.; Conway, B. E., Studies in hydrogen overpotential. The effect of catalytic poisons at platinized platinum and nickel. *Transactions of the Faraday Society* **1949**, 0, 989-999.
- (102) Bernicke, M.; Eckhardt, B.; Lippitz, A.; Ortel, E.; Bernsmeier, D.; Schmack, R.; Kraehnert, R., Synthesis and OER activity of NiO coatings with micelle–templated mesopore structure. *ChemistrySelect* **2016**, 3, 482-489.
- (103) Cui, C.; Gan, L.; Heggen, M.; Rudi, S.; Strasser, P., Compositional segregation in shaped Pt alloy nanoparticles and their structural behaviour during electrocatalysis. *Nature Materials* **2013**, 8, 765-771.
- (104) Ortel, E.; Polte, J.; Bernsmeier, D.; Eckhardt, B.; Paul, B.; Bergmann, A.; Strasser, P.; Emmerling, F.; Kraehnert, R., Pd/TiO₂ coatings with template-controlled mesopore structure as highly active hydrogenation catalyst. *Applied Catalysis A: General* **2015**, 25-32.
- (105) Pentland, N.; Bockris, J. O. M.; Sheldon, E., Hydrogen Evolution Reaction on Copper, Gold, Molybdenum, Palladium, Rhodium, and Iron: Mechanism and Measurement Technique under High Purity Conditions. *Journal of The Electrochemical Society* **1957**, 3, 182-194.

- (106) Bhowmik, T.; Kundu, M. K.; Barman, S., Palladium Nanoparticle–Graphitic Carbon Nitride Porous Synergistic Catalyst for Hydrogen Evolution/Oxidation Reactions over a Broad Range of pH and Correlation of Its Catalytic Activity with Measured Hydrogen Binding Energy. *ACS Catalysis* **2016**, 3, 1929-1941.
- (107) Bai, S.; Wang, C.; Deng, M.; Gong, M.; Bai, Y.; Jiang, J.; Xiong, Y., Surface Polarization Matters: Enhancing the Hydrogen-Evolution Reaction by Shrinking Pt Shells in Pt–Pd–Graphene Stack Structures. *Angewandte Chemie International Edition* **2014**, 45, 12120-12124.
- (108) Tang, C.; Wang, D.; Wu, Z.; Duan, B., Tungsten carbide hollow microspheres as electrocatalyst and platinum support for hydrogen evolution reaction. *International Journal of Hydrogen Energy* **2015**, 8, 3229-3237.
- (109) Garcia, R.; Besson, M.; Gallezot, P., Chemoselective catalytic oxidation of glycerol with air on platinum metals. *Applied Catalysis A: General* **1995**, 1–2, 165-176.
- (110) Qiang, Z.; Zhang, Y.; Wang, Y.; Bhaway, S. M.; Cavicchi, K. A.; Vogt, B. D., Highly aligned, large pore ordered mesoporous carbon films by solvent vapor annealing with soft shear. *Carbon* **2015**, 51-59.
- (111) Qiang, Z.; Xue, J.; Stein, G. E.; Cavicchi, K. A.; Vogt, B. D., Control of Ordering and Structure in Soft Templated Mesoporous Carbon Films by Use of Selective Solvent Additives. *Langmuir* **2013**, 27, 8703-8712.
- (112) Liang, C.; Li, Z.; Dai, S., Mesoporous Carbon Materials: Synthesis and Modification. *Angewandte Chemie International Edition* **2008**, 20, 3696-3717.
- (113) Tüysüz, H.; Schüth, F., Chapter Two - Ordered Mesoporous Materials as Catalysts. In *Advances in Catalysis*, Bruce, C. G.; Friederike, C. J., Eds. Academic Press: 2012; Vol. Volume 55, pp 127-239..
- (114) Meng, Y.; Gu, D.; Zhang, F.; Shi, Y.; Yang, H.; Li, Z.; Yu, C.; Tu, B.; Zhao, D., Ordered Mesoporous Polymers and Homologous Carbon Frameworks: Amphiphilic Surfactant Templating and Direct Transformation. *Angewandte Chemie International Edition* **2005**, 43, 7053-7059.
- (115) Luo, W.; Li, Y.; Dong, J.; Wei, J.; Xu, J.; Deng, Y.; Zhao, D., A Resol-Assisted Co-Assembly Approach to Crystalline Mesoporous Niobia Spheres for Electrochemical Biosensing. *Angewandte Chemie International Edition* **2013**, 40, 10505-10510.
- (116) Reier, T.; Oezaslan, M.; Strasser, P., Electrocatalytic Oxygen Evolution Reaction (OER) on Ru, Ir, and Pt Catalysts: A Comparative Study of Nanoparticles and Bulk Materials. *ACS Catalysis* **2012**, 8, 1765-1772.
- (117) Cui, C.; Gan, L.; Heggen, M.; Rudi, S.; Strasser, P., Compositional segregation in shaped Pt alloy nanoparticles and their structural behaviour during electrocatalysis. *Nat Mater* **2013**, 8, 765-771.
- (118) Ortel, E.; Hertwig, A.; Berger, D.; Esposito, P.; Rossi, A. M.; Kraehnert, R.; Hodoroaba, V.-D., New Approach on Quantification of Porosity of Thin Films via Electron-Excited X-ray Spectra. *Analytical Chemistry* **2016**, .
- (119) Menzel, N.; Ortel, E.; Mette, K.; Kraehnert, R.; Strasser, P., Dimensionally Stable Ru/Ir/TiO₂-Anodes with Tailored Mesoporosity for Efficient Electrochemical Chlorine Evolution. *ACS Catalysis* **2013**, 6, 1324-1333.

- (120) Eckhardt, B.; Ortel, E.; Polte, J.; Bernsmeier, D.; Görke, O.; Strasser, P.; Kraehnert, R., Micelle-Templated Mesoporous Films of Magnesium Carbonate and Magnesium Oxide. *Advanced Materials* **2012**, 23, 3115-3119.
- (121) Eckhardt, B.; Ortel, E.; Bernsmeier, D.; Polte, J.; Strasser, P.; Vainio, U.; Emmerling, F.; Kraehnert, R., Micelle-Templated Oxides and Carbonates of Zinc, Cobalt, and Aluminum and a Generalized Strategy for Their Synthesis. *Chemistry of Materials* **2013**, 14, 2749-2758.
- (122) Sanchez, C.; Boissière, C.; Grosso, D.; Laberty, C.; Nicole, L., Design, Synthesis, and Properties of Inorganic and Hybrid Thin Films Having Periodically Organized Nanoporosity. *Chemistry of Materials* **2008**, 3, 682-737.
- (123) De Bruijn, F. A.; Marin, G. B.; Niemantsverdriet, J. W.; Visscher, W. H. M.; Van Veen, J. A. R., Characterization of graphite-supported platinum catalysts by electrochemical methods and XPS. *Surface and Interface Analysis* **1992**, 1-12, 537-542.
- (124) Lau, W. M.; Huang, L. J.; Bello, I.; Yiu, Y. M.; Lee, S. T., Modification of surface band bending of diamond by low energy argon and carbon ion bombardment. *Journal of Applied Physics* **1994**, 7, 3385-3391.
- (125) Galeano, C.; Baldizzone, C.; Bongard, H.; Spliethoff, B.; Weidenthaler, C.; Meier, J. C.; Mayrhofer, K. J. J.; Schüth, F., Carbon-Based Yolk-Shell Materials for Fuel Cell Applications. *Advanced Functional Materials* **2014**, 2, 220-232.
- (126) Reddy, S.; Du, R.; Kang, L.; Mao, N.; Zhang, J., Three dimensional CNTs aerogel/MoSx as an electrocatalyst for hydrogen evolution reaction. *Applied Catalysis B: Environmental* **2016**, 16-21.
- (127) Gao, M.-R.; Liang, J.-X.; Zheng, Y.-R.; Xu, Y.-F.; Jiang, J.; Gao, Q.; Li, J.; Yu, S.-H., An efficient molybdenum disulfide/cobalt diselenide hybrid catalyst for electrochemical hydrogen generation. *Nat Commun* **2015**, .
- (128) Ma, L.; Ting, L. R. L.; Molinari, V.; Giordano, C.; Yeo, B. S., Efficient hydrogen evolution reaction catalyzed by molybdenum carbide and molybdenum nitride nanocatalysts synthesized via the urea glass route. *Journal of Materials Chemistry A* **2015**, 16, 8361-8368.
- (129) Wu, H. B.; Xia, B. Y.; Yu, L.; Yu, X.-Y.; Lou, X. W., Porous molybdenum carbide nano-octahedrons synthesized via confined carburization in metal-organic frameworks for efficient hydrogen production. *Nature Communications* **2015**, 6512, .
- (130) Li, Y. H.; Liu, P. F.; Pan, L. F.; Wang, H. F.; Yang, Z. Z.; Zheng, L. R.; Hu, P.; Zhao, H. J.; Gu, L.; Yang, H. G., Local atomic structure modulations activate metal oxide as electrocatalyst for hydrogen evolution in acidic water. *Nature Communications* **2015**, 8064, .
- (131) Gao, M.-R.; Liang, J.-X.; Zheng, Y.-R.; Xu, Y.-F.; Jiang, J.; Gao, Q.; Li, J.; Yu, S.-H., An efficient molybdenum disulfide/cobalt diselenide hybrid catalyst for electrochemical hydrogen generation. *Nature Communications* **2015**, 5982, .
- (132) Merki, D.; Fierro, S.; Vrabel, H.; Hu, X., Amorphous molybdenum sulfide films as catalysts for electrochemical hydrogen production in water. *Chemical Science* **2011**, 7, 1262-1267.

- (133) Xu, C.; Shen, P. k.; Liu, Y., Ethanol electrooxidation on Pt/C and Pd/C catalysts promoted with oxide. *Journal of Power Sources* **2007**, 2, 527-531.
- (134) Liu, Z.; Ling, X. Y.; Su, X.; Lee, J. Y.; Gan, L. M., Preparation and characterization of Pt/C and PtRu/C electrocatalysts for direct ethanol fuel cells. *Journal of Power Sources* **2005**, 1-7.
- (135) Perez-Alonso, F. J.; Elkjær, C. F.; Shim, S. S.; Abrams, B. L.; Stephens, I. E. L.; Chorkendorff, I., Identical locations transmission electron microscopy study of Pt/C electrocatalyst degradation during oxygen reduction reaction. *Journal of Power Sources* **2011**, 15, 6085-6091.
- (136) Kim, M.; Park, J.-N.; Kim, H.; Song, S.; Lee, W.-H., The preparation of Pt/C catalysts using various carbon materials for the cathode of PEMFC. *Journal of Power Sources* **2006**, 1, 93-97.
- (137) Cheng, L.; Huang, W.; Gong, Q.; Liu, C.; Liu, Z.; Li, Y.; Dai, H., Ultrathin WS₂ Nanoflakes as a High-Performance Electrocatalyst for the Hydrogen Evolution Reaction. *Angewandte Chemie International Edition* **2014**, 30, 7860-7863.
- (138) Sheng, W.; Gasteiger, H. A.; Shao-Horn, Y., Hydrogen Oxidation and Evolution Reaction Kinetics on Platinum: Acid vs Alkaline Electrolytes. *Journal of The Electrochemical Society* **2010**, 11, B1529-B1536.
- (139) Tymoczko, J.; Calle-Vallejo, F.; Schuhmann, W.; Bandarenka, A. S., Making the hydrogen evolution reaction in polymer electrolyte membrane electrolyzers even faster. *Nature Communications* **2016**, 10990, .
- (140) Hunt, S. T.; Milina, M.; Alba-Rubio, A. C.; Hendon, C. H.; Dumesic, J. A.; Román-Leshkov, Y., Self-assembly of noble metal monolayers on transition metal carbide nanoparticle catalysts. *Science* **2016**, 6288, 974-978.
- (141) Elbert, K.; Hu, J.; Ma, Z.; Zhang, Y.; Chen, G.; An, W.; Liu, P.; Isaacs, H. S.; Adzic, R. R.; Wang, J. X., Elucidating Hydrogen Oxidation/Evolution Kinetics in Base and Acid by Enhanced Activities at the Optimized Pt Shell Thickness on the Ru Core. *ACS Catalysis* **2015**, 11, 6764-6772.
- (142) Meng, Y.; Gu, D.; Zhang, F.; Shi, Y.; Yang, H.; Li, Z.; Yu, C.; Tu, B.; Zhao, D., Ordered Mesoporous Polymers and Homologous Carbon Frameworks: Amphiphilic Surfactant Templating and Direct Transformation. *Angewandte Chemie* **2005**, 43, 7215-7221.
- (143) Soin, N.; Roy, S. S.; Mitra, S. K.; Thundat, T.; McLaughlin, J. A., Nanocrystalline ruthenium oxide dispersed Few Layered Graphene (FLG) nanoflakes as supercapacitor electrodes. *Journal of Materials Chemistry* **2012**, 30, 14944-14950.
- (144) Chen, J.-Y.; Wang, L.-Y.; Wu, P.-W., Preparation and characterization of ruthenium films via an electroless deposition route. *Thin Solid Films* **2010**, 24, 7245-7248.
- (145) Zhang, M.; Chen, W.; Ding, S. J.; Wang, X. P.; Zhang, D. W.; Wang, L. K., Investigation of atomic-layer-deposited ruthenium nanocrystal growth on SiO₂ and Al₂O₃ films. *J. Vac. Sci. Technol. A* **2007**, 4, 775-780.
- (146) Meng, Y.; Gu, D.; Zhang, F.; Shi, Y.; Cheng, L.; Feng, D.; Wu, Z.; Chen, Z.; Wan, Y.; Stein, A.; Zhao, D., A Family of Highly Ordered Mesoporous Polymer Resin

- and Carbon Structures from Organic–Organic Self-Assembly. *Chemistry of Materials* **2006**, 18, 4447-4464.
- (147) Croy, J. R.; Mostafa, S.; Hickman, L.; Heinrich, H.; Cuenya, B. R., Bimetallic Pt-Metal catalysts for the decomposition of methanol: Effect of secondary metal on the oxidation state, activity, and selectivity of Pt. *Applied Catalysis A: General* **2008**, 2, 207-216.
- (148) Trasatti, S., Work function, electronegativity, and electrochemical behaviour of metals: III. Electrolytic hydrogen evolution in acid solutions. *Journal of Electroanalytical Chemistry and Interfacial Electrochemistry* **1972**, 1, 163-184.
- (149) Greeley, J.; Mavrikakis, M., Surface and Subsurface Hydrogen: Adsorption Properties on Transition Metals and Near-Surface Alloys. *The Journal of Physical Chemistry B* **2005**, 8, 3460-3471.
- (150) Kraehnert, R. Ammonia Oxidation over Polycrystalline Platinum: Surface Morphology and Kinetics at Atmospheric Pressure. Doctoral Thesis, Technische Universität Berlin, 2005..
- (151) Carrettin, S.; McMorn, P.; Johnston, P.; Griffin, K.; Kiely, C. J.; Hutchings, G. J., Oxidation of glycerol using supported Pt, Pd and Au catalysts. *Physical Chemistry Chemical Physics* **2003**, 6, 1329-1336.
- (152) Shim, W. G.; Kim, S. C., Heterogeneous adsorption and catalytic oxidation of benzene, toluene and xylene over spent and chemically regenerated platinum catalyst supported on activated carbon. *Applied Surface Science* **2010**, 17, 5566-5571.
- (153) Xu, X.; Li, X.; Gu, H.; Huang, Z.; Yan, X., A highly active and chemoselective assembled Pt/C(Fe) catalyst for hydrogenation of o-chloronitrobenzene. *Applied Catalysis A: General* **2012**, 17-23.
- (154) Fu, J.; Lu, X.; Savage, P. E., Hydrothermal Decarboxylation and Hydrogenation of Fatty Acids over Pt/C. *ChemSusChem* **2011**, 4, 481-486.
- (155) Suttisawat, Y.; Horikoshi, S.; Sakai, H.; Abe, M., Hydrogen production from tetralin over microwave-accelerated Pt-supported activated carbon. *International Journal of Hydrogen Energy* **2010**, 12, 6179-6183.
- (156) Shinohara, C.; Kawakami, S.; Moriga, T.; Hayashi, H.; Hodoshima, S.; Saito, Y.; Sugiyama, S., Local structure around platinum in Pt/C catalysts employed for liquid-phase dehydrogenation of decalin in the liquid-film state under reactive distillation conditions. *Applied Catalysis A: General* **2004**, 2, 251-255.
- (157) Deng, J.; Ren, P.; Deng, D.; Bao, X., Enhanced Electron Penetration through an Ultrathin Graphene Layer for Highly Efficient Catalysis of the Hydrogen Evolution Reaction. *Angewandte Chemie International Edition* **2015**, 7, 2100-2104.
- (158) Grigoriev, S. A.; Millet, P.; Fateev, V. N., Evaluation of carbon-supported Pt and Pd nanoparticles for the hydrogen evolution reaction in PEM water electrolyzers. *Journal of Power Sources* **2008**, 2, 281-285.
- (159) Antolini, E., Formation, microstructural characteristics and stability of carbon supported platinum catalysts for low temperature fuel cells. *Journal of Materials Science* **2003**, 14, 2995-3005.

- (160) Liu, Z.; Hong, L.; Tham, M. P.; Lim, T. H.; Jiang, H., Nanostructured Pt/C and Pd/C catalysts for direct formic acid fuel cells. *Journal of Power Sources* **2006**, 2, 831-835.
- (161) Liu, Q.; Joshi, U. A.; Uber, K.; Regalbuto, J. R., The control of Pt and Ru nanoparticle size on high surface area supports. *Physical Chemistry Chemical Physics* **2014**, 48, 26431-26435.
- (162) Liu, Z.; Gan, L. M.; Hong, L.; Chen, W.; Lee, J. Y., Carbon-supported Pt nanoparticles as catalysts for proton exchange membrane fuel cells. *Journal of Power Sources* **2005**, 1-2, 73-78.
- (163) Gloaguen, F.; Léger, J.-M.; Lamy, C., Electrocatalytic oxidation of methanol on platinum nanoparticles electrodeposited onto porous carbon substrates. *Journal of Applied Electrochemistry* **9**, 1052-1060.
- (164) Liu, W.-J.; Wu, B.-L.; Cha, C.-S., Surface diffusion and the spillover of H-adatoms and oxygen-containing surface species on the surface of carbon black and Pt/C porous electrodes. *Journal of Electroanalytical Chemistry* **1999**, 2, 101-108.
- (165) Wilson, M. S.; Gottesfeld, S., Thin-film catalyst layers for polymer electrolyte fuel cell electrodes. *Journal of Applied Electrochemistry* **1**, 1-7.
- (166) Garsany, Y.; Ge, J.; St-Pierre, J.; Rocheleau, R.; Swider-Lyons, K., ORR Measurements Reproducibility Using a RRDE. *ECS Transactions* **2013**, 1, 1233-1241.
- (167) Zhang, C.; Geng, Z.; Ma, J., Self-assembly synthesis of ordered mesoporous carbon thin film by a dip-coating technique. *Microporous and Mesoporous Materials* **2013**, 287-292.
- (168) Bonnemann, H.; Brijoux, W.; Brinkmann, R.; Fretzen, R.; Jousen, T.; Koppler, R.; Korall, B.; Neiteler, P.; Richter, J., Preparation, Characterization, and Application of Fine Metal Particles and Metal Colloids Using Hydrotriorganoborates. *J Mol Catal* **1994**, 1-3, 129-177.
- (169) Zhou, W.; Zhou, Y.; Yang, L.; Huang, J.; Ke, Y.; Zhou, K.; Li, L.; Chen, S., N-doped carbon-coated cobalt nanorod arrays supported on a titanium mesh as highly active electrocatalysts for the hydrogen evolution reaction. *Journal of Materials Chemistry A* **2015**, 5, 1915-1919.
- (170) Liu, W.; Hu, E.; Jiang, H.; Xiang, Y.; Weng, Z.; Li, M.; Fan, Q.; Yu, X.; Altman, E. I.; Wang, H., A highly active and stable hydrogen evolution catalyst based on pyrite-structured cobalt phosphosulfide. *Nature Communications* **2016**, 10771, .
- (171) Sakai, T.; Alexandridis, P., Mechanism of Gold Metal Ion Reduction, Nanoparticle Growth and Size Control in Aqueous Amphiphilic Block Copolymer Solutions at Ambient Conditions. *The Journal of Physical Chemistry B* **2005**, 16, 7766-7777.
- (172) Ortega-Amaya, R.; Matsumoto, Y.; Pérez-Guzmán, M. A.; Ortega-López, M., In situ synthesis of Cu₂O and Cu nanoparticles during the thermal reduction of copper foil-supported graphene oxide. *Journal of Nanoparticle Research* **2015**, 10, 1-8.
- (173) Wang, D.-W.; Li, F.; Chen, Z.-G.; Lu, G. Q.; Cheng, H.-M., Synthesis and Electrochemical Property of Boron-Doped Mesoporous Carbon in Supercapacitor. *Chemistry of Materials* **2008**, 22, 7195-7200.

- (174) Chang, H.; Joo, S. H.; Pak, C., Synthesis and characterization of mesoporous carbon for fuel cell applications. *Journal of Materials Chemistry* **2007**, 30, 3078-3088.
- (175) Datta, K. K. R.; Balasubramanian, V. V.; Ariga, K.; Mori, T.; Vinu, A., Highly Crystalline and Conductive Nitrogen-Doped Mesoporous Carbon with Graphitic Walls and Its Electrochemical Performance. *Chemistry – A European Journal* **2011**, 12, 3390-3397.
- (176) Pilger, F.; Testino, A.; Carino, A.; Proff, C.; Kambolis, A.; Cervellino, A.; Ludwig, C., Size Control of Pt Clusters on CeO₂ Nanoparticles via an Incorporation–Segregation Mechanism and Study of Segregation Kinetics. *ACS Catalysis* **2016**, 6, 3688-3699.
- (177) Szabó, Z. G.; Lakatos, B., On the melting point of transition metals. *Die Naturwissenschaften* **1952**, 21, 486-487.
- (178) Merkle, R.; Maier, J., On the Tammann–Rule. *Zeitschrift für anorganische und allgemeine Chemie* **2005**, 6-7, 1163-1166.
- (179) Tammann, G.; Sworykin, A., Zur Bestimmung der Temperatur des Zusammenbackens. *Zeitschrift für anorganische und allgemeine Chemie* **1928**, 1, 46-48.
- (180) Lu, H.; Khan, A.; Pratsinis, S. E.; Smirniotis, P. G., Flame-Made Durable Doped-CaO Nanosorbents for CO₂ Capture. *Energy & Fuels* **2009**, 2, 1093-1100.
- (181) Guisbiers, G.; Abudukelimu, G.; Hourlier, D., Size-dependent catalytic and melting properties of platinum-palladium nanoparticles. *Nanoscale Research Letters* **2011**, 1, 396-396.
- (182) Dies, K., Reines Kupfer. In *Kupfer und Kupferlegierungen in der Technik*, Springer Berlin Heidelberg: Berlin, Heidelberg, 1967; pp 100-114..
- (183) Miles, M. H., Evaluation of electrocatalysts for water electrolysis in alkaline solutions. *Journal of Electroanalytical Chemistry and Interfacial Electrochemistry* **1975**, 1, 89-96.
- (184) Mann, R. F.; Thurgood, C. P., Evaluation of Tafel–Volmer kinetic parameters for the hydrogen oxidation reaction on Pt(1 1 0) electrodes. *Journal of Power Sources* **2011**, 10, 4705-4713.
- (185) Zhang, L.; Kim, J.; Chen, H. M.; Nan, F.; Dudeck, K.; Liu, R.-S.; Botton, G. A.; Zhang, J., A novel CO-tolerant PtRu core–shell structured electrocatalyst with Ru rich in core and Pt rich in shell for hydrogen oxidation reaction and its implication in proton exchange membrane fuel cell. *Journal of Power Sources* **2011**, 22, 9117-9123.
- (186) Sasaki, K.; Wang, J. X.; Balasubramanian, M.; McBreen, J.; Uribe, F.; Adzic, R. R., Ultra-low platinum content fuel cell anode electrocatalyst with a long-term performance stability. *Electrochimica Acta* **2004**, 22–23, 3873-3877.
- (187) Brankovic, S. R.; Wang, J. X.; Adžić, R. R., Pt Submonolayers on Ru Nanoparticles: A Novel Low Pt Loading, High CO Tolerance Fuel Cell Electrocatalyst. *Electrochemical and Solid-State Letters* **2001**, 12, A217-A220.

- (188) Wang, J. X.; Brankovic, S. R.; Zhu, Y.; Hanson, J. C.; Adžić, R. R., Kinetic Characterization of PtRu Fuel Cell Anode Catalysts Made by Spontaneous Pt Deposition on Ru Nanoparticles. *Journal of The Electrochemical Society* **2003**, *8*, A1108-A1117.
- (189) Alayoglu, S.; Nilekar, A. U.; Mavrikakis, M.; Eichhorn, B., Ru-Pt core-shell nanoparticles for preferential oxidation of carbon monoxide in hydrogen. *Nature Materials* **2008**, *4*, 333-338.
- (190) van der Vliet, D. F.; Wang, C.; Li, D.; Paulikas, A. P.; Greeley, J.; Rankin, R. B.; Strmcnik, D.; Tripkovic, D.; Markovic, N. M.; Stamenkovic, V. R., Unique Electrochemical Adsorption Properties of Pt-Skin Surfaces. *Angewandte Chemie* **2012**, *13*, 3193-3196.
- (191) Rudi, S.; Cui, C.; Gan, L.; Strasser, P., Comparative Study of the Electrocatalytically Active Surface Areas (ECSAs) of Pt Alloy Nanoparticles Evaluated by Hupd and CO-stripping voltammetry. *Electrocatalysis* **2014**, *4*, 408-418.
- (192) Chen, X.; He, D.; Wu, H.; Zhao, X.; Zhang, J.; Cheng, K.; Wu, P.; Mu, S., Platinized Graphene/ceramics Nano-sandwiched Architectures and Electrodes with Outstanding Performance for PEM Fuel Cells. *Scientific Reports* **2015**, 16246.
- (193) Guha, A.; Zawodzinski Jr, T. A.; Schiraldi, D. A., Evaluation of electrochemical performance for surface-modified carbons as catalyst support in polymer electrolyte membrane (PEM) fuel cells. *Journal of Power Sources* **2007**, *2*, 530-541.
- (194) Chmiola, J.; Yushin, G.; Gogotsi, Y.; Portet, C.; Simon, P.; Taberna, P. L., Anomalous Increase in Carbon Capacitance at Pore Sizes Less Than 1 Nanometer. *Science* **2006**, 5794, 1760-1763.
- (195) Hou, D.; Zhou, W.; Zhou, K.; Zhou, Y.; Zhong, J.; Yang, L.; Lu, J.; Li, G.; Chen, S., Flexible and porous catalyst electrodes constructed by Co nanoparticles@nitrogen-doped graphene films for highly efficient hydrogen evolution. *Journal of Materials Chemistry A* **2015**, *31*, 15962-15968.
- (196) Wang, D.-Y.; Gong, M.; Chou, H.-L.; Pan, C.-J.; Chen, H.-A.; Wu, Y.; Lin, M.-C.; Guan, M.; Yang, J.; Chen, C.-W.; Wang, Y.-L.; Hwang, B.-J.; Chen, C.-C.; Dai, H., Highly Active and Stable Hybrid Catalyst of Cobalt-Doped FeS₂ Nanosheets–Carbon Nanotubes for Hydrogen Evolution Reaction. *Journal of the American Chemical Society* **2015**, *4*, 1587-1592.
- (197) McCrory, C. C. L.; Jung, S.; Ferrer, I. M.; Chatman, S. M.; Peters, J. C.; Jaramillo, T. F., Benchmarking Hydrogen Evolving Reaction and Oxygen Evolving Reaction Electrocatalysts for Solar Water Splitting Devices. *Journal of the American Chemical Society* **2015**, *13*, 4347-4357.
- (198) Faber, M. S.; Dziejczak, R.; Lukowski, M. A.; Kaiser, N. S.; Ding, Q.; Jin, S., High-Performance Electrocatalysis Using Metallic Cobalt Pyrite (CoS₂) Micro- and Nanostructures. *Journal of the American Chemical Society* **2014**, *28*, 10053-10061.
- (199) Feng, L.; Vrabel, H.; Bensimon, M.; Hu, X., Easily-prepared dinickel phosphide (Ni₂P) nanoparticles as an efficient and robust electrocatalyst for hydrogen evolution. *Physical Chemistry Chemical Physics* **2014**, *13*, 5917-5921.

- (200) Chen, W. F.; Wang, C. H.; Sasaki, K.; Marinkovic, N.; Xu, W.; Muckerman, J. T.; Zhu, Y.; Adzic, R. R., Highly active and durable nanostructured molybdenum carbide electrocatalysts for hydrogen production. *Energy & Environmental Science* **2013**, 3, 943-951.
- (201) Zhang, J.; Meng, X.; Zhao, J.; Zhu, Z., Construction of a MoxC/Ni Network Electrode with Low Overpotential for Hydrogen Generation. *ChemCatChem* **2014**, 7, 2059-2064.
- (202) Vesborg, P. C. K.; Seger, B.; Chorkendorff, I., Recent Development in Hydrogen Evolution Reaction Catalysts and Their Practical Implementation. *The Journal of Physical Chemistry Letters* **2015**, 6, 951-957.

List of publications, patents and conference talks

Peer-reviewed publications

1. Eckhardt, B.; Ortel, E.; Polte, J.; Bernsmeier, D.; Görke, O.; Strasser, P.; Kraehnert, R., Micelle-Templated Mesoporous Films of Magnesium Carbonate and Magnesium Oxide. *Advanced Materials* **2012**, *24* (23), 3115-3119.
2. Eckhardt, B.; Ortel, E.; Bernsmeier, D.; Polte, J.; Strasser, P.; Vainio, U.; Emmerling, F.; Kraehnert, R., Micelle-Templated Oxides and Carbonates of Zinc, Cobalt, and Aluminum and a Generalized Strategy for Their Synthesis. *Chemistry of Materials* **2013**, *25* (14), 2749-2758.
3. Bernsmeier, D.; Ortel, E.; Polte, J.; Eckhardt, B.; Nowag, S.; Haag, R.; Kraehnert, R., Versatile control over size and spacing of small mesopores in metal oxide films and catalytic coatings via templating with hyperbranched core-multishell polymers. *Journal of Materials Chemistry A* **2014**, *2* (32), 13075-13082.
4. Bernsmeier, D.; Polte, J.; Ortel, E.; Krahl, T.; Kemnitz, E.; Kraehnert, R., Antireflective Coatings with Adjustable Refractive Index and Porosity Synthesized by Micelle-Templated Deposition of MgF₂ Sol Particles. *ACS Applied Materials & Interfaces* **2014**, *6* (22), 19559-19565.
5. Fetyan, A.; Derr, I.; Kayarkatte, M. K.; Langner, J.; Bernsmeier, D.; Kraehnert, R.; Roth, C., Electrospun Carbon Nanofibers as Alternative Electrode Materials for Vanadium Redox Flow Batteries. *ChemElectroChem* **2015**, *2* (12), 2055-2060.
6. Ortel, E.; Polte, J.; Bernsmeier, D.; Eckhardt, B.; Paul, B.; Bergmann, A.; Strasser, P.; Emmerling, F.; Kraehnert, R., Pd/TiO₂ coatings with template-controlled mesopore structure as highly active hydrogenation catalyst. *Applied Catalysis A: General* **2015**, *493*, 25-32.

Patents

Kraehnert, R.; Eckhardt, B.; Ortel, E.; Bernsmeier, D., Preparing mesoporous-metal carbonate or metal oxide films, fibers or powders, comprises preparing a solution comprising e.g. organic template, and dispersing the solution in a distribution device in droplets to form powder or fibers. **2013**.

Conference talks

1. Bernsmeier, D.; Bernicke, M.; Chuenchom, L.; Smarsly, B.; Kraehnert, R., Micelle-Templated Mesoporous Pt/C Catalysts for the Electrochemical Hydrogen Evolution Reaction. In *26. Deutsche Zeolith-Tagung*, Paderborn, Germany, **2014**.
2. Bernsmeier, D.; Bernicke, M.; Chuenchom, L.; Smarsly, B.; Kraehnert, R., Micelle-Templated Mesoporous Pt/C Catalysts for the Electrochemical Hydrogen Evolution Reaction. In *E-MRS 2014 Spring Meeting*, Lille, France, **2014**.
3. Bernsmeier, D.; Bernicke, M.; Eckhardt, B.; Chęcinski, M. P.; Kulesza, A.; Kraehnert, R., Mesoporous Bimetallic Carbon-supported Catalysts for the Efficient Electrocatalytic Hydrogen Evolution Reaction. In *E-MRS 2015 Fall Meeting*, Warsaw, Poland, **2015**.
4. Bernsmeier, D.; Bernicke, M.; Eckhardt, B.; Kraehnert, R., Mesoporous Bimetallic Carbon-supported Catalysts for the Efficient Electrocatalytic Hydrogen Evolution Reaction. In *1st Symposium on Electrocatalysis & Materials for Energy Conversion and Storage*, El Gouna, Egypt, **2015**.
5. Bernicke, M.; Eckhardt, B.; Ortel, E.; Bernsmeier, D.; Schmack, R.; Kraehnert, R., Synthesis of micelle-templated mesoporous NiO layer via Carbonate route/intermediate for Oxygen Evolution Reaction In *28. Deutsche Zeolith-Tagung* Gießen, Germany, **2016**.
6. Bernsmeier, D.; Bernicke, M.; Sachse, R.; Ortel, E.; Eckhardt, B.; Schmack, R.; Kraehnert, R., Synthesis Concepts for Noble Metal containing Ordered Mesoporous Carbon Coatings. In *2nd Symposium on Electrocatalysis & Materials for Energy Conversion and Storage*, El Gouna, Egypt, **2016**.
7. Bernsmeier, D.; Sachse, R.; Bernicke, M.; Kraehnert, R., Preformed Colloidal Pt Nanoparticles in Ordered Mesoporous Carbon Coatings as highly active Electrocatalysts for the Hydrogen Evolution Reaction. In *49. Jahrestreffen Deutscher Katalytiker*, Weimar, Germany, **2016**.

Since 2012: 18 Posters as first author at national and international conferences.

Danksagung

Bei meiner Doktorarbeit haben mich viele Menschen über die letzten Jahre fachlich und moralisch unterstützt. Für die Hilfe und den Rückhalt bin ich zutiefst dankbar.

Ganz herzlich möchte ich meinem Doktorvater, Dr.-Ing. Ralph Krähnert, für die Möglichkeit der Promotion danken. Sein Vertrauen, seine strukturierte Beratung und die fortwährende Bereitschaft mich zu unterstützen haben diese Arbeit ermöglicht. Darüber hinaus möchte ich ihm danken, dass ich stets meine Ergebnisse auf nationalen und internationalen Konferenzen vorstellen konnte, um mit inspirierenden Erkenntnissen heimzukehren.

Herrn Professor Arne Thomas danke ich für die bereitwillige Übernahme des Prüfungsvorsitzes. Bei Frau Professor Christina Roth und Herrn Professor Peter Strasser bedanke ich mich herzlich für die Begutachtung dieser Arbeit.

Mein besonderer Dank gilt der Arbeitsgruppe Krähnert. Für die gute Zusammenarbeit, für wissenschaftliche Diskussion, für bereitwillige Hilfestellungen, für viele nette Gespräche und lustige Abende danke ich meinen Kollegen Katrin Schulz, Kornelia Weh, Michael Bernicke, Laemthong Chuenchom, Björn Eckhardt, Erik Ortel, Benjamin Paul, René Sachse, Roman Schmack und Huan Wang.

Meinen Kollegen der Arbeitsgruppe Strasser danke ich sehr für die freundliche Arbeitsatmosphäre, die Unterstützung, den guten Umgang und die schöne Zeit:

Ich danke vielmals den weiteren Kooperationspartnern und Coautoren für die fruchtbare Zusammenarbeit: Arno Bergmann, Ines Häusler, Frieder Kettemann, Andreas Lippitz, Jörg Nissen, Jörg Polte, Stefan Rümmler, Sören Selve, Bernd Smarsly und Ulla Vainio.

Außerdem danke ich dem Team der feinmechanischen Werkstatt, Glasbläser Carsten und Astrid für ICP-OES sowie den Wissenschaftlern aus zahlreichen Kooperationen anderer Projekte.

Ana Sofia, Katrin, Romina, Frau Weh, Arno, Erik, Micha und René danke ich fürs sorgsame Korrekturlesen dieser Arbeit.

Zu guter Letzt danke ich meiner Familie und meinen Freunden!

